Hemodynamic alterations at the Blood-Brain Barrier and optimization of renal denervation treatment to prevent vascular impairment

Fernando García Polite

DOCTORAL THESIS

Title	Hemodynamic alterations at the Blood-Brain Barrier and optimization of renal denervation treatment to prevent vascular impairment.
Presented by	Fernando García Polite
Centre	IQS School of Engineering
Department	Chemical Engineering
Directed by	Dra. Mercedes Balcells Camps Dr. José Javier Molins Vara

C. Claravall, 1-3
08022 Barcelona
Tel. 93 602 22 00
Fax 93 602 22 49
a/e. info@url.edu
www.url.edu

Acknowledgements

A la Dra. Mercedes Balcells por confiar en mi desde el día que nos conocimos y por enseñarme a superar cualquier obstáculo. Gracias, Merche, por la paciencia, el apoyo y las oportunidades que me has dado durante todos estos años. Ha sido un placer realizar este proyecto contigo.

Al Dr. José Javier Molins, por ser un gran mentor y por introducirme en un campo de infinitas posibilidades y del que he podido obtener muchos frutos. Tu conocimiento y tus consejos han sido claves para llegar a este momento.

To Professor Elazer R. Edelman, for his invaluable support and guidance and for showing me that any puzzle can be solved if you look into the right perspective.

To Dr. Rami Tzafriri, for trusting me in all the challenging projects I've been involved and for the big opportunities that derived from them. I look forward to learn much more from you.

Al Dr. Jordi Martorell López, por saber guiarme profesionalmente y ser a la vez un buen amigo en todas las etapas que hemos pasado, desde años atrás como auxiliar hasta ahora como profesor.

Al Dr. Andrés A. García-Granada, al Dr. Guillermo Reyes, al Dr. Joaquin Menacho y a César Alquézar, por su colaboración en los aspectos más ingenieriles de este trabajo.

Al Dr. Pedro Melgar-Lesmes, gracias por la interminable ayuda a cualquier hora y especialmente por los ánimos en los buenos y malos momentos en el laboratorio.

To Dr. Caroline O'Brien, for your help during my first months in the lab and for your support no matter the distance and time.

Al Dr. Jaume Roquer, al Dr. Ángel Ois y al Dr. Alessandro Principe, por su ayuda y consejos durante la experimentación animal de este trabajo.

To the members of the Edelman Lab and the employees of CBSET, for being welcoming since the beginning and for their friendliness in such inspiring work environments.

A Paula, por compartir conmigo los momentos más divertidos y también los más duros de parte de este proyecto. Gracias por tu apoyo dentro y fuera del laboratorio. A Mario, por ser un pozo sin fondo de sabiduría del que siempre salieron grandes ideas. A l'Oriol, per l'ajuda durant els darrers mesos i la rapidesa en que vas aprendre.

A los amigos de siempre, en especial a Victor, Eric y Pol, por el apoyo continuo a pesar de estar constantemente repartidos por el mundo y por los buenos momentos habidos y por haber. A los compañeros de la universidad, por todo lo que hemos pasado juntos.

Als meus companys de pis, Majo, Helena, Alicia, Ferran i Pipo, a l'equip Somerville, Jose, Marcel i Andreu, al comando JP, Jaume i Biel, a la petita Gemma i als veterans Jordi i Elena, a tota la gran família Bostoniana, perquè arribar a una nova ciutat i tenir-vos al costat des del primer dia no té preu.

A la Cris, perquè trobar-te durant aquest procés ha sigut sens dubte el millor que podia haver passat. Gràcies per estar sempre disponible, per ajudar-me a resoldre qualsevol problema i per animar-me a aconseguir tot el que em proposi.

A mis sobrinos, Aitana, Daniela y Matías, por no perder nunca la sonrisa y saber alegrar cualquier situación.

A mis hermanos, Pablo y Nacho, por todo el esfuerzo dedicado a vuestro hermano pequeño y porque, a pesar de ser los tres distintos, sois el mejor espejo en el que mirarse.

A mis padres, por su cariño y su preocupación, por apoyarme en todas las decisiones de mi vida, por enseñarme que cualquier cosa se puede conseguir si uno lo intenta y por inspirarme cada día a crecer como persona.

Abstract

Microvascular endothelial cells at the Blood-Brain Barrier exhibit a protective phenotype, which is highly induced by biochemical and biomechanical stimuli. Amongst them, shear stress, a mechanical force prompted by circulation, enhances junctional tightness and limits transport at capillary-like levels. It has long been proven that abnormal flow patterns reduce functional features of macrovascular endothelium. Hemodynamic and structural alterations such as hypertension or arterial stiffness are examples of vascular conditions that increase shear stress and pulsatility, which reach and affect downstream at the neurovascular unit. Clinical studies have shown that such alterations are relevant in the pathogenesis of neurodegenerative diseases such as types of dementia and multiple sclerosis. In this work, the effects of high shear stress and pulsatile stimuli were evaluated at the cellular level of the Blood-Brain Barrier as the interface between the vascular and cerebral systems.

A dynamic *in vitro* model of the Blood-Brain barrier was designed and characterized in order to allow exposure of microvascular endothelial cells to shear stress and soluble factors produced by neighboring cells in co-culture. Human brain microvascular endothelial cells were exposed to both physiological and pathological flow patterns. Physiologic shear upregulated the expression of tight junction markers Zonula Occludens 1 and Claudin-5. High shear stress and/or pulsatility, decreased their expression to basal levels and altered junctional morphology and P-glycoprotein efflux activity. Furthermore, cells were exposed to altered shear stress patterns followed by restoration of physiological capillary-like conditions. Reversible recovery on the expression of tight junction markers was observed. Flow conditions that disturb barrier phenotype commensurated with junctional signaling pathways. This finding suggests that if flow conditions are restored, the Blood-Brain Barrier functional features may be recovered. Recent evidence of effects of renal denervation in hypertension treatment and Blood-Brain Barrier markers makes this technology a suitable candidate for hemodynamic cerebrovascular restoration.

Renal denervation is a novel technology for treatment of resistant hypertension by ablation of sympathetic nerves in renal arteries. While proven safe, efficacy results in clinical trials are still inconclusive. Understanding arterial microanatomy is critical to predict future efficacy outcomes. An *in vivo* study was performed to evaluate nerve and lymph node distributions around renal arteries and the effect of single and dual denervation treatments. Distal regions of the renal artery were identified as the optimal target locations, as they showed the highest nerve density close to the lumen and the lowest lymph node area. Dual treatment increased circumferential affected arc in renal arteries and have a higher probability to increase efficacy.

Abnormal shear stress inherent to systemic vascular disease leads to Blood-Brain Barrier impairment, which could be reverted by hemodynamic interventions. Renal denervation is a potential therapy that needs to be further characterized in order to correlate its effects on blood pressure decrease and functional features of the Blood-Brain Barrier.

Resumen

Las células endoteliales microvasculares cerebrales de la Barrera Hematoencefálica exhiben un fenotipo protector que está altamente inducido por estímulos bioquímicos y biomecánicos. Entre ellos, la tensión cortante es una fuerza mecánica provocada por la circulación que intensifica la unión celular y limita el transporte a nivel capilar. Distintos estudios han probado que los patrones de flujo anormales reducen las propiedades funcionales del endotelio macrovascular. Las alteraciones hemodinámicas y estructurales, como la hipertensión o la rigidez arterial, son algunos ejemplos de condiciones vasculares que aumentan la tensión cortante y la pulsatilidad, las cuales alcanzan y afectan aguas abajo en la unidad neurovascular. Otros estudios clínicos muestran que dichas alteraciones son relevantes en la patogénesis de enfermedades neurodegenerativas como algunos tipos de demencia y esclerosis múltiple. En este trabajo, se han evaluado los efectos del aumento de la tensión cortante y la pulsatilidad a nivel celular en la Barrera Hematoencefálica como interfaz entre el sistema vascular y cerebral.

Se ha diseñado y caracterizado un modelo *in vitro* dinámico de la Barrera Hematoencefálica para permitir el cultivo de células endoteliales microvasculares y exponerlas a tensión cortante y a factores solubles producidos por células vecinas en cocultivo. Se han expuesto células endoteliales microvasculares cerebrales humanas a patrones de flujo fisiológicos y patológicos. El rango fisiológico aumentó la expresión de los marcadores de unión estrecha Zonula Occludens 1 y Claudina 5. Tanto la tensión cortante elevada como la pulsatilidad disminuyeron la expresión de dichos marcadores a niveles basales y alteraron la morfología de las uniones estrechas y la actividad del transportador activo P-glicoproteína. Además, se expusieron células a tensión cortante alterada seguida por condiciones fisiológicas y se observó una recuperación reversible de la expresión de marcadores de unión estrecha. También se constató que las condiciones hemodinámicas que alteran el fenotipo de barrera correlacionaron con vías de señalización relacionadas con las uniones estrechas. Estos hallazgos sugieren que, en caso de restauración de las condiciones de flujo, las propiedades funcionales de la Barrera Hematoencefálica podrían recuperarse. Evidencias recientes de los efectos de la denervación renal para el tratamiento de la hipertensión y de marcadores de Barrera Hematoencefálica hacen de esta tecnología un candidato apto para la restauración de la hemodinámica cerebrovascular.

La denervación renal es una tecnología novedosa para el tratamiento de la hipertensión resistente que se basa en la ablación de los nervios simpáticos alrededor de las arterias renales. Aunque se ha demostrado su seguridad, los resultados de eficacia obtenidos en estudios clínicos son aún poco concluyentes. El entendimiento de la microanatomía arterial es esencial para predecir futuros resultados de eficacia. Se ha realizado un estudio *in vivo* para evaluar la distribución de nervios y ganglios linfáticos alrededor de arterias renales y el efecto de tratamientos de denervación sencillos y dobles. Se identificaron las regiones distales de la arteria renal como localizaciones óptimas para el tratamiento ya que estas presentaron mayor densidad de nervios cercanos a la pared arterial y la menor área de ganglios linfáticos. El tratamiento doble incrementó el arco circunferencial afectado en las arterias renales y por lo tanto presenta una mayor probabilidad para incrementar la eficacia.

Los patrones de tensión cortante anormales, inherentes a enfermedades vasculares sistémicas, conducen al deterioro de la Barrera Hematoencefálica. Éste puede corregirse mediante intervenciones hemodinámicas. La denervación renal es un tratamiento con potencial que necesita una mayor caracterización para poder correlacionar sus efectos en la presión sanguínea y las propiedades funcionales de la Barrera Hematoencefálica.

Resum

Les cèl·lules endotelials microvasculars cerebrals de la Barrera Hematoencefàlica exhibeixen un fenotip protector que està altament induït per estímuls bioquímics i biomecànics. Entre aquests, la tensió tallant és una força mecànica provocada per la circulació que intensifica la unió cel·lular i limita el transport a nivell capil·lar. Diferents estudis han provat que els patrons de flux anormals redueixen les propietats funcionals de l'endoteli macrovascular. Les alteracions hemodinàmiques i estructurals, com la hipertensió o la rigidesa arterial, són alguns exemples de condicions vasculars que augmenten la tensió tallant i la pulsatilitat, les quals arriben i afecten aigües avall a la unitat neurovascular. Altres estudis clínics mostren que aquestes alteracions son rellevants en la patogènesi de malalties neurodegeneratives com alguns tipus de demència i esclerosi múltiple. En aquest treball, s'han avaluat els efectes de l'augment de la tensió tallant i la pulsatilitat a nivell cel·lular a la Barrera Hematoencefàlica com a interfase entre el sistema vascular i cerebral.

S'ha dissenyat i caracteritzat un model *in vitro* dinàmic de la Barrera Hematoencefàlica per a permetre el cultiu de cèl·lules endotelials microvasculars i exposar-les a tensió tallant i a factors solubles produïts per cèl·lules veïnes en cocultiu. S'han exposat cèl·lules endotelials microvasculars cerebrals humanes a patrons de flux fisiològics i patològics. El rang fisiològic va augmentar la expressió dels marcadors d'unió estreta Zonula Occludens 1 i Claudina 5. Tant la tensió tallant elevada com la pulsatilitat van disminuir l'expressió d'aquests marcadors al nivell basal i van alterar la morfologia de les unions estretes i la activitat del transportador actiu P-glicoproteïna. A més, es van exposar cèl·lules a tensió tallant seguida per condicions fisiològiques i es va observar una recuperació reversible de l'expressió dels marcadors d'unió estreta. També es va constatar que les condicions hemodinàmiques que alteren el fenotip de barrera van correlacionar amb vies de senyalització relacionades amb les unions estretes. Aquestes troballes suggereixen que, en cas de restauració de les condicions de flux, les propietats funcionals de la Barrera Hematoencefàlica podrien recuperar-se. Evidències recents dels efectes de la denervació renal pel tractament de la hipertensió i dels marcadors de Barrera Hematoencefàlica fan d'aquesta tecnologia un candidat apte per la restauració de la hemodinàmica cerebrovascular.

La denervació renal és una tecnologia innovadora pel tractament de la hipertensió resistent que es basa en l'ablació dels nervis simpàtics al voltant de les arteries renals. Tot i que s'ha demostrat la seva seguretat, els resultats d'eficàcia obtinguts en estudis clínics són encara poc concloents. La comprensió de la microanatomia arterial és essencial per predir futurs resultats d'eficàcia. S'ha realitzat un estudi *in vivo* per avaluar la distribució de nervis i ganglis limfàtics al voltant d'arteries renals i l'efecte de tractaments de denervació senzills i dobles. Es van identificar les regions distals de l'arteria renal com a localitzacions òptimes pel tractament, donat que aquestes van presentar una major densitat de nervis propers a la paret arterial i una menor àrea de ganglis limfàtics. El tractament doble va incrementar l'arc circumferencial afectat en les arteries renals i per tant presenta una probabilitat més elevada per incrementar l'eficàcia.

Els patrons de tensió tallant anormals, inherents a malalties vasculars sistèmiques, condueixen al deteriorament de la Barrera Hematoencefàlica. Aquest pot corregir-se mitjançant intervencions hemodinàmiques. La denervació renal és un tractament amb potencial que necessita una major caracterització per poder correlacionar els seus efectes a la pressió sanguínia i a les propietats funcionals de la Barrera Hematoencefàlica.

Table of Contents

List of abbreviations, magnitudes and units

Abbreviations

ABC	ATP-Binding Cassette
ACM	Astrocyte Conditioned Medium
AD	Alzheimer's Disease
AJ	Adherens Junction
AM	Astrocyte Medium
BBB	Blood-Brain Barrier
bFGF	Basic Fibroblast Growth Factor
BL	Basal Lamina
CAD	Computer-Aided Design
CD31	Cluster of differentiation 31 - Platelet Endothelial Cell Adhesion Molecule 1
CFD	Computer Fluid Dynamics
CNS	Central Nervous System
DFS	Dynamic Flow System
DMEM	Dulbecco's Modified Eagle Medium
EBD	Evans Blue Dye
EBM-2	Endothelial Basal Medium 2
ECM	Extracellular Matrix
EDCM	Endothelial Dynamic Culture Medium
EGM-2	Endothelial Growth Medium 2
ERK	Extracellular signal-Regulated Kinase
FBS	Fetal Bovine Serum
FDA	Food & Drug Administration
Fn	Fibronectin
GFAP	Glial Fibrillary Acidic Protein
GLUT1	Glucose Transporter 1
GPCR	G-Coupled Protein Receptor
HA	Human Astrocytes
HBMEC	Human Brain Microvascular Endothelial Cells
IGS	Initial Graphics Exchange Specification
JAM	Junctional Adhesion Molecule
JNK	c-Jun N-terminal Kinase
LN	Lymph Node
LRP1	Low-density lipoprotein Receptor-related Protein-1
MAGUK	Membrane-Associated Guanylate Kinase-Like
MMP	Matrix Metalloproteinase
MS	Multiple Sclerosis
MTT	3-(4,5-dimethylthiazol-2-yl)-2,5-diphenyltetrazolium bromide
NEPI	Norepinephrine
NVU	Neurovascular Unit
PBS	Phosphate Buffered Saline
PDMS	Polydimethylsiloxane
P-gp	P-glycoprotein
PLL	Poly-L-Lysine
PPFC	Parallel-Plate Flow Chamber
PS	Penicilin+Streptomycin
PSG	Penicilin+Streptomycin+Glutamine
RA	Renal Artery
RDN	Renal Denervation
ROS	Reactive Oxygen Species
SLC	Solute-Like Carrier
SPSHR	Stroke-Prone Spontaneously Hypertensive Rat
TCA	Trichloroacetic Acid
TCP	Tissue Culture Plate
TEER	Transendothelial Electrical Resistance
TJ	Tight Junction
TNF-α	Tumor Necrosis Factor α
VEGF	Vascular Endothelial Growth Factor
ZO	Zonula Occludens

Magnitudes and units

A	Cross-sectional area [cm^2]
B	Bottom fluorescence [RFU]
d	Diameter [mm]
h	PPFC height [mm]
L	Vessel length [mm]
Le	Entrance length [mm]
P_e	Permeability [cm/s]
Q	Flow [mL/s]
R	Vessel resistance [mmHg·s/mL]
r	Radius [mm]
R_e	Reynolds number [1]
T	Top fluorescence [RFU]
t	Time [s]
v	Velocity [cm/s]
V_B	Bottom compartment volume [mL]
w	PPFC width [mm]
ΔP	Pressure gradient [mmHg]
μ	Viscosity [cP]
ρ	Density [g/cm^3]
τ	Shear stress [dyn/cm^2]

List of figures and tables

Figures

Tables

Collaborations and funding

This thesis has been possible thanks to the combined effort of several researchers and laboratories. Here is a detailed list of collaborators and funding sources that have facilitated the success of this thesis.

Dr. Mercedes Balcells supervised every step of the thesis with additional support from Dr. José Javier Molins Vara and Dr. Jordi Martorell López. Dr. Elazer Edelman gently offered oversight to the whole project.

The design and manufacture of the parallel-plate flow chamber was possible thanks to Dr. Andrés A. García-Granada and César Alquézar from the industrial engineering department at IQS, from Paula del Rey and Sina Salehi Omran who collaborated at MIT and finally from Oriol Bosch who collaborated at IQS.

All *in vitro* experiments were performed at MIT and IQS. Design of experiments would not have been possible without the expertise of Dr. Pedro Melgar-Lesmes and the insights of Dr. Caroline O'Brien, both from Dr. Edelman's Harvard-MIT Biomedical Engineering Center at MIT.

In vivo preliminary studies with rats were performed at Institut Hospital del Mar d'Investigacions Mèdiques (IMIM), Parc de Recerca Biomèdica de Barcelona (PRBB). Dr. Jaume Roquer, Dr. Angel Ois and Dr. Alessandro Principe provided invaluable insights in the design of animal experiments and performing animal surgeries.

Renal denervation animal studies were performed at CBSET, Inc. with the collaboration of Dr. Rami Tzafriri, Dr. John Keating, Anna Spognardi, Lynn Bailey and Peter Markham.

The project used funds from different sources, listed here:

- Banco Santander (Beca Fórmula Santander 2013).
- IQS School of Engineering (Beca de doctorado 2016).
- Ministerio de Economía y Competitividad SAF2013-43302-R
- NIH grant R01 GM 49039
- Fundació Empreses IQS
- CBSET grants from multiple medical device companies

1. Introduction

1.1. The Brain and the Blood-Brain Barrier

1.1.1. The concept of the Blood-Brain Barrier

While traditional neuroscience has focused on neurons as well as their interactions with the glial cells that support their function, increasing evidence has shifted the field of study towards a well-structured neurovascular unit (NVU). Such unit is involved in the regulation of the blood flow in the brain and adds the brain microvascular domain to the aforementioned neurons and glia. The endothelial cells that line cerebral microvessels form a selective barrier that separates the central nervous system (CNS) from the peripheral circulatory system. Historically, this biological barrier has been referred as the Blood-Brain Barrier (BBB) (Figure 1.1).[1]

Paul Ehrlich provided the first experimental evidence of the existence of a BBB in 1885, when he reported that after a parental injection of a variety of dyes in adult animals, all organs were stained except the brain and the spinal cord.[2] This fact, together with further phenomena observation, lead to the introduction of the term *Bluthirnschranke*, Blood-Brain Barrier, by Max Lewandowsky in 1900.

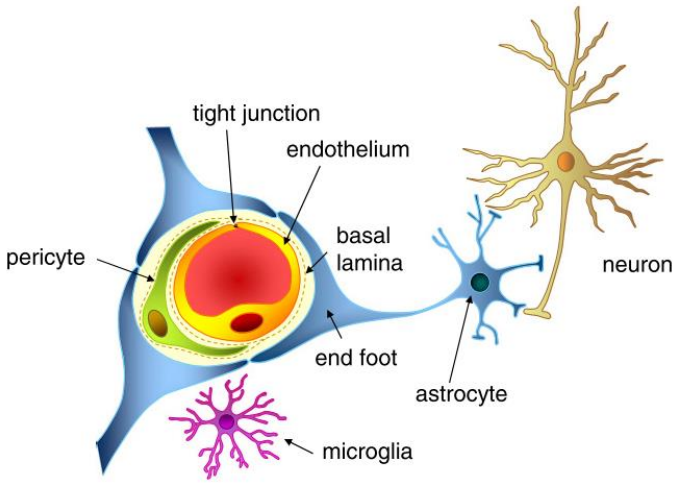

Figure 1.1. Neurovacular unit at capillary level, showing the close association of the different cell types that compose it.[3]

1.1.2. Functions of the Blood-Brain Barrier

Several roles have been attributed to the BBB. One of the main functions of the BBB is the regulation of the nutrition of the brain. Specific transport systems ensure the appropriate nutrient supply providing the BBB with a low passive permeability to many essential hydrophilic metabolites and nutrients required by the CNS. The BBB also mediates the efflux of waste products from the brain to the blood and protects the brain from the entrance of neurotoxic compounds circulating in the blood. This protective function involves an active pumping of

endogenous metabolites or xenobiotics by ATP-binding cassette (ABC) transporters out of the CNS into the blood. Optimal ionic composition of the medium for neuronal function is ensured by the BBB by restricting ionic and fluid transport by specific solute-like carriers (SLC), such as ionic transporters and channels. This ionic regulation is essential to maintain the concentrations of Ca^{2+}, K^{+}, Na^{+} and Mg^{2+} in the narrow range required for proper synaptic neuronal signaling, as well as the pH. Ionic movement restriction leads to a transendothelial electrical resistance (TEER) higher than 1000 Ω/cm^2, in contrast to peripheral capillaries with 2 – 20 Ω/cm^2.

The BBB also helps to keep separate the pools of neurotransmitters and neuroactive agents from central and peripheral nervous systems, allowing their use in both systems independently. Additionally, it controls neural tissue release of glutamate, a neuroexcitatory with high concentration fluctuation after ingestion and potential neurotoxic.[1,4] The BBB is also a barrier for macromolecules traveling from the blood to the brain, such as albumin or plasminogen, proteins inducing cellular activation in the nervous tissue that can lead to cellular apoptosis.[5] This allows maintenance of total protein content on both sides of the barrier, with blood plasma concentration having a higher protein concentration than the cerebrospinal fluid (CSF).

Overall, the BBB is an essential barrier for the homeostasis of the brain.[6,7]

1.1.3. The endothelial frontier

As in most endothelia, transcellular route of molecules across the BBB is forced as opposed to paracellular pathways. This is a consequence of the presence of complex tight junctions (TJ) existing between adjacent brain microvascular endothelial cells. Anatomically, endothelial cells in microcapillaries differ from those in the periphery by an increased mitochondrial content, lack of fenestrations, minimal pinocytotic activity and the presence of TJ.[8] Small gaseous molecules such as CO_2 or O_2 and small lipophilic agents such as ethanol diffuse freely through the lipid membranes of endothelial cells. The traffic of small hydrophilic compounds is regulated by specific transport systems on both luminal and abluminal sides of the endothelium, thus providing a transport barrier that selectively facilitates the entry of nutrients and excludes or effluxes harmful compounds.[3] In addition, intracellular and extracellular enzymes that metabolize bloodborne neuroactive solutes provide an additional metabolic barrier. In general, large hydrophilic compounds are transferred by specific receptor-mediated transcytosis or otherwise excluded.[9]

a) Junctions of the BBB endothelium

The endothelium of the brain microvasculature is characterized by a junctional complex that includes adjerens junction (AJ) and TJ, which contribute to the paracellular permeability restriction across the BBB. AJ stabilize cell-cell interactions in the junctional zone, mediate contact inhibition during vascular remodeling and growth and initiate cell polarity. The principal component of AJ is VE-cadherin, which mediates adhesion between adjacent cells through Ca^{2+} regulation and is linked to the cytoskeleton via catenins. Another AJ protein, platelet-endothelial cell adhesion molecule (PECAM or CD31), has an important role in monocyte transmigration across the CNS endothelium even though it is not structurally associated with TJ.[8]

The main molecular components of the TJ are classified into the integral transmembrane proteins and the cytoplasmic adaptor proteins, linked to the actin cytoskeleton, as depicted in Figure 1.2.

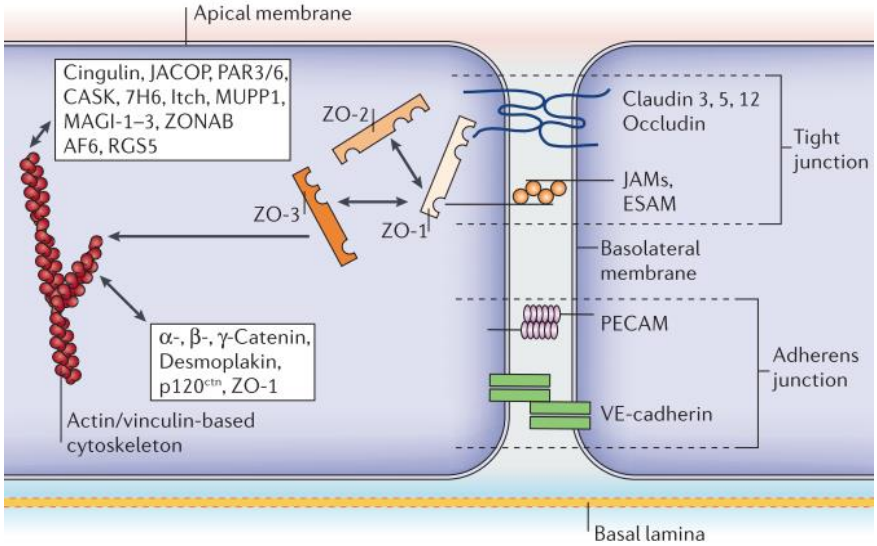

Figure 1.2. Molecular composition of endothelial tight junctions and adherens junctions.[1]

Transmembrane proteins are composed by junctional adhesion molecules (JAM), claudins and occludin. JAMs have been reported as the first members of the IgG superfamily to contribute to TJ and are believed to mediate the early attachment of adjacent cell membranes.[10] Occludin was the first transmembrane TJ discovered[11] and might have a function in TJ modulation but is not essential for its formation. Claudins establish barrier properties and form a family of more than 20 member proteins[12,13], whose selective expression and combinations is specific to certain tissues and determines the barrier function contributing to the TEER.[14]

Adaptor cytoplasmic proteins, including members of the membrane-associated guanylate kinase-like (MAGUK) family,[15] form large complexes known as the cytoplasmic plaque, anchoring transmembrane proteins with the cellular cytoskeleton. Three proteins in this family have been identified in the formation of TJ, the Zonula Occludens (ZO) family including ZO-1, ZO-2 and ZO-

3. The dissociation of these proteins causes an increase in permeability as they stabilize TJ through the link of transmembrane proteins with the cytoplasm. ZO-1 acts as a signaling molecule and has been shown to localize to the nucleus in proliferation and injury conditions. Second order adaptor proteins include cingulin and afadin.[16]

Besides the restriction of paracellular permeability, TJ play a key role in the polarization of the endothelium, segregating the cell membrane in apical and basal domains. Also, several intracellular signaling pathways regulate changes in expression, subcellular location, post-translational modifications and protein-protein interaction under pathological and physiological conditions. The regulation of TJ organization and function at the BBB involves mainly calcium, phosphorylation and G-protein pathways.[17]

b) BBB transport systems

In addition to the structural elements that ensure the tightness of the BBB, different transport systems present in the endothelium are essential for the correct brain function (Figure 1.3). Brain nutrition relies on molecular carriers present at both apical and basolateral sides of the brain endothelium and selectively transport hexoses (glucose transporter 1 or GLUT1), aminoacids (large neutral amino acid transporters), monocarboxylic acids, nucleosides, amines and vitamins. Ionic transport is accomplished equally with selective ion transporters such as the Na^+/K^+ ATPase pump, which maintains high Na^+ gradient at the BBB, and the Na^+/H^+ and Cl^-/HCO_3^- exchangers, which play important roles regulating the pH.

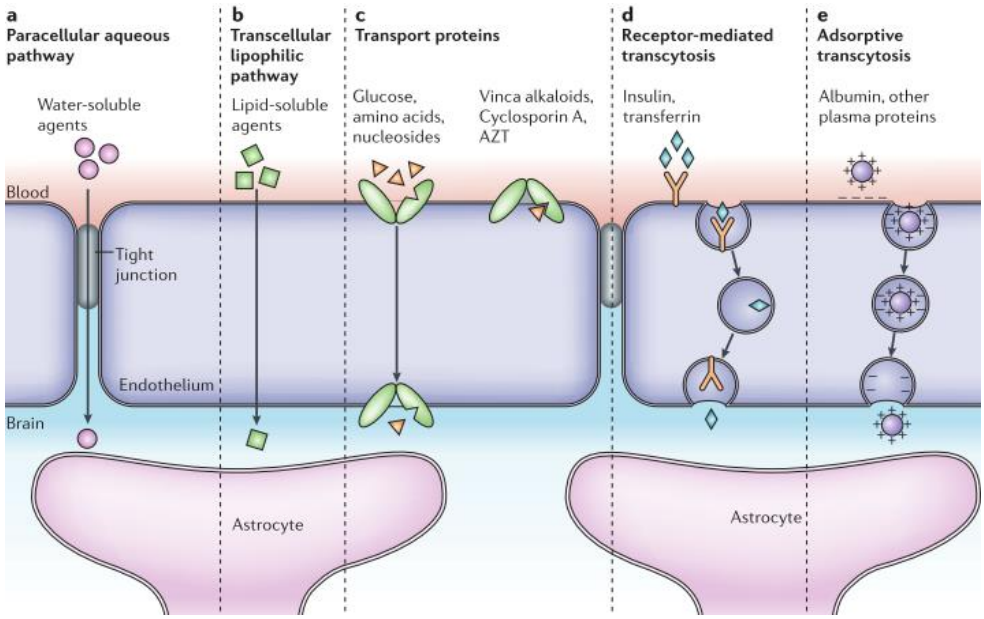

Figure 1.3. Transport pathways across the Blood-Brain Barrier.[1]

While TJ severely restrict the paracellular pathways for hydrophilic molecules, the large surface area of the endothelium membranes ensures an efficient transcellular route for lipophilic molecules, which is the entry route of most CNS drugs. A large number of molecules expected to penetrate into the CNS have a much lower entry rate than expected. These substances are actively effluxed from the brain by members of the ATP-binding cassette transporters (ABC transporters).[18,19] Among these neuroprotective transporters, P-glycoprotein (P-gp), multidrug resistance-associated proteins (MRP) and breast cancer resistant proteins (BCRP) are the most abundant.[6] While most of the studies specify that these efflux transporters are located in the luminal side of endothelial cells to transport molecules to the blood, there is some controversy regarding transporter polarization.[20] Figure 1.4 depicts typical locations of common ABC transporters in the BBB, where only those located in the luminal side are relevant in efflux transport. Receptor-mediated transcytosis, which involves binding of a ligand to a specific receptor, take up large proteins such as insulin, low-density lipoprotein and transferring, as well as neuroactive peptides, cytokines and chemokines. Polycationic molecules binding to negative charges on the plasma membrane initiate absorptive-mediated endocytosis and transcytosis. The latter is the responsible of albumin uptake upon its cationization, otherwise being poorly transported.[16]

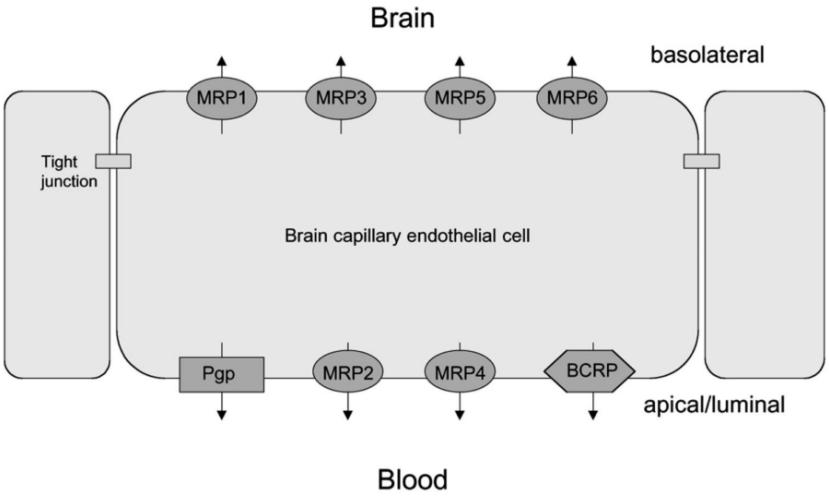

Figure 1.4. Localization of selected ATP-binding cassette transporters in brain microvascular endothelial cells.[21]

1.1.4. Other components of the neurovascular unit

While in larger vessels (arterioles, arteries and veins) there is a continuous layer of smooth muscle cells, brain capillaries are surrounded by astrocytes, pericytes, microglia and neuronal processes. It has long been thought that this close cell-cell association is responsible for the induction and/or maintenance of the BBB phenotype in the capillary brain endothelium.

a) Astrocytes

Astrocytes are complex and external stimuli sensitive cells which show over eleven distinct phenotypes, eight of which are specifically related with the brain microvascular environment. Their anatomy is characterized by abundant end-foot processes that come in contact with neuronal synapses and surround the cerebral microvascular endothelium. The purpose of this complex anatomy is thought to be the control of brain water and ionic homeostasis in order to optimize the interstitial space for synaptic transmission.[22] Astrocytes are involved in the metabolism of neurotransmitters, regulation of extracellular pH and K^+ concentration, immunoresponse and the structural and functional integrity of the BBB.[23]

Several specialized features at the astrocytic endfeet are responsible of water and ion transport in the CNS, including a high density of orthogonal arrays of particles (OAPs), aquaporin water channel (AQP4) and the Kir 4.1 K^+ channel. The polarization of these proteins correlates with the expression of agrin, a heparin sulfate proteoglycan on the basal lamina that accumulates in brain microvessels at the time of BBB tightening during development.[16] The most common specific astrocytic marker is the glial fibrillary acidic protein (GFAP), which plays a role in cell-cell communication.

Astrocytes are able to induce morphological, biochemical and functional barrier features of the BBB phenotype in endothelial cells *in vitro*. Several studies show that brain endothelial cells either co-cultured with astrocytes or exposed to astrocyte-conditioned medium (ACM) increase their TJ expression, TEER and enzymatic activity, and upregulate specific transporters such as GLUT1 or P-gp.[24] These findings suggest an active role played by soluble factors secreted by astrocytes in BBB phenotype modulation. Several molecules have been associated with endothelial regulation such as glial-derived neurotrophic factor, transforming growth factor β-1, basic fibroblast growth factor, interleukin 6 and angiopoietin 1.[25] However, due to the dedifferentiation process experienced by mammalian cells when cultured *in vitro*, caution must be used in the interpretation of these results. In contrast to the *in vitro* evidence, several studies argue about the role of astrocytes *in vivo*. For example, certain aspects of the BBB become functional during development before the appearance of astrocytes.[26]

b) Pericytes

Brain pericytes are associated with the stabilization of small blood vessel architecture, neurovascularization and angiogenesis. They are responsible for BBB gene specific expression patterns in brain endothelial cells and induce the polarization of the astrocytic endfoot processes.[25] Pericytes play a key role in several CNS pathologies and release different growth factors and angiogenic molecules that regulate brain endothelium. They influence vascular blood flow through contraction and relaxation and are also involved in the immune responses at the BBB.[27] Historically, astrocytes were considered the main barrier phenotype inductor at the BBB[28], leading *in vitro* models to endothelial-astrocyte co-culture configurations. Later evidence of the importance of pericytes in BBB function[29] has increased the number of models that include these cells in co- or tri-culture configurations.[30,31]

c) Basal lamina

In addition to the cellular components that contribute to the BBB, the extracellular matrix (ECM) of the basal lamina (BL) interacts with cells and separates them. Different extracellular matrix proteins such as collagen IV, fibronectin, laminin and proteoglycans form the BL. Besides cell-cell interaction, cell-matrix plays a key role in BBB regulation. The BL exists as two distinct forms, either produced by astrocytes or by endothelial cells, or as a fusion of both, creating a BL composite.[32] During angiogenesis, integrins that link cells to the ECM play a key role in mediating endothelial signaling, brain capillary formation and cell migration. Fibronectin, for instance, has shown significant benefits in *in vitro* cultures by inducing cell survival and proliferation[33] and increasing TEER.[34] An increase in permeability in the BBB in pathological states is strongly associated with a disruption of the BL.[35]

1.1.5. Alteration of the Blood-Brain Barrier in disease

The failure of the BBB is involved in the progression of a great number of pathologies that affect the CNS.[8,36] The relationship between pathology and barrier phenotype depends on the specific disease. In some cases, increased BBB permeability is consequence of the pathology, such as ischemic stroke,[37,38] whereas in other cases it remains unclear whether BBB dysfunction plays a role in the onset of the disease, such as with multiple sclerosis (MS)[39,40], epilepsy[41] or Alzheimer's disease (AD).[42] Depending on the disease, different molecular mechanisms are involved in BBB disruption, including VEGF, MMPs, cytokines and reactive oxygen species (ROS).[43]

During ischemic stroke and traumatic brain injury there is production of a mediator of inflammation, bradykinin, which stimulates the expression and secretion of IL-6 by astrocytes and increases BBB permeability.[44] Not only the access of molecules to the CNS is increased, but also the entry of macrophages and neutrophils. BBB breakdown in multiple sclerosis is also associated to inflammation. MS is characterized by an autoimmune attack on CNS components that leads to impairment of motor and sensory functions. Progressive MS is mediated by an inflammatory response driven by immune cells trapped behind the BBB.[45] TJ proteins are highly downregulated in active lesion areas but also in areas of normal-appearing white matter.[46]

In the case of epilepsy, which is characterized by recurrent seizures, the expression level of key transport markers of the BBB is highly involved. GLUT1 deficiency can lead to epileptic syndrome[47] and overexpression of P-gp and MDR hinder disease treatment.[48] In infectious diseases such as bacterial meningitis and sepsis, the increase of BBB permeability is mainly caused by the effect of bacterial endotoxin lipopolysaccharide.[49]

The main pathological features of Alzheimer's disease are the presence and accumulation in the brain of amyloid-β (Aβ) peptides and neurofibrillary tangles. BBB disruption in AD is thought to be related to the low-density lipoprotein receptor-related protein-1 (LRP1)[50], as the main responsible of Aβ brain clearance. Abnormal amyloid clearance across blood vessels is lower than the production rate, leading to higher plaque accumulations in the brain. Addition of hypoxic or ischemic insults in AD may accelerate the plaque accumulation process.[51]

Biomechanical forces induced by blood circulation along the BBB are critical in the performance of the BBB in health and disease. As this is a major aspect in the hypothesis and development of this thesis, a detailed description of the link between vascular alterations and cerebral effects will be detailed in Chapter 1.2.2.

1.1.6. *In vitro* models of the Blood-Brain Barrier

Neurological diseases affect millions of people worldwide. In 2015, the World Health Organization (WHO) estimated the prevalence of all sorts of neurological disorders to be 1050 million worldwide. In the same year, 7.5 million deaths would be associated to such diseases. In 2030, prevalence and mortality are projected to increase by 8% and 19%, respectively.[52]

Currently, the CNS drug industry is the second largest therapeutic industry. The average time for a CNS drug to get to market (12 – 16 years) is 4 years higher than non-CNS drugs (10 – 12 years).[24] Discovery and development of CNS novel drugs takes longer because of the complexity of the brain and the insufficient CNS exposure to the drug due to the inability of drugs to cross the BBB.[25] Among the different types of BBB models, *in vitro* modeling has become the fastest tool to evaluate drug permeability across the BBB[53–56] in studies prior to preclinical animal models targeting the CNS.

Reproducing the functional properties and physiological responses of the BBB in the microvascular environment is extremely challenging. Currently, no specific *in vitro* model of the BBB is used as a reference standard in the pharmaceutical industry. The phenotypic drift that cells undergo once isolated from their anatomical environment limits proper recapitulation of *in vivo* conditions. Brain microvascular endothelial cells rapidly lose their barrier phenotype and acquire generic endothelial cell properties with no tight junction formation.[57,58] However, a wide variety of *in vitro* models have been developed as tools not only for drug permeability studies but also for the study of basic physiology, elucidation of drug interactions at the BBB and performance of physiopathological, toxicological and immunological studies.[3,24,59–62]

The main features required for a useful BBB *in vitro* model are proper expression and localization of TJ, presence of specific transporters, functional efflux mechanisms, drug metabolizing enzymes as well as permeability and TEER values similar to the *in vivo* ones. Moreover, models should promote the exposure to biochemical and biomechanical stimuli that play a role in the modulation of the BBB both in physiological and pathological states. Finally, *in vitro* models should provide a reproducible, regulated and easy to establish and scale-up system.[63] Different factors are considered in order to attempt to reestablish and maintain BBB features.

a) Cell source

Primary human brain microvascular endothelial cells (HBMEC) are the ideal option to reproduce human *in vivo* conditions. However, the limited availability of these cells, the concern about the health of the brain source and the rapid loss of phenotype restrict its use for high throughput studies. The most established and well characterized BBB models incorporate primary animal brain cells from porcine, bovine, rat and mouse origin. The main inconvenient of extrapolating animal model data to human is the interspecies differences. As a consequence, considerable efforts have been made to establish stable human cell lines.[24] The most characterized and widely used human cerebral endothelial cell lines is the hCMEC/D3, which is derived by a primary culture immortalized by lentiviral vector transduction with the catalytic subunit of the human telomerase and the oncogene SV40 large T antigen.[64] Over 100 studies have been published with this cell line focused on different aspects of cerebral endothelial biology and pharmacology.[65] Another interesting approach has recently started to be studied regarding the use of human pluripotent stem cells. This approach involves an initial co-differentiation of both endothelial and neural cells, followed by a purification and further maturation of the endothelium in order to achieve a complete BBB phenotype.[66,67]

b) Co-culture with other NVU components

As above mentioned, other cellular components of the NVU play a crucial role in the barrier phenotype of HBMEC. Several models, incorporating astrocytes, pericytes and/or neurons, have been studied, characterized and validated. The most common setup for the establishment of co-cultures is a porous membrane that allows endothelial cell exposure to astrocyte soluble factors and direct contact interactions depending on membrane porosity and thickness. Typical transwell inserts contain a porous membrane bottom and fit in standard culture well plates, dividing the well into two adjacent chambers. This setup allows different cell configurations (Figure 1.5), being the upper chamber the luminal side (apical side) and the bottom chamber the abluminal one (basolateral side).

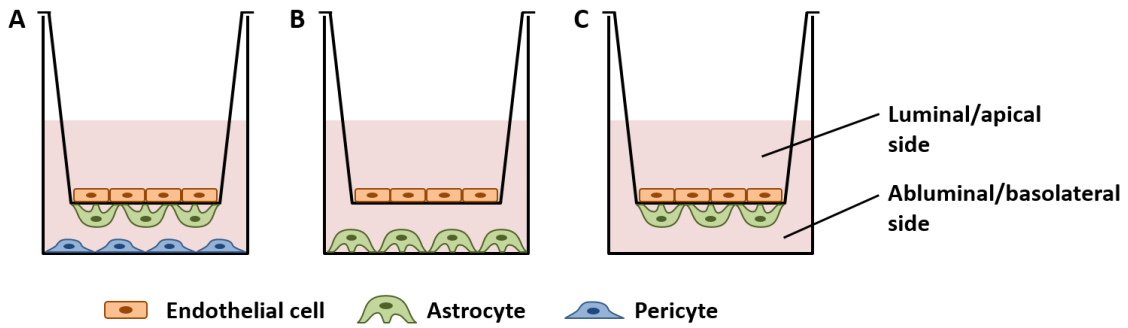

Figure 1.5. Different *in vitro* model cell configurations in the transwell insert.

The main advantages of this setup are the high throughput capacity, low cost and easiness to culture and perform TEER and permeability assays. This culture system, however, lacks of biomechanical stimuli such as shear stress and is built upon a 10-200 µm porous membrane, which is at least 80 times thicker than the basal lamina (40 – 120 nm).[68]

c) Dynamic models

Vascular endothelial cells express a wide range of mechanosensors, described in Chapter 1.2.2, that transduce the stimuli generated by flow-induced shear stress into biochemical signals.[69,70] Mechanosensor signaling pathways involve cell differentiation, division, apoptosis and migration patterns. Exposure of HBMEC to flow is a requirement to obtain and maintain a proper BBB phenotype.[71] Current *in vitro* dynamic BBB models that enable exposure of HBMEC to flow include different flow exposure techniques, such as the parallel-plate flow chamber (PPFC), hollow fiber based bioreactors and microfluidic systems (Figure 1.6).

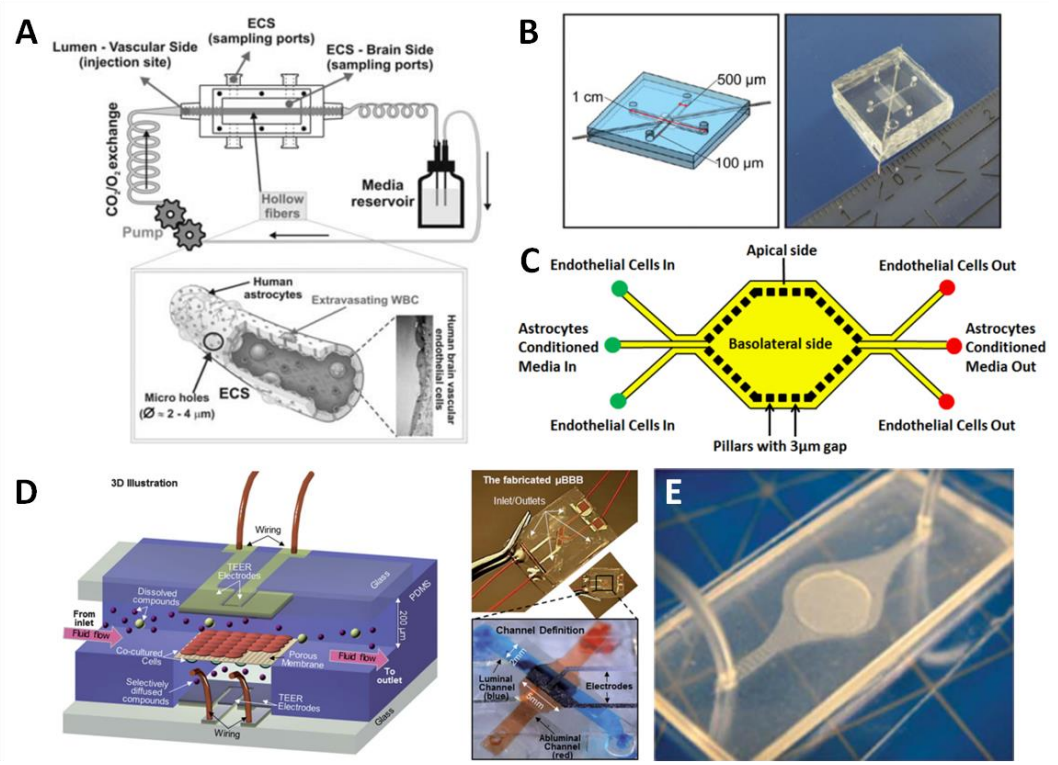

Figure 1.6. Current dynamic *in vitro* BBB models: (A) DIV-BBB,[72] (B) BBB-on-chip,[73] (C) Sym-BBB,[74] (D) µBBB,[75] and (E) NVU on a chip.[76]

PPFC allow study of physiological and morphological responses of HBMEC and are commonly used for the evaluation of transendothelial migration, chemotaxis and leukocyte-endothelial interactions.[77] This type of device is imaging-compatible and allows a controlled and reproducible shear stress exposure. However, co-culture is not possible in the PPFC.

Hollow fiber based *in vitro* models, such as the DIV-BBB, aim to mimic brain microvessels in porous polymeric capillaries with endothelial cells on the luminal side and glial cells on the outer surface. It provides better anatomical resemblance, proper exposure to flow and *in situ* TEER monitoring. Despite these benefits, the DIV-BBB does not allow cell imaging, it requires a large number of reagents and cells and capillary fibers have higher thicknesses than the porous membranes in static setups (>200µm).

Over the last years, aiming towards a more physiologically relevant, dynamically monitored, low-cost and high throughput platform, several unique microfluidic cerebrovascular models have been developed.[73–76] They differ in complexity and functionality, but most of them are made of PDMS and still incorporate a porous membrane to enable glial co-culture. Even though further characterization of BBB markers is needed to improve the relevance of the models, microfluidics offer the alternative to current static and dynamic models in order to make a platform for suitable high throughput CNS drug-screening model. However, the size of this kind of model limits the yield of proteomic and genomic concentration for expression assays.

d) 3D cell culture

Proper three dimensional (3D) cellular organization and structure are required for appropriate positioning effects, polarization, differentiation, cell-cell interactions and dynamics. However, the use of 3D scaffolds for BBB modeling is still limited. Development of scaffolds that are simple, reproducible and can withstand mechanical stimuli such as shear stress remains a challenge. Currently, the development of 3D platforms has different approaches. Collagen I[78,79] is a typical biomaterial used in 3D hydrogel scaffolds, either by itself or in combination with hyaluronic acid[80], alginate[81] or electrospun nanofibers.[82] Such models may allow study of the interaction between the NVU cellular components[58,83] in compartmentalized areas.[84] Some designs have combined microfluidic chips with 3D environments, creating microchannels within collagen I matrices populated with glial cells where endothelial cells were seeded and formed stable *in vitro* capillaries with significant low permeability.[85,86]

1.2. Hemodynamics

1.2.1. Fluid dynamics in vasculature

Hemodynamics is the branch of physiology that is concerned with the mechanical and physiological properties governing blood circulation through the body.[87] The main parameters that dictate this vascular environment are blood pressure and flow (Q). The energy of blood as a fluid is exerted by blood pressure in three interchangeable forms, which is lateral pressure (force exerted on the walls of the vessel), kinetic energy and gravitational forces. Blood circulation occurs from a region of higher pressure towards a region of lower pressure (ΔP) and is inversely affected by the vessel resistance (R) to flow (Equation 1.1).

$$Q = \frac{\Delta P}{R}$$ **Equation 1.1**

Blood is not an ideal fluid, which is translated into a loss of pressure when blood flows through the vasculature. Resistance to flow depends on kinetic viscosity (μ), vessel radius (r) and length (L). Such relationship is known as the Hagen-Poiseuille law (Equation 1.2), which allows the estimation of blood flow after pressure measurements (Equation 1.3).

$$R = \frac{8 \cdot \mu \cdot L}{\pi \cdot r^4}$$ **Equation 1.2**

$$Q = \frac{\pi \cdot r^4 \cdot \Delta P}{8 \cdot \mu \cdot L}$$ **Equation 1.3**

However, this law is just an approximation as it is based on the assumptions that blood viscosity is constant, vessels are rigid, cylindrical and with a significantly high length/diameter ratio and flow is steady, non-pulsatile and non-turbulent. The dimensionless Reynolds number (Equation 1.4) provides information on the regime of a flow in a pipe. Flow regimes with Reynolds number below 2000 are considered laminar and turbulence is reached beyond that number.

$$Re = \frac{\rho \cdot v \cdot d}{\mu}$$ **Equation 1.4**

Blood flow is typically laminar. A gradient of frictional wall resistance between fluid in contact with the wall and the center of the vessel generates a parabolic flow profile. When turbulence occurs in blood vessels, flow patterns are chaotic and linearity between flow and pressure is lost. In order to maintain flow, pressure gradients need to be larger. In complex vascular geometries such as arterial bifurcations or aneurysms, turbulent flows can develop and induce endothelial cell damage.[88]

1.2.2. Mechanotransduction: Effect of blood flow in the endothelium

Blood circulation along the vascular tree leads to the development of different mechanical forces affecting vessel walls and cells within them (Figure 1.7). On one hand, pulse pressure variations induce circumferential stress, a normal force which is perpendicular to flow direction and induces stretching of all vessel cellular layers (intima, media and adventitia). On the other hand, shear stress (τ, Equation 1.5), a tangential force, is directly induced by blood flow and involves cellular deformation and stretching following flow direction in endothelial cells only.[89]

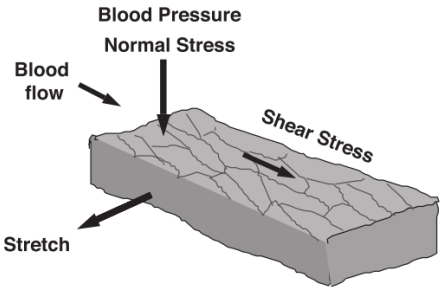

Figure 1.7. Schematic representation of mechanical forces induced by blood flow.[90]

$$\tau = \mu \cdot \left.\frac{\partial v}{\partial y}\right|_{y=0} = \frac{4 \cdot \mu \cdot v}{r} = \frac{4 \cdot \mu \cdot Q}{\pi \cdot r^3}$$ **Equation 1.5**

It has been known for decades that mechanical forces induced by flow modulate endothelial functions.[69,70,91] The concept of mechanotransduction describes how endothelial cells sense mechanical stimuli through membrane receptors. These components, also known as mechanosensors, include integrins[92], receptor tyrosine kinases (RTK)[93], G-protein coupled receptors (GPCR)[94], ion channels[95], primary cilia[96] and glycocalyx.[97] Following specific mechanisms, cells sense shear stress and activate signaling pathways related to a wide range of cellular aspects such as gene expression[98,99], cell proliferation[100], apoptosis[101], adhesion[102] or permeability[103] (Figure 1.8).

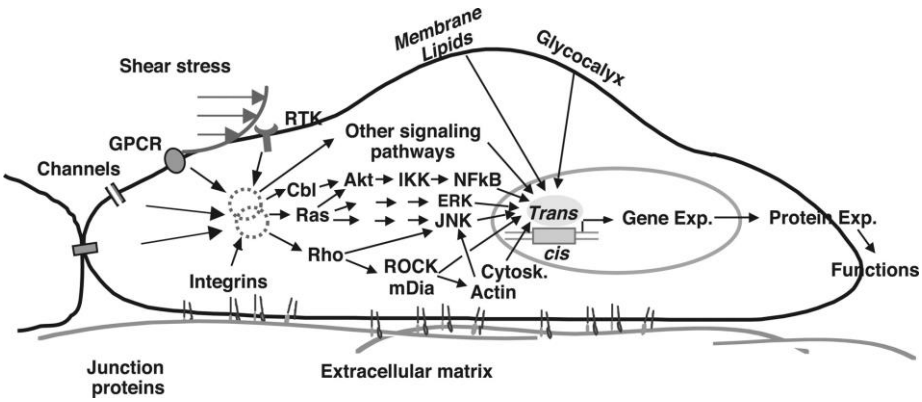

Figure 1.8. Schematic representation of mechanosensors and stress signaling pathways.[90]

However, mechanotransduction is not tuned equally in all vascular vessels. Endothelial cells along the whole arterial tree are highly heterogeneous at three different levels, structure, expression patterns and function.[104] Depending on their location, endothelial cells have different neighboring cells and applied mechanical forces have different profile and magnitude. Physiological hemodynamic conditions change at different locations in the vasculature. Alterations of such conditions have significant implications in disease progression. Endothelial cells in systemic vasculature, for instance, are typically exposed to laminar pulsatile flow with average shear stress between 5 and 25 dyn/cm^2.[105] Arterial geometries such as obstructed vessels or bifurcations result in the presence of higher shear stress and/or oscillatory flow profiles. In these scenarios, endothelial cells show higher inflammatory, atherogenic and thrombotic responses.[106–108]

In brain microvasculature, physiological hemodynamic conditions are complicated to measure due to capillary size. Yet, there is common agreement that flow through brain capillaries is steady and physiological shear stress levels are between 5 and 20 dyn/cm^2.[109,110] Brain microvascular endothelial cells respond to such dynamic patterns by enhancing BBB phenotype.[111] Exposure of physiological shear in brain microvascular endothelial cells upregulates tight junctions, drug transporters and ion channel genes, among others.[71] Shear stress has also proved to be a protective factor against inflammatory cytokines at the BBB.[112,113] While loss of shear stress in scenarios of ischemia leads to BBB failure[114,115], less is known about the effect of increased shear stress and pulsatility in microvascular endothelial cells at the neurovascular unit.

1.2.3. Hypertension and arterial stiffness

Normal hemodynamic parameters are estimated in predetermined ranges. In healthy adults, arterial blood pressure should be below 120/80 mmHg (systolic/diastolic). Hypertension is defined as a medical condition in patients with permanently higher blood pressure, with greater risk when systolic or diastolic pressures are beyond 140 and 90 mmHg, respectively. There are two types of hypertensive patients based on etiology. Primary or essential hypertension is the most common case of hypertension (90 – 95%). The origin of primary hypertension is unclear but associated to the effect of genetic, environmental and lifestyle factors. In secondary hypertension, which accounts for 5 – 10% of hypertensive patients, high blood pressure is caused by renal and endocrine disorders, or by the consumption of exogenous substances such as contraceptives or glucocorticoids. [116] Prevalence of primary hypertension is affected by

increasing age, ethnic origin and sex. Salt intake, overweight, alcohol consumption, lack of exercise or stress are typical risk factors that increase the probability of high blood pressure. Hypertension itself is a risk factor in the development of several disease conditions affecting different organs and tissues, including stroke, vascular dementia, coronary heart disease, heart failure, large vessel arterial disease, renal disease and retinopathy.[117]

Among the above-mentioned risk factors, increased blood pressure with age has also been associated for decades to arterial stiffness, an independent and progressive phenomenon developed in arterial vessels.[118] The arterial system is not only in charge of irrigating organs and tissues in the body, but also acts as a cushion. Arteries reduce pulsations generated by the left ventricle and allow blood to reach peripheral vascular beds with steady pressure and flow.[119] In young healthy adults, elastic arteries dilate and absorb energy from blood pressure. The resulting double peak pulse waveform results from the addition of the incident wave and reflected waves from points of wall resistance alterations or arterial bifurcations.[120] Transmitted wave reduces its amplitude as blood flows through sequential bifurcations. During the aging process, arteries dilate and stiffen because of fatigue deterioration of elastin fibers and continuous recruitment of collagen fibers, stiffer than elastin (Figure 1.9).[121] As a consequence of progressive stiffening, cushion capacity decreases, incident and reflected wave peaks align and generate higher pressure waves (Figure 1.10).

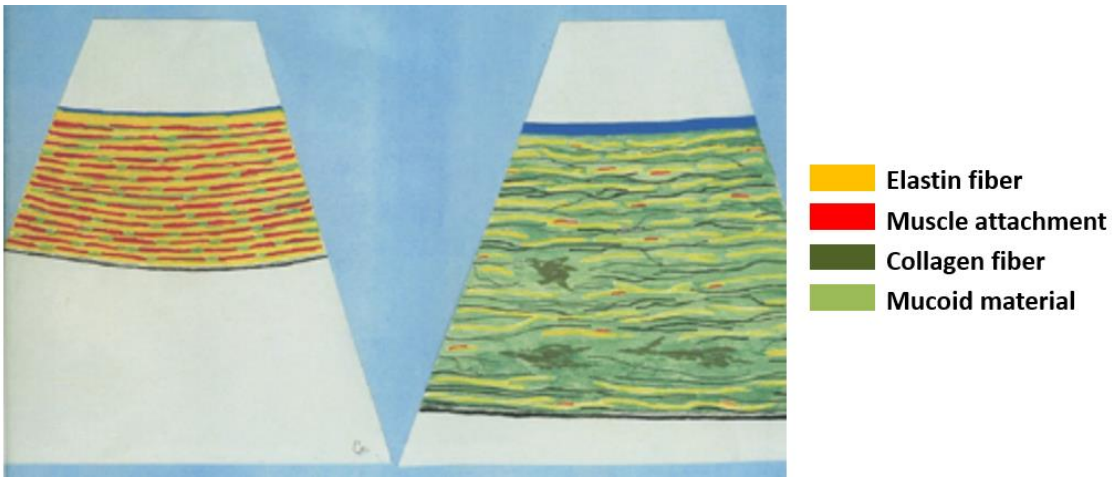

Figure 1.9. Schematic diagram of an aorta section in young (left) and old (right) humans, showing fracture of elastin and muscle fibers and increase of collagen and mucoid.[120]

Resulting high pressure waves from arterial stiffening move along the arterial tree with higher pulse wave velocity. While pressure and flow waveforms differ in shape, augmentation indexes measured in both show a linear correlation (Figure 1.11), which implies that blood flow is indirectly affected by the stiffening process.[122]

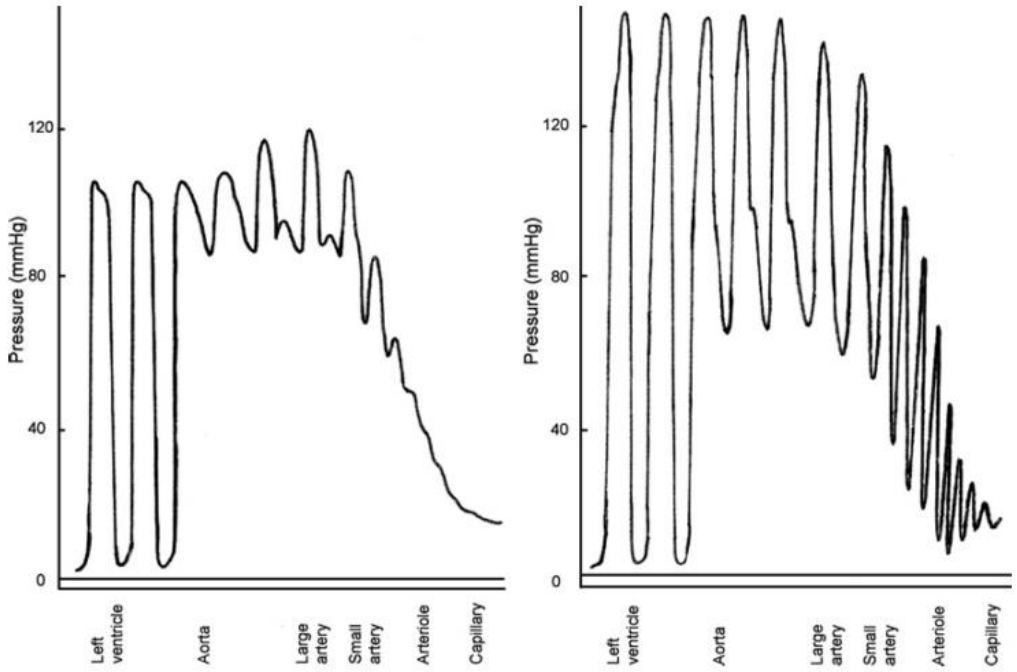

Figure 1.10. Pulsatile pressure changes in the vascular tree in young (left) and old (right) humans. Arterial stiffness extends pulsatility to microcirculation.[120]

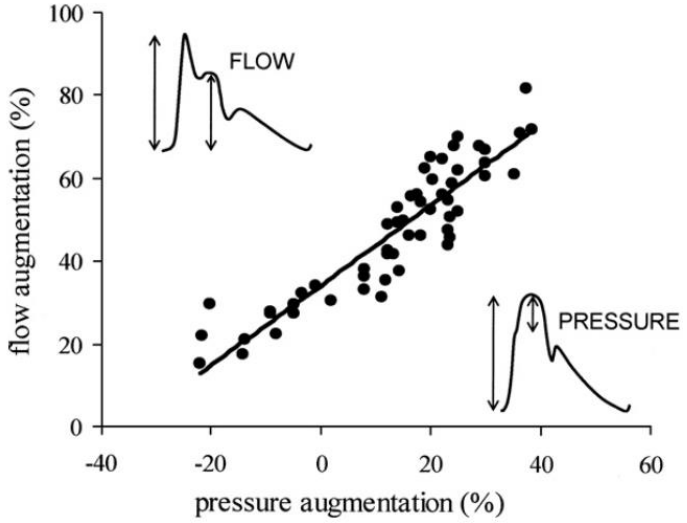

Figure 1.11. Linear relationship between augmentation of flow and pressure waves in the carotid artery.[120,122]

1.2.4. Vascular alterations in brain microcirculation

When physiological hemodynamic conditions are altered through phenomena such as hypertension or arterial stiffening, the subsequent deleterious implications in peripheral organs are significant. Microcirculation in vital organs with permanently dilated arteries, such as brain and kidney, can be exposed to higher pulsatile stresses than other organs.[123,124]

Vascular-related brain pathologies have been a concern due to the increased number of elder population. In 2015, the American Heart Association estimated the incidence of stroke to be 15 million worldwide.[125] Cerebrovascular disease is the fifth leading cause of death in the United States. In the case of non-fatal stroke, some subtypes may lead to increased probability of new vascular events.[126] Moreover, vascular dementia, the second most common form of dementia, is 4 times more likely in patients after stroke.[127] The statistics linking vascular impairment and cerebral disease are frightening, and motivated studies to show the relationship between flow alterations and cerebral diseases.

In the last decade, clinical studies have been conducted showing clear trends between hemodynamic parameters and stroke development. Raise in pulse wave velocity and pulse pressure significantly increase the risk of stroke.[128] More specifically, such conditions correlate with localized cerebral injuries such as white matter hyperintensities, lacunar infarcts and microbleeds in brain microcirculation.[129,130] Similarly, dementia-related diseases show a linear trend between symptoms of cognitive decline and hemodynamic markers. Again, longitudinal clinical studies revealed that increased pulse wave velocity and pulse pressure induce a decline in verbal learning, memory, cognitive screening, processing speed.[131–135] Under such circumstances, the risk of developing neurodegenerative diseases such as Alzheimer's disease increases.[136,137]

As described in Chapter 1.1.5, increasing evidence supports that endothelial state at the BBB is relevant in the development of different cerebral disease. As the interface between vascular and cerebral environments, interest grew in finding how vascular risk factors may be behind the underlying mechanisms that alter BBB phenotype in disease.[138,139] A clinical study showed that brain microcirculation is a direct intermediate link between arterial stiffness and cerebral damage.[140] In parallel, *in vivo* studies suggest BBB breakdown as the starting point in cerebral disease in hypertensive or stroke prone rodents.[141–143] Clinical or *in vivo* studies have deeply studied the already established concept of vascular-cerebral pathological link. However, *in vitro* studies have not yet focused on studying endothelial behavior and mechanistic response to parametrical hemodynamic alterations at the neurovascular unit.

1.2.5. Treatments for hypertension – Renal denervation as an emerging therapy

General guidelines for hypertension, established by different health organisms, have evolved during the last decades to provide standard protocols and steps to follow on the treatment of high blood pressure based on the existing knowledge. While the definition of blood pressure risks differs among different guidelines, they all share common principles and emphasize the achievement of a specific blood pressure target. Initial steps towards hypertension treatment include lifestyle interventions, such as weight reduction, diet modifications or reduction of alcohol/tobacco consumption. Prescription of antihypertensive drugs begins with the use of a single agent, whose type depends on the case. If blood pressure target is not achieved, the use of two or more combined drugs is encouraged.[144–146] Antihypertensive drug types listed in Table 1.1 reduce blood pressure through different methods of action.

Table 1.1. Commonly prescribed antihypertensive drugs and methods of action.

Drug type	Method of action
Diuretics	Reduce sodium and water excess from blood.
Beta-blockers	Reduce heart rate and cardiac output.
Angiotensin converting enzyme (ACE) inhibitors	Inhibit the expression of angiotensin, inducing blood vessel relaxation.
Angiontensin receptor blockers	Block the action of angiotensin, inducing blood vessel relaxation.
Calcium channel blockers	Inhibit calcium access across smooth muscle cells in heart and vessels, inducing vasodilation and heart rate reduction.

Despite the existence of different types of antihypertensive agents, pharmacological treatment does not always allows reaching the target blood pressure levels. Resistant hypertension is defined in hypertensive patients who do not reach target blood pressure after prescription of three or more antihypertensive drugs at the maximal tolerated doses or reach their target blood pressure after prescription of four or more drugs.[147] The prevalence of resistant hypertension is estimated to be 10 – 15 % among hypertensive population.[147,148] Given the major effects of hypertension in the development of vascular-related diseases and the fact that prevalence of resistant hypertension has increased over the last decades, device-based therapies for hypertension have recently emerged. Among them, renal denervation (RDN) therapy is the most revolutionary and promising therapeutic option.

The basis of RDN derives from recent findings suggesting that hypertension has a neurogenic component. Hypertension is initiated and sustained by sympathetic nervous system overactivity.[149] Sympathetic outflow to the kidney is increased in hypertensive patients, which is evidenced by an increased release of renal norepinephrine, a neurotransmitter that raises blood pressure.[150,151] Surgical ablation of renal nerves in experimental models confirmed previous observations and showed a decrease in blood pressure.[152] RDN therapy targets the sympathetic nervous system, which is ablated by delivering radiofrequency or ultrasonic energy into the lumen of both renal

arteries (Figure 1.12). While still not commercially available, several biomedical companies are currently developing RDN devices and performing clinical trials to assess their safety and efficacy (

Table 1.2).[153,154]

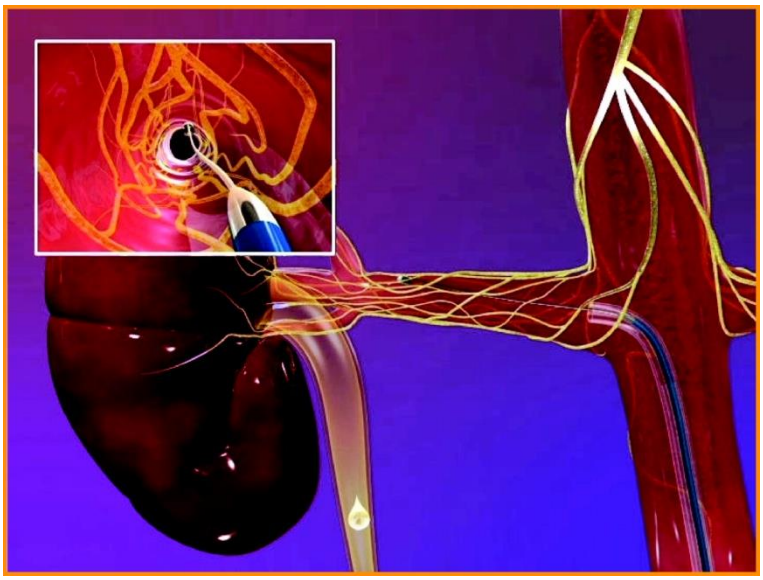

Figure 1.12. Graphic of catheter-based renal denervation procedure in distal renal artery.[155]

Table 1.2. List of renal denervation systems.[153]

Company	Device	Technology
Medtronic Inc. (Mountain View, CA, USA)	Symplicity	Radiofrequency
St. Jude Medical Inc. (St. Paul, MN, USA)	EnligHTN	Radiofrequency
Vessix Vascular Inc. (Laguna Hills, CA, USA) & Boston Scientific, Inc. (Minneapolis, MN, USA)	V2	Radiofrequency
Covidien (Dublin, Ireland)	OneShot	Radiofrequency
Biosense Webster Inc. (Diamond Bar, CA, USA)	Celsius ThermoCool	Radiofrequency
Boston Scientific Inc. (Minneapolis, MN, USA)	Chilli II	Radiofrequency
Renal Dynamics (Oviedo, FL, USA)	ReDy	Radiofrequency
ReCor Medical Inc. (Ronkonkoma, NY, USA)	PARADISE	Ultrasound
Cardiosonic Ltd. (Tel Aviv, Israel)	TIVUS	Ultrasound

Significant short-term blood pressure reductions were achieved in the Symplicity HTN-1[156] and Symplicity HTN-2[157] randomized clinical trials, which recently reported a sustained effect at longer time points.[158,159] However, in the latest Symplicity HTN-3[160] controlled trial, RDN procedures did not achieve the expected efficacy and caused some concerns about this technology. Recent evidence suggests that variability in the response of patients to RDN may be caused by non-homogeneous arterial microanatomy surrounding renal arteries, including not

only nerves but neighboring veins and lymph nodes.[161,162] Current treatments deliver the ablation energy in focal points instead of the whole lumen surface, and might miss regions where higher nerve densities are located. Computational modeling predicts ablation patterns and show that the presence of substructures with different thermal conductivity can alter energy distribution.[163]

In a recent study, RDN efficacy was tested in brain-related pathological aspects using spontaneous hypertensive stroke prone rats (SHRSP). Results showed significant prevention of neurological deficit, cerebral blood flow correction, glial activation and, most importantly, inhibition of BBB disruption.[164] Better understanding of the microanatomical environment of renal arteries is crucial to optimize renal denervation therapy to reduce hypertension, improve proper vascular activity and recover physiological conditions at the BBB.

1.3. Hypothesis and objectives

The phenotype of endothelial cells along blood vessels is highly affected by hemodynamic parameters. When physiological conditions are altered, mechanisms are triggered inducing cellular damage with potential implications in the development of disease. Specific understanding of the effect of blood flow in microvascular endothelium at the Blood-Brain Barrier is missing.

In the present thesis, it is hypothesized that brain microvascular endothelial cell state is affected by flow. Such cellular state plays a fundamental role in the performance of the BBB. Human brain microvascular cell (HBMEC) phenotype may be stimulated or silenced depending on the biomechanical conditions to which cells are exposed. In such scenario, hemodynamic repair might be a potential therapeutic target to optimize BBB phenotype.

To address these hypotheses, the following objectives are defined:

1) Analyze the effect of shear stress and pulsatile flow on the expression, functional and structural phenotype of brain microvascular endothelial cells.
2) Evaluate Blood-Brain Barrier breakdown in animal models with different vascular conditions.
3) Design and characterize a customizable *in vitro* Blood-Brain Barrier model allowing co-culture of brain microvascular endothelial cells with astrocytes and flow exposure.
4) Provide new insights for optimization of renal denervation therapies by detection of patterns in renal artery microanatomy and correlation with ablation efficacy.

2. Pulsatility and high shear stress deteriorate barrier phenotype in brain microvascular endothelium

2.1. Introduction

The following chapter focuses on the effect of flow and shear stress on human brain microvascular endothelium. Human brain microvascular endothelial cells (HBMEC) were cultured in tubular constructs, which have been previously used on endothelial cells, have a simple handling and tolerate high flow rates.[108,165,166] Cell culture medium was fed into the system by using a flow perfusion bioreactor, which is described in detail in Chapter 5.4.

Prior to the dynamic study of cerebral microvascular endothelium, it was necessary to establish the optimum experimental parameters to maximize BBB phenotype development. Chapter 2.2 optimizes temporal development of BBB markers in static cultures. Then, Chapter 2.3 establishes optimal dynamic conditions for subsequent experiments. Results on the effects of shear stress patterns in dynamic HBMEC cultures are shown from Chapter 2.4.1 to 2.4.6, including a study of cellular behavior upon shear stress reversibility. Key BBB markers were analyzed, Claudin 5 and Zonula Occludens 1 (ZO-1) as tight junction proteins, P-glycoprotein (P-gp) as a representative marker of ATP-binding cassette (ABC) efflux transporters and Glucose Transporter 1 (GLUT1) as a representative marker of solute-like carrier (SLC) transporters. Mechanistic insights linking proteomic alterations with flow are provided in Chapter 2.4.7. Finally, results found in *in vitro* experiments were evaluated *in vivo* in Chapter 2.5 using hypertensive rats.

2.2. Temporal barrier formation in static HBMEC/HA co-cultures

HBMEC and HA were co-cultured in 6-well plate transwell inserts and grown for 1, 2, 4 and 7 days. Cells were then lysed and protein expression of Claudin 5, P-gp and GLUT1 was analyzed as representative tight junction, efflux transport and SLC transport markers, respectively. Figure 2.1 shows the evolution of those markers with time.

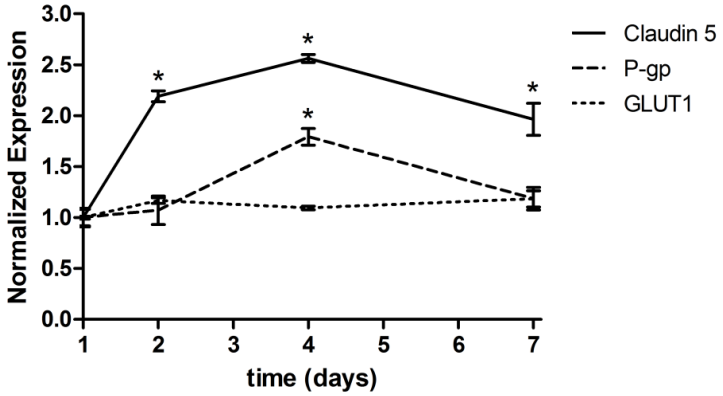

Figure 2.1. Expression of Claudin 5, P-gp and GLUT1 in static HBMEC/HA co-cultures during 7 days.

The expression of Claudin 5 and P-gp increased significantly until day 4 (2.56±0.04-fold and 1.79±0.08-fold, respectively), compared to day 1. Such increase was followed by a significant expression reduction at day 7. In the case of GLUT1, the expression remained constant during the whole experiment. Loss of Claudin 5 and P-gp levels may be associated with the rapid loss of phenotype that characterizes HBMEC in *in vitro* cultures.[57,167] After the expression analysis, four days was chosen as the optimal time-point in order to maximize BBB phenotype.

HBMEC morphology in Figure 2.2 showed confluent monolayers and positive localization of tight junction markers ZO-1 and Claudin 5.

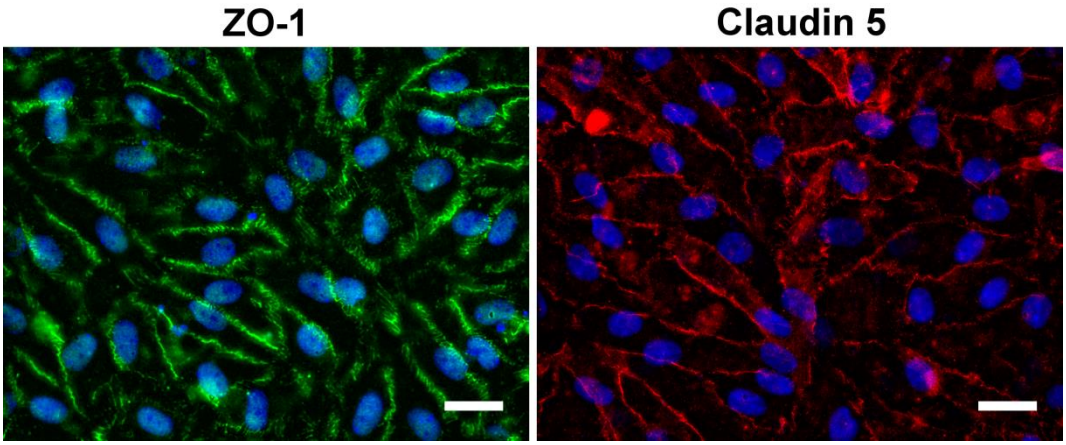

Figure 2.2. HBMEC confluent monolayer after 4 days of co-culture. (Green: ZO-1; Red: Claudin 5; Blue: nuclei; Scale bar = 2.5µm).

In order to confirm barrier formation, functional permeability assays were done in HBMEC/HA co-cultures in 24-well plate Transwell inserts using fluorescent-labeled dyes of different size (4, 20 and 70 kDa FITC-Dextran, with Stokes radius of 1.4, 2.4 and 3.6 nm, respectively). Permeability coefficients of 4, 20 and 70 kDa dextrans in HBMEC/HA cultures were 2.41±0.08, 1.10±0.11 and 0.05±0.03 x 10^{-6} cm/s, respectively (Figure 2.3).

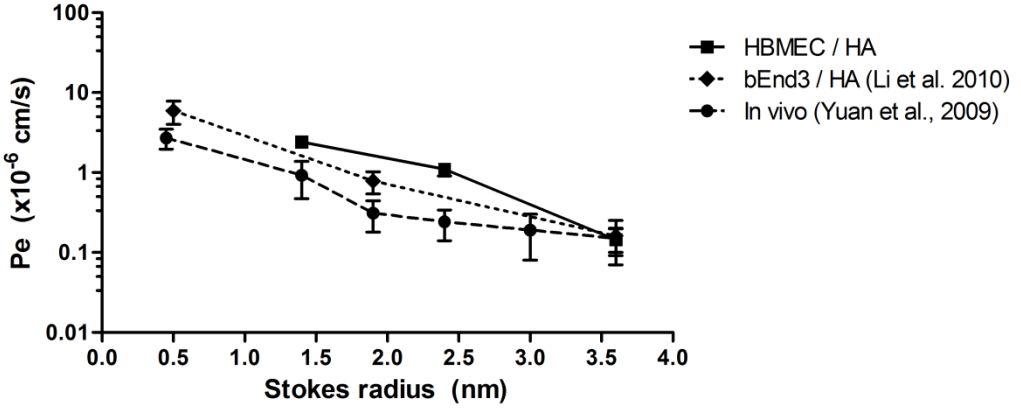

Figure 2.3. Permeability of HBMEC/HA co-culture and comparison with published *in vivo* and *in vitro* data.

As expected, the permeabilities obtained are higher than *in vivo* data[168], but have no significant difference with other published *in vitro* results.[169]

2.3. HBMEC dynamic culture optimization and experimental setup

Expression, localization and functional analysis of HBMEC/HA co-cultures were successful at 4 days of culture. Temporal evaluation of barrier formation was also performed on dynamic HBMEC cultures where cells were seeded on the luminal wall of silicone rubber tubing for flow exposure. However, additional concerns became apparent in this scenario. First, in order to enhance BBB phenotype, the culture medium used in HBMEC cultures is depleted from vascularization factors and FBS percentage is lower.[170] In the presence of flow-induced shear stress, cells might not resist and detach from tubes. Also, co-culture with astrocytes was not possible in tubes. As a consequence, astrocyte-conditioned medium (ACM), which is also known to induce barrier phenotype[1,24], was used as a substitute. Endothelial growth medium was used to condition astrocytes, so an evaluation of astrocyte viability and morphology on endothelial medium was required, followed by an evaluation of ACM effectiveness. All previous problems were addressed before a final evaluation of HBMEC viability under the final experimental conditions.

2.3.1. Temporal tight junction formation in dynamic cultures

HBMEC were cultured during 1, 4 and 7 days at 5 dyn/cm^2 using the flow perfusion bioreactor described in Chapter 5.4. Tight junction marker ZO-1 was positively immunostained, showing that HBMEC morphology progressively oriented and aligned with flow direction (Figure 2.4.A-C).

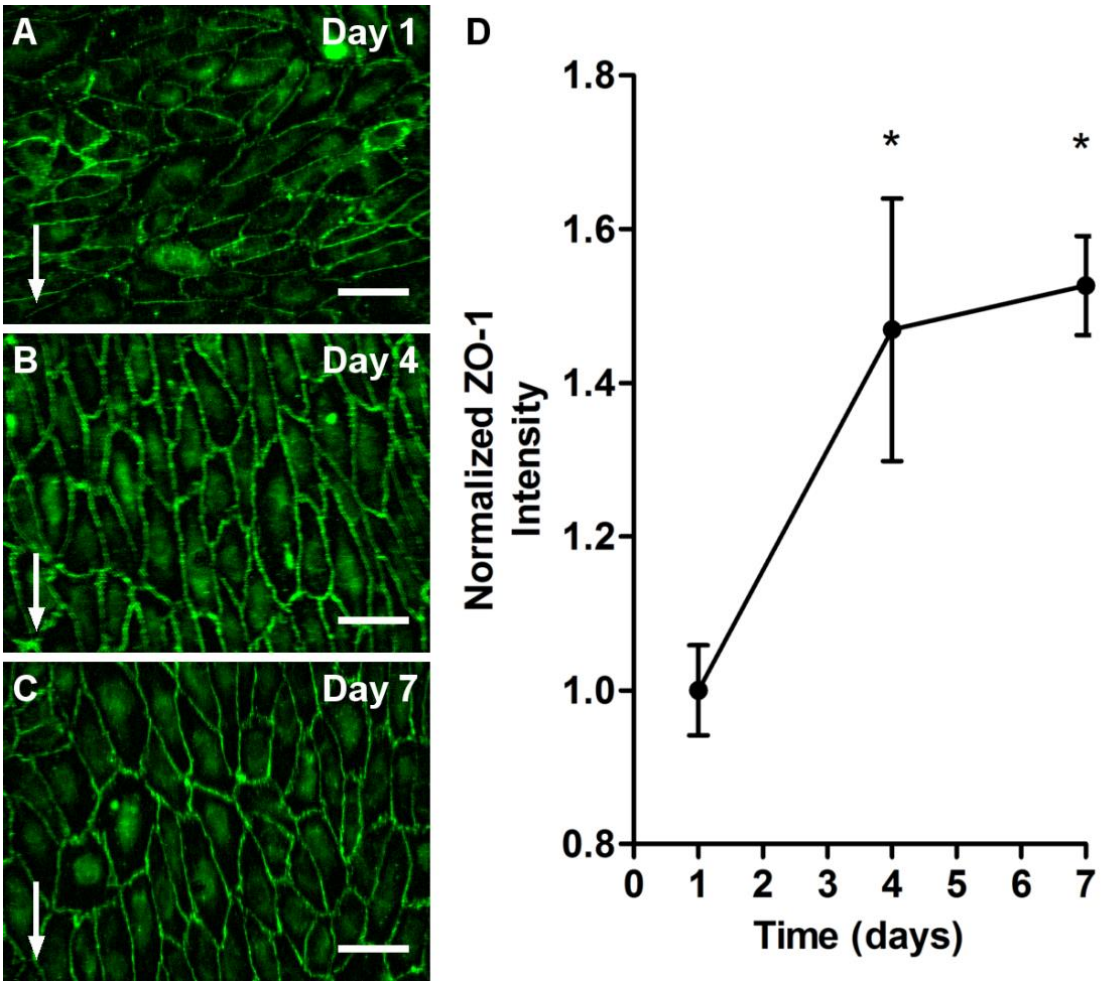

Figure 2.4. Evolution of HBMEC morphology and junctional localization of ZO-1 (A –C). Image intensity quantification (D) (Arrows: flow direction; Scale bar = 5 µm).

ZO-1 junctional intensity was quantified (Figure 2.4.D). At day 4, ZO-1 was significantly upregulated (1.47±0.17-fold) compared to day 1. Such increase was maintained at day 7 (1.53±0.06-fold), with no statistical significance between day 4 and 7. Results are in agreement with the static temporal study of BBB phenotype induction in Chapter 2.2. Further HBMEC dynamic cultures were performed for 4 days, prior to the execution of any analytical technique.

2.3.2. Resistance of HBMEC to depleted culture medium and shear stress

HBMEC were cultured in tubes of equal dimensions at 5 dyn/cm^2 with endothelial growth media depleted from vascularization factors and supplemented with 2.5 or 0% FBS. A static group of tubes with the same media and 2.5% FBS was used as a control. After 4 days, cells were trypsinized and counted. Figure 2.5 shows the number of cells in each group.

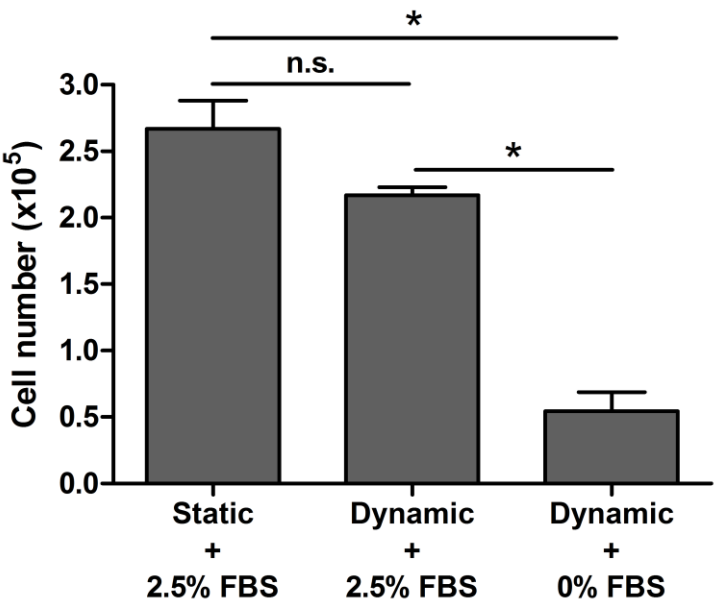

Figure 2.5. Effect of vascular growth factors and FBS depletion on dynamic HBMEC cultures.

Under dynamic conditions and 2.5% FBS, the cell count was 2.17±0.06·10^5 cells/tube, which was lower than the static control (2.67±0.21·10^5 cells/tube) but non-significantly. The combination of shear stress, removal of growth factors and decrease of FBS from the usually applied 5% to 2.5% did not affect cell attachment in the surface of tubes. Total removal of FBS, however, affected cell attachment when stimulating cells with shear stress. The cell count was 0.54±0.14·10^5 cells/tube and was significantly lower than both static and dynamic groups with 2.5% FBS. Vascular growth factors were not added in cell culture medium and FBS was limited to 2.5% in dynamic experiments with HBMEC.

2.3.3. Viability and morphology of HA in endothelial growth medium

ACM was collected by growing HA with endothelial growth medium (EGM-2) and incubating confluent plates with endothelial basal medium, as described in Chapter 5.3.6. Figure 2.6 shows a comparison of HA cell viability grown with EGM-2 and the manufacture-recommended and commonly used astrocyte medium (AM).

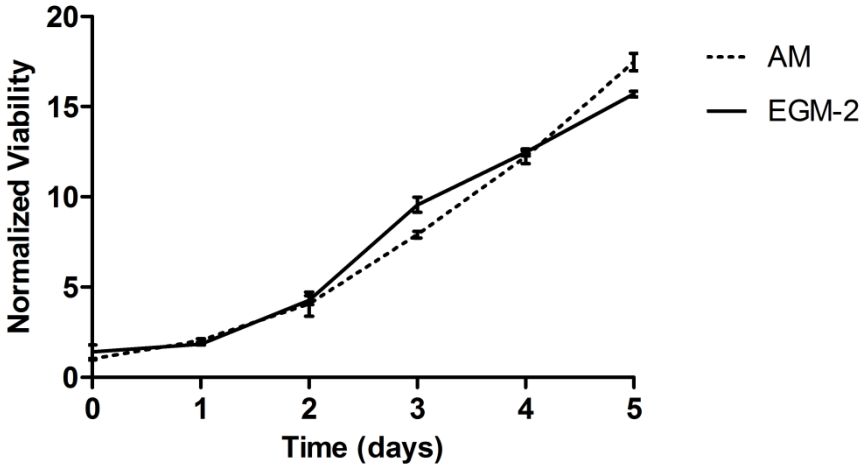

Figure 2.6. HA viability in cultures with AM and EGM-2.

The evolution of cell viability was equivalent in both cell culture media, with no statistical difference between them. EGM-2 did not alter HA growth.

Cell morphology was also compared by immunofluorescent imaging of GFAP, a specific functional astrocytic marker.[26] As seen in Figure 2.7, HA displayed in both cases the distinctive *in vitro* elongated morphology with the presence of astrocytic end-feet. No significant morphological differences were observed.

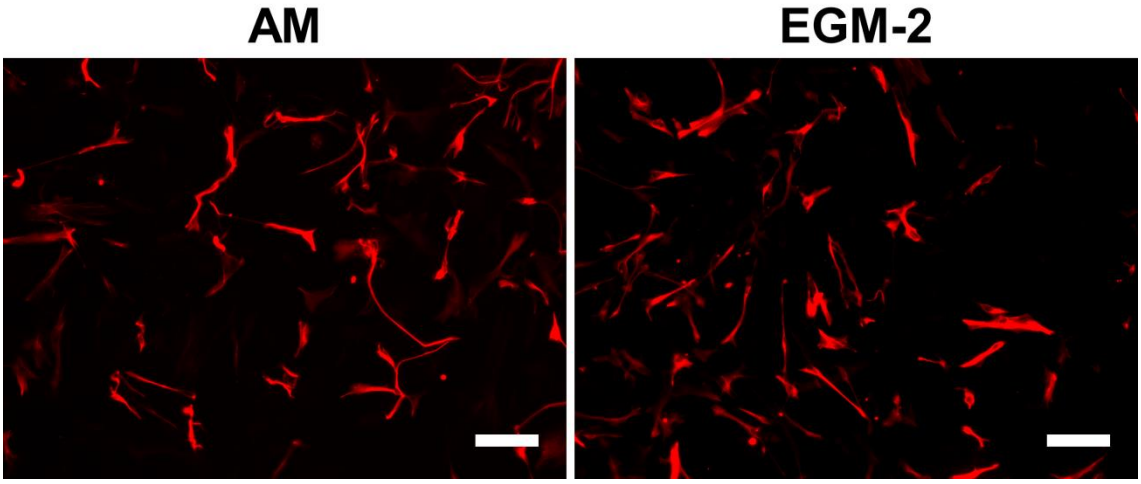

Figure 2.7. Astrocyte morphology and GFAP immunostaining of HA grown with AM and EGM-2 (Scale bar = 10 µm).

2.3.4. Effect of astrocyte-conditioned media on human brain and dermal microvascular endothelial cells

After confirmation that cells withstand flow with depletion of vascular growth factors and FBS, and that ACM collection does not compromise HA growth and morphological behavior, a new cell culture media was adapted. Endothelial dynamic culture medium (EDCM) was prepared as a mixture with a 1:1 ratio between ACM and EGM-2, the latter without growth factors and 5% FBS, so that the resulting media contained astrocyte secreted factors and 2.5% FBS.

EDCM was tested to evaluate ACM barrier phenotype induction. HBMEC were cultured for 4 days at 10 dyn/cm^2 using EDCM containing either 50% ACM and 50% endothelial basal medium as a control. Additionally, the same culture media were used in human dermal microvascular cells (HDMEC), as non-BBB microvascular endothelial cells control groups. Figure 2.8 shows cell morphology and junctional presence of ZO-1 after exposure of flow.

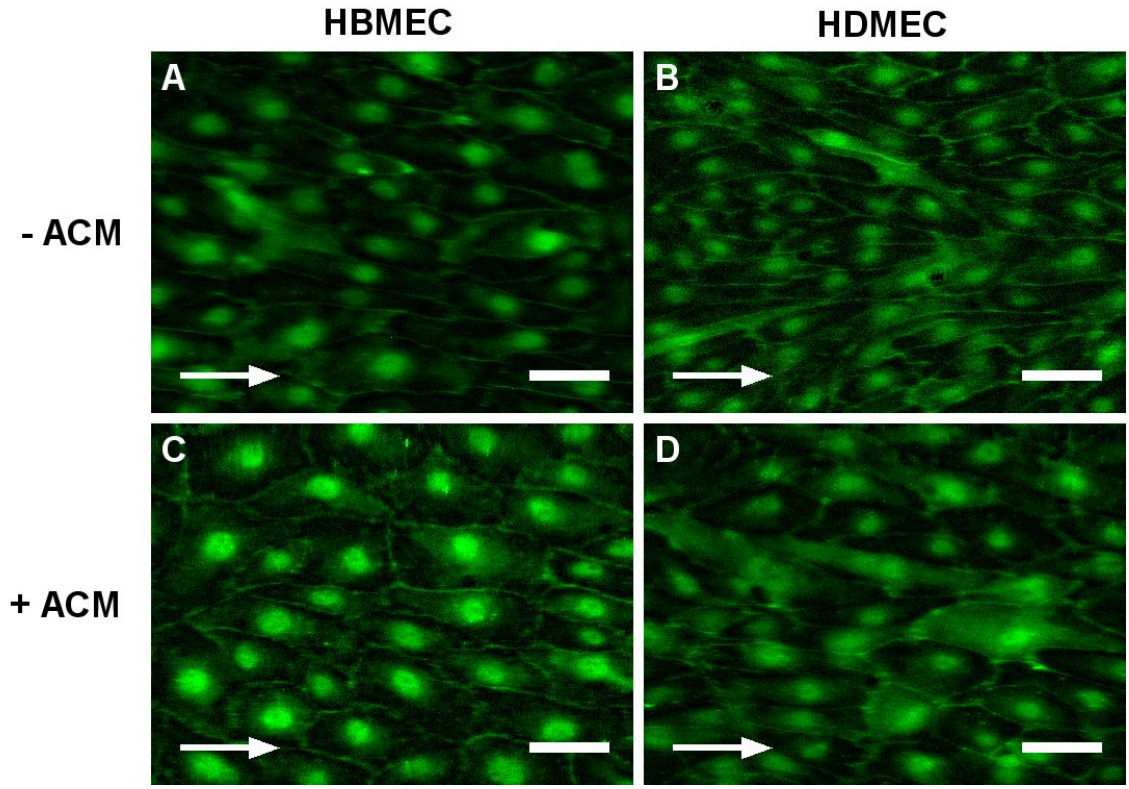

Figure 2.8. Morphology and junctional localization of ZO-1 in HBMEC (A, C) and HDMEC (B, D) dynamic cultures in the absence (A, B) or presence (C, D) of ACM (Arrows: flow direction; Scale bar = 5 µm).

Again, endothelial cells aligned with flow direction. ZO-1 was positively detected in tight junctions in all groups, with an apparent higher intensity in HBMEC cultured with ACM. Intensity of junctional ZO-1 was quantified to confirm visual indications (Figure 2.9).

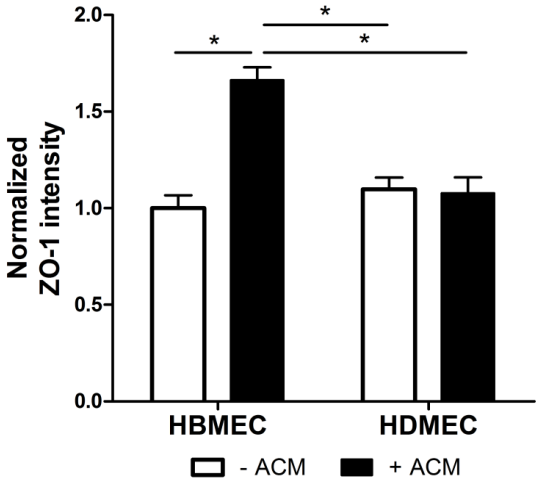

Figure 2.9. Junctional intensity of ZO-1 in human brain and derman microvascular endothelial cells in the presence or absence of astrocyte-conditioned medium.

In the absence of ACM, both HBMEC and HDMEC displayed equal amounts of ZO-1 in intercellular junctions, with no statistical difference between them. However, while ZO-1 presence remained at the same basal level in HDMEC with addition of ACM, HBMEC showed a significantly higher amount of ZO-1 at tight junctions (1.66±0.07-fold). Results from this experiment confirm that ACM is indeed a barrier phenotype inducer that, more interestingly, has selectivity on microvascular endothelial cells from the brain.

2.3.5. HBMEC viability in dynamic cultures with EDCM

Cell viability was measured in HBMEC cultured with EDCM in static conditions and at 10 dyn/cm^2. Figure 2.10 shows that viability increases slightly in both cases with no significant difference between the static and dynamic groups. HBMEC viability was not compromised in any case, which confirmed EDCM suitability for the duration of dynamic experiments.

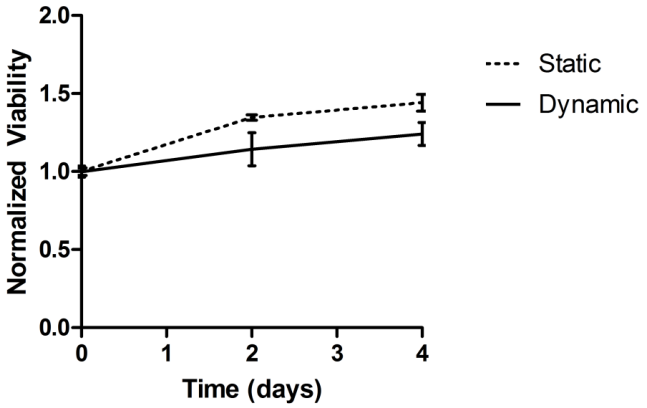

Figure 2.10. Cell viability of HBMEC in static and dynamic cultures in endothelial dynamic culture medium.

2.4. Effect of shear stress on the BBB

2.4.1. Shear stress extent selection

When blood circulation reaches the surface of the brain through incoming arteries from the circle of Willis, blood penetrates into the brain parenchyma.[171] After consecutive bifurcations, vessels become arteriole, pre-capillaries and, finally, capillaries. Capillaries have the smallest size in human vasculature, with an estimated diameter of 7 µm.[110] Because of its microscopic size and location, shear stress in brain capillaries is extremely difficult to measure with non-invasive techniques. However, literature on shear stress brain capillaries is wide and estimates normal physiological range between 5 and 20 dyn/cm^2.[71,109,110] In future experiments, 10 and 20 dyn/cm^2 were selected as physiological shears.

In patients with vascular conditions such as hypertension, shear stress may increase. Using a previously implemented computational platform[172], a three-dimensional arteriolar ramification network was designed (Figure 2.11.A) using vessel diameters and lengths measured from human neuroangiographies. Ramification type was limited to bifurcation only, as it is the most common kind in the brain microvasculature.[110] CFD simulations were performed, where pressure gradients generated along the whole structure (Figure 2.11.A) induced shear stress increase from the inlet of the model to the pre-capillary outlets (Figure 2.11.B-C).

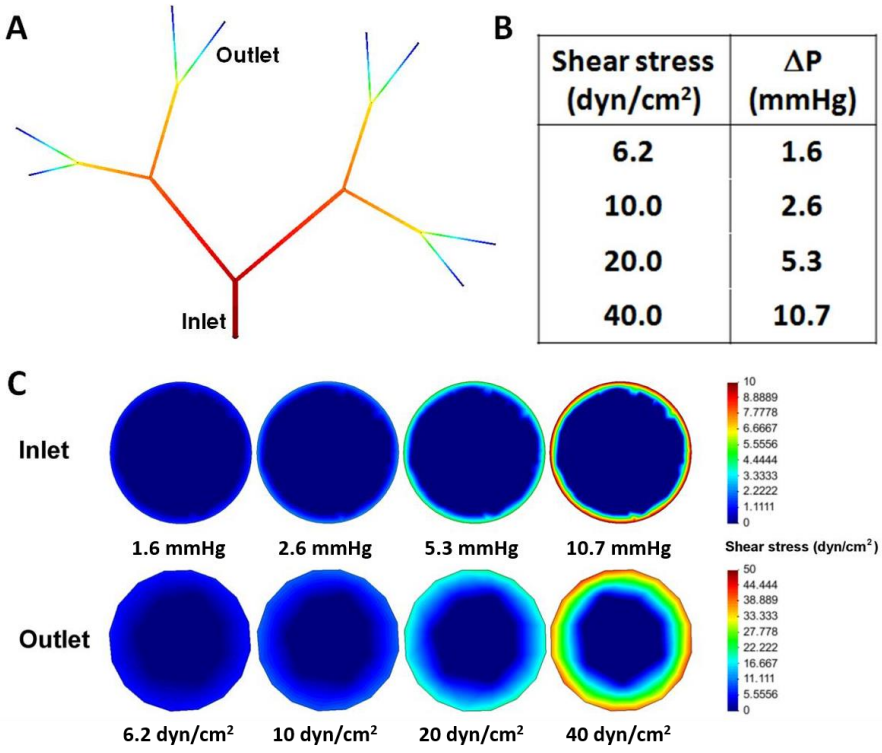

Figure 2.11. Computational fluid dynamics simulations of an arteriolar fractal tree model where pressure gradient in the geometry (A) induced a shear stress increase (B) from the inlet to the outlet pre-capillaries up to 40 dyn/cm^2.

Outlet shear stress was measured at different pressure gradient levels in the model. Results in Figure 2.11.C show that, in a simple model with three levels of bifurcation, a pressure gradient increase from 5.3 to 10.7 mmHg can raise the outlet shear stress from 20 to 40 dyn/cm^2. Carotid pulse pressure in hypertensive patients is at least 10 mmHg higher than normotensive patients[173], which may lead to higher pressure gradients leading to shear stress of 40 dyn/cm^2 or higher entering the BBB region. An additional study group of 40 dyn/cm^2 was included in the following experiments as a scenario of high pathological shear stress.

HBMEC were exposed to the afore-mentioned shear stresses at both steady and pulsatile flow patterns, in order to simulate healthy hemodynamic circulation and altered high pulses potentially induced by hypertension and arterial stiffness.

2.4.2. Pulsatility and high shear stress downregulate the expression of critical tight junction markers

HBMEC were cultured under static conditions (0 dyn/cm^2) as a control, and up to six different flow conditions (10, 20 and 40 dyn/cm^2 in steady and pulsatile flow patterns). After exposing HBMEC to laminar steady flow for 4 days, Western blot results support literature and confirm that, under physiological shear stress, expression of tight junction markers is upregulated (Figure 2.12.A).

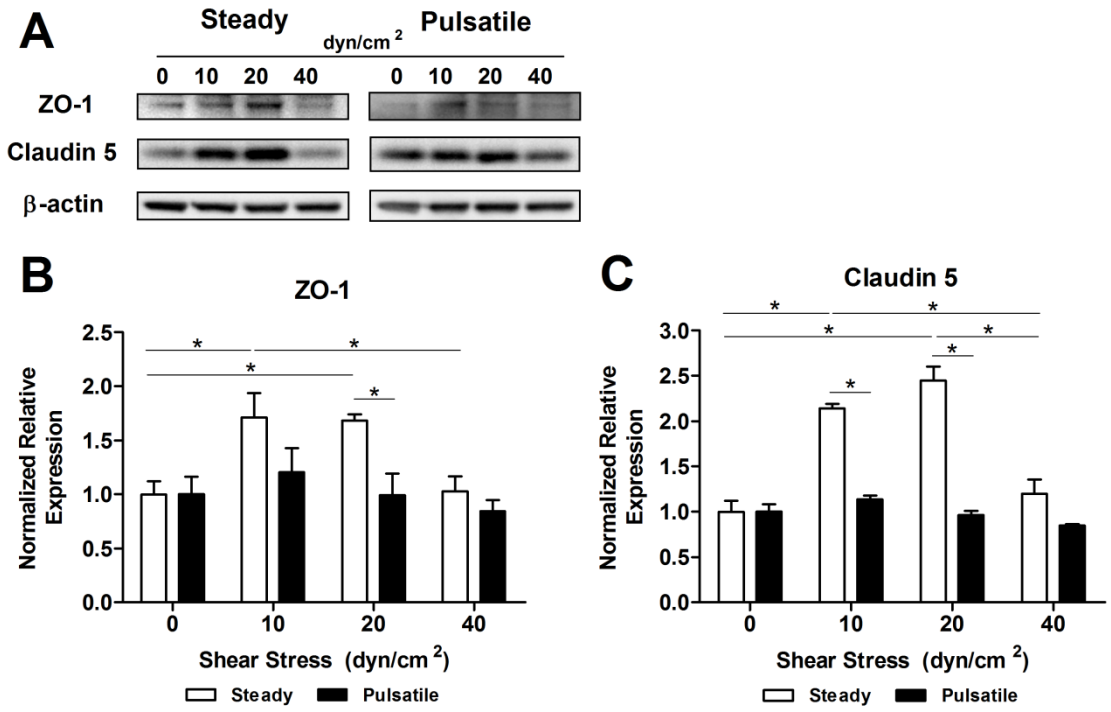

Figure 2.12. Effect of shear stress on the expression of tight junction markers ZO-1 and Claudin 5.

Densitometric quantification showed that the expression of ZO-1 (Figure 2.12.B) increased significantly in steady flow at 10 dyn/cm^2 (1.71±0.23-fold) and 20 dyn/cm^2 (1.68±0.06-fold). Interestingly, ZO-1 dropped, and was not different from the static control, at 40dyn/cm^2 (1.03±0.14-fold). Claudin-5 expression (Figure 2.12.C) showed a similar trend, with significant increase at 10 and 20 dyn/cm^2 (2.14±0.05-fold and 2.45±0.15-fold, respectively). Again, 40 dyn/cm^2 steady flow (1.20±0.15-fold) brought Claudin-5 expression down to static basal expression. When cells were exposed to pulsatile flow, the expression of both junctional markers showed no significant difference as compared with the static control under any shear stress studied. It is important to remark that cells exposed to pulsatile flow patterns within the range of physiological shear stress levels revealed a significant downregulation of ZO-1 and Claudin-5 when compared to steady patterns with the same average shear stress of 10 (1.42±0.32-fold

and 1.88±0.09-fold, respectively) and 20 dyn/cm^2 (1.69±0.34-fold and 2.54±0.20-fold, respectively).

In both steady and pulsatile flow patterns, the expression level of both ZO-1 and Claudin-5 at different shear stress showed linear correlation, of R^2=0.97 according to Pearson's correlation (Figure 2.13).

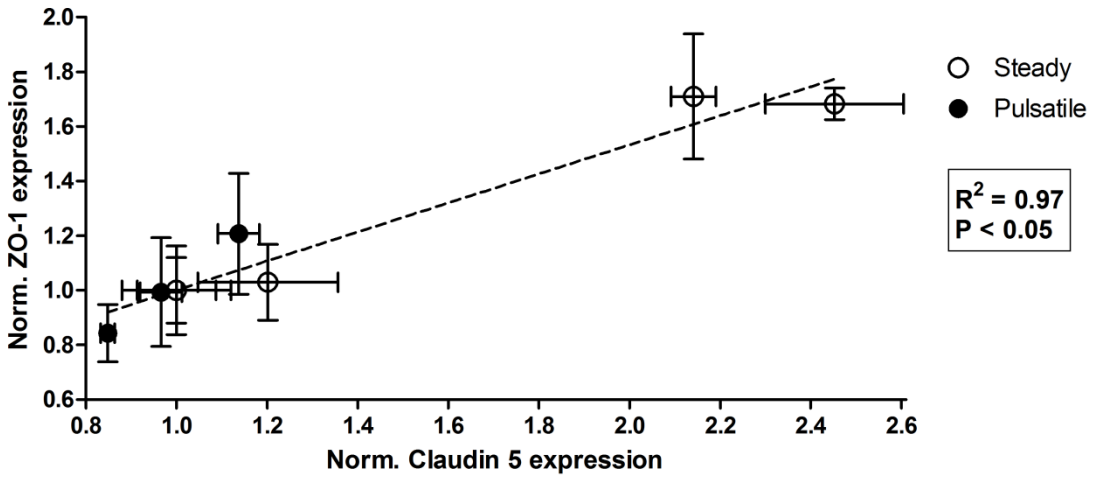

Figure 2.13. Shear-independent linear correlation between the expression levels of ZO-1 and Claudin 5.

Regardless of individual expression variations, our results suggest that the whole junctional structure formed by transmembrane domains (Claudin-5) and cytosolic anchorage (ZO-1) is affected concurrently. Flow regulation of ZO-1 and Claudin-5 are intrinsically connected independently of flow type or shear.

2.4.3. High shear stress disrupts tight junction morphology

HBMEC were exposed to steady and pulsatile shear stress for 4 days and stained with specific antibodies against ZO-1 in order to accurately study cell and junctional morphology under different scenarios (Figure 2.14). Junctional and nuclear/cytosolic ZO-1 intensity was quantified and represented in Figure 2.15 and Figure 2.16, respectively.

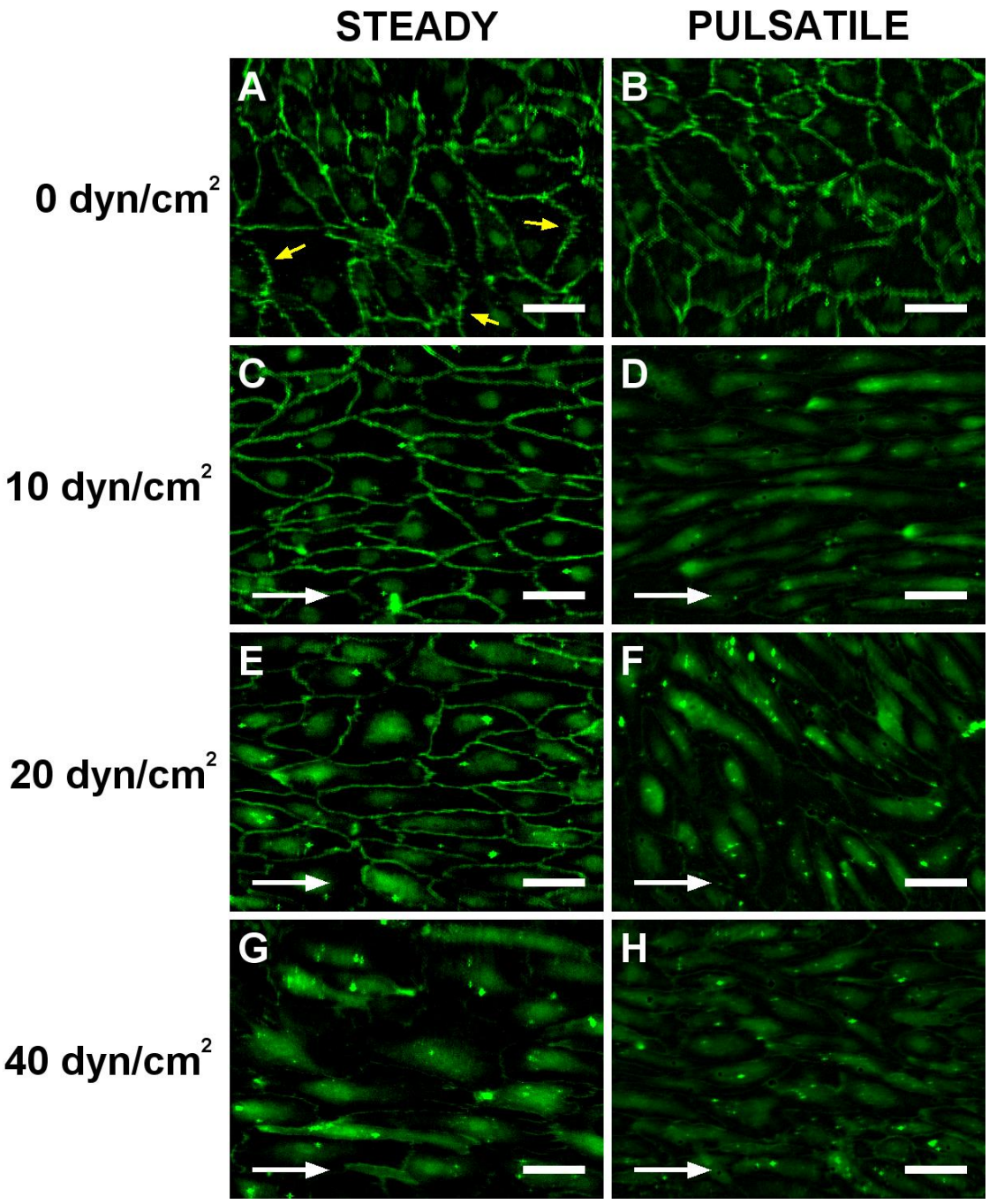

Figure 2.14. HBMEC morphology after exposure of 0 (A, B), 10 (C, D), 20 (E, F) and 40 (G, H) dyn/cm^2 at steady (A, C, E, G) and pulsatile flow patterns (B, D, F, H) (White arrows: Flow direction; Yellow arrows: junctional saw-tooth patterns; Scale bar = 5 µm).

The static controls (Figure 2.14.A and B) showed a disorganized junctional morphology (yellow arrows). Tight junctions in static controls displayed discontinuous saw-tooth patterns. Such serrated patterns differed greatly from those observed in cells cultured under physiological steady shear stress (10-20 dyn/cm^2, Figure 2.14.C and E), which had linear junctions aligned with flow. ZO-1 was especially intense and localized in the intercellular junctions of cells exposed to 10 and 20 dyn/cm^2.

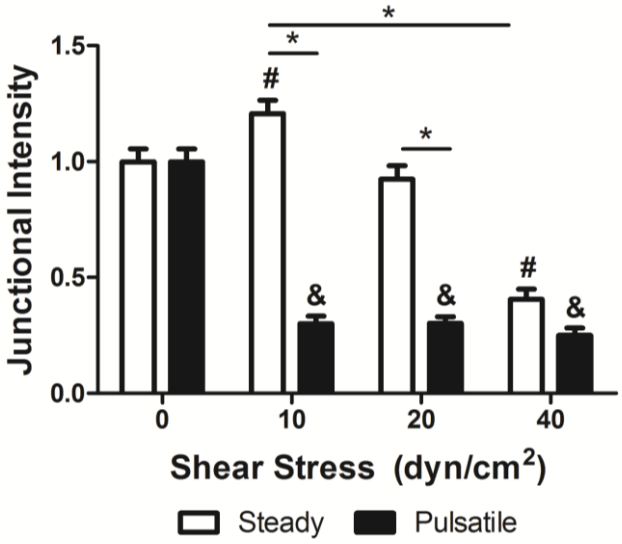

Figure 2.15. Effect of shear stress on ZO-1 junctional intensity (* P<0.05 between selected bars; #,& P<0.05 between steady (#) or pulsatile (&) shear stress compared to static control).

Junctional ZO-1 intensity measured by immunofluorescence (Figure 2.15) was indeed significantly higher (1.21±0.06-fold) than in the static control. Contrarily, ZO-1 was translocated to the cytoplasm in cells exposed to abnormally high shear stress (40 dyn/cm^2,Figure 2.14.D). ZO-1 junctional intensity decreased dramatically (0.41±0.04-fold) in these cells. These results showed similar trends to those previously analyzed by Western blot (Figure 2.12.B) and confirmed that abnormally high shear stress compromised barrier phenotype.

Pulsatile flow (Figure 2.14.B, D, F and H) caused ZO-1 delocalization independently of the applied shear stress. The fluorescence intensity of ZO-1 was significantly lower (0.30±0.03-fold) than the static. In cells exposed to 10 dyn/cm^2, ZO-1 junctional expression was 3.9±0.4-fold lower when flow was pulsatile than when cells were exposed to steady flow. Similarly, there was a 3.1±0.4-fold difference between cells exposed to pulsatile flow versus cells exposed to steady flow at 20 dyn/cm^2. There was, however, no significant difference between cells exposed to pulsatile or steady 40 dyn/cm^2 flow as ZO-1 was already low and translocated into the cytoplasm. Interestingly, the differences between steady and pulsatile shear stress at 10 and 20 dyn/cm^2 were significantly higher in junctional ZO-1 (Figure 2.15) than in total ZO-1 expression (Figure

2.12.B), suggesting that pulsatility triggers ZO-1 delocalization. Cytoplasmic/nuclear ZO-1 intensity was quantified (Figure 2.16), showing significantly higher non-junctional ZO-1 for all pulsatile shear stresses (2.32±0.12-fold at 10 dyn/cm^2, 2.03±0.11-fold at 20 dyn/cm^2 and 1.44±0.11-fold at 40 dyn/cm^2).

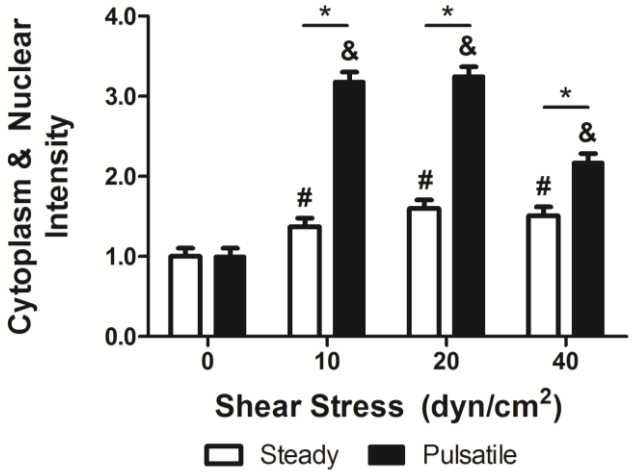

Figure 2.16. Effect of shear stress on ZO-1 cytoplasmic and nuclear intensity (* P<0.05 between selected bars; #,& P<0.05 between steady (#) or pulsatile (&) shear stress compared to static control).

The ratio between junctional and cytoplasmic/nuclear ZO-1 was measured (Figure 2.17) for every shear stress, under steady or pulsatile flow. Under increasing steady shear stress, ZO-1 localization shifted gradually from junctional to internal, as the ratio decayed significantly (0.58±0.05 and 0.27±0.03 at 20 and 40 dyn/cm^2, respectively). This ratio was significantly lower for all pulsatile shear stresses (0.10±0.01 at 10 dyn/cm^2, 0.09±0.01 at 20 dyn/cm^2 and 0.13±0.01 at 40 dyn/cm^2).

In conclusion, pulsatile flow jeopardized microvascular junction independently of shear stress.

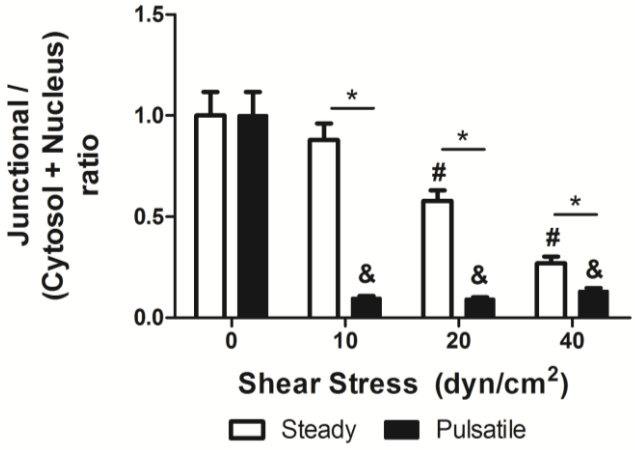

Figure 2.17. Ratio between junctional and cytosol/nuclear ZO-1 (* P<0.05 between selected bars; #,& P<0.05 between steady (#) or pulsatile (&) shear stress compared to static control).

2.4.4. Shear stress and pulsatility induce different expression profiles in transporters P-gp and GLUT1

Western blotting of transport markers P-gp and GLUT1 was performed on cell lysates from HBMEC exposed to different shear stress values (Figure 2.18.A). The expression of P-gp (Figure 2.18.B) was significantly increased between 1.5- and 1.6-fold in cells exposed to steady flow, independently of mean shear stress applied. No significant differences in expression of transporters were found between shear stress of 10, 20 and 40 dyn/cm^2. The expression of P-gp in pulsatile cultures was in all cases lower than the steady analog, with a significant difference at 20 and 40 dyn/cm^2.

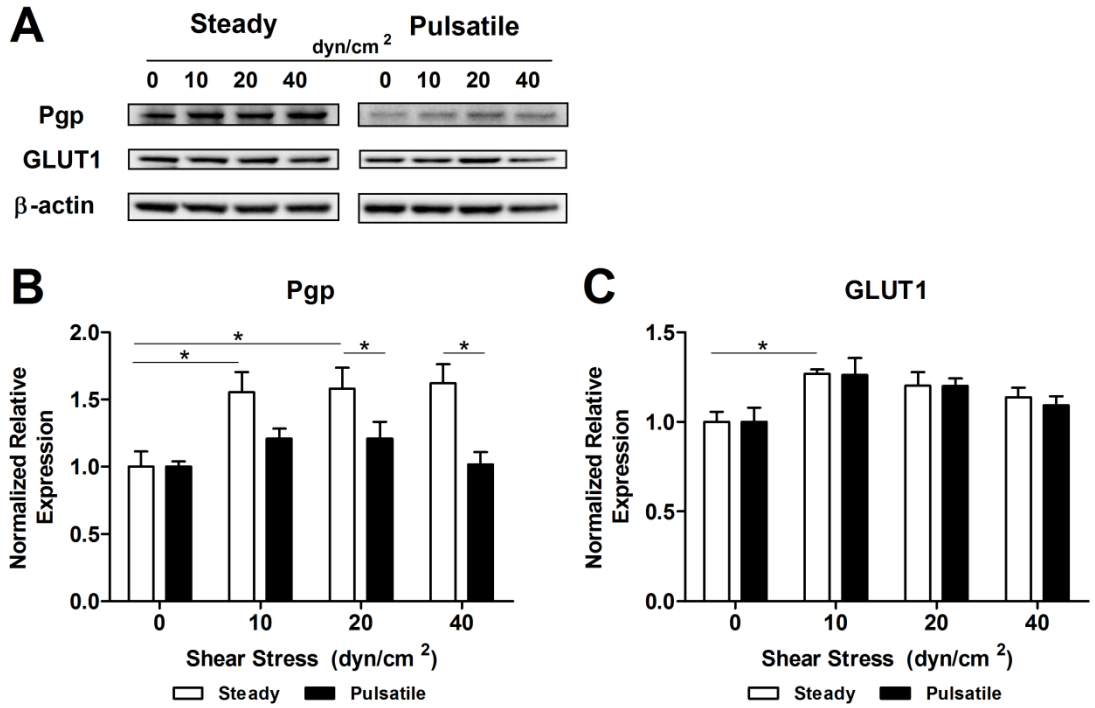

Figure 2.18. Effect of shear stress on the expression of P-gp and GLUT1.

Thus, P-gp expression may be compromised when both pathological shear stress and pulsatile flow are present. Contrary to P-gp, the expression of GLUT-1 (Figure 2.18.C) showed no significant difference between steady and pulsatile flow. Both flow patterns showed the same tendency, where GLUT1 expression peaked significantly in cells exposed to steady 10 dyn/cm^2 (1.27±0.03-fold) and decreased afterwards. No significant differences were found compared to the static control, suggesting that GLUT1 expression is not governed by fluid dynamics.

2.4.5. P-glycoprotein efflux activity is decreased upon high shear stress exposure

Although total cellular expression was constant under steady flow (Figure 2.18.B), P-gp efflux activity was tested using Rhodamine 123 (Rho123) as a fluorescent P-gp substrate.[174] Results in Figure 2.19 show the concentration of secreted Rho123 into the culture media after exposure and incorporation of the substrate into the cells.

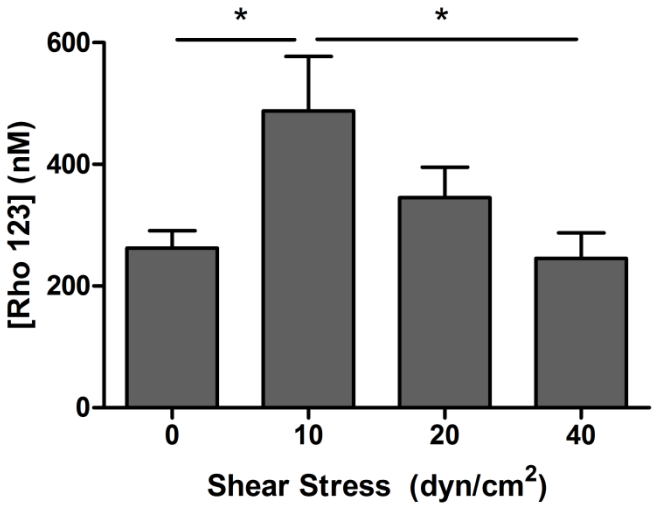

Figure 2.19. Effect of shear stress on P-gp efflux activity.

A significant activity peak was achieved at 10 dyn/cm^2, which was 1.86±0.29-fold higher than the static control. Beyond 10 dyn/cm^2, efflux activity decreased and resulted in lower concentrations of Rho123. A significant minimum activity was found at 40 dyn/cm^2, where the measured Rho123 concentration was 2.00±0.36-fold lower than the peak at 10. This suggests that, although the expression of P-gp is constant under steady shear stress, its efflux activity can be modulated by flow. Some studies suggest that transmembrane active P-gp may be internalized and deactivated upon transport requirements.[175]

2.4.6. Tight junction markers can be recovered when physiological shear stress is reestablished

After analyzing the effect of shear stress on tight junction and transport markers, microvascular endothelium response to temporary modifications of fluid dynamics was investigated. HBMEC were exposed to steady shear stress of 10 or 40 dyn/cm^2 for 3 days. Then, as Figure 2.20 illustrates, cells were either kept at their initial shear for three more days (Group A: 10 dyn/cm^2; Group B: 40 dyn/cm^2) or switched from one to the other (Group C: 10 → 40 dyn/cm^2; Group D: 40 → 10 dyn/cm^2). HBMEC were lysed and tight junction markers were analyzed by Western blotting (Figure 2.21.A).

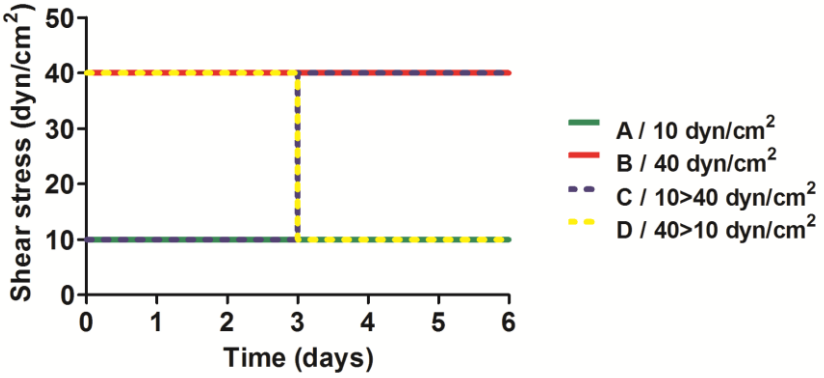

Figure 2.20. Time plan for the study of shear stress induced effects reversibility.

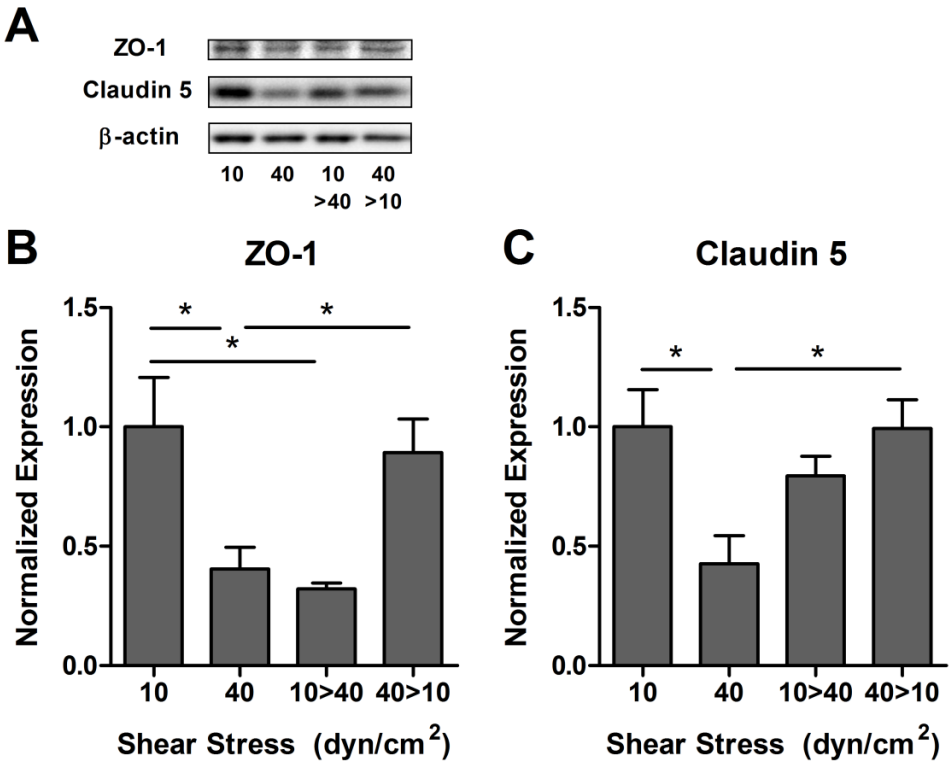

Figure 2.21. Shear stress reversibility effects on tight junction markers.

As expected, the expression of ZO-1 and Claudin-5 (Figure 2.21.B and C) showed a significant downregulation at 40 dyn/cm^2 compared to 10 dyn/cm^2 (0.41±0.09 and 0.43±0.12, respectively). Interestingly, when cells cultured at 40 dyn/cm^2 were switched to 10 dyn/cm^2, the expression of tight junction markers was significantly recovered and was comparable to the expression of cells maintained at 10 dyn/cm^2 for the entire experiment (0.89±0.14 and 0.99±0.12 for ZO-1 and Claudin-5, respectively). This indicates that HBMEC may recover their BBB phenotype when the alteration of their normal fluid dynamic conditions is reversed. On the contrary cells exposed to 10 dyn/cm^2 and switched to 40 dyn/cm^2 showed a significant ZO-1 downregulation (0.32±0.02) similar to the level of cells maintained at 40 dyn/cm^2 (Figure 2.21.B). Under the same circumstances, Claudin-5 showed resistance to pathological shear exposure and its expression decreased non-significantly (Figure 2.21.C).

2.4.7. Effects induced by shear stress in HBMEC are modulated via the Src/ERK signaling pathway

Phosphorylation analysis of Src and ERK1/2 was assessed by Western blotting after HBMEC exposure to flow (Figure 2.22.A). Under physiological conditions, Src and ERK1/2 are inhibited and upregulate tight junction markers. Results showed that ERK1/2 (Figure 2.22.B) and Src (Figure 2.22.C) are inhibited in cells stimulated with steady shear stress of 10 and 20 dyn/cm^2. Both phosphorylation ratios decreased significantly compared to the static control (ERK1/2, 0.25±0.07; Src, 0.77±0.03 at 20 dyn/cm^2). Subsequent increase of shear stress to 40 dyn/cm^2 activated the Src/ERK pathway showing a significant increase in phosphorylation compared to capillary-like shear stress levels (ERK1/2, 2.3±0.6; Src, 1.2±0.05). When cells were stimulated with pulsatile flow, phosphorylation ratios were equivalent to high steady shear stress levels independently of the pulsatile shear stress applied.

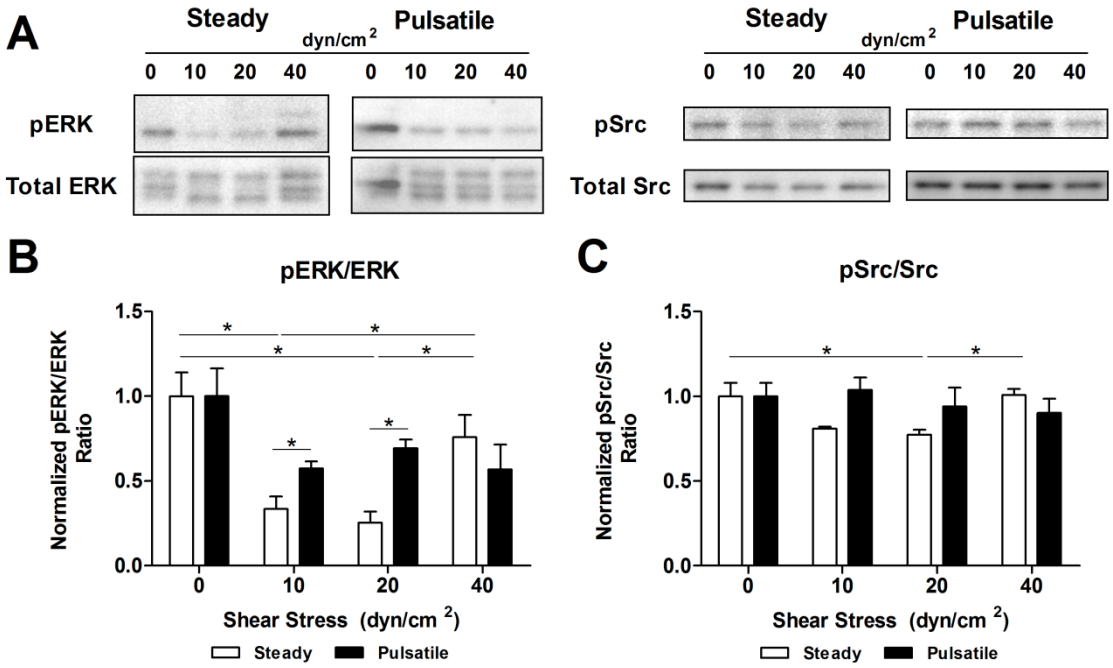

Figure 2.22. Effect of shear stress on the activation of Src and ERK1/2.

Overall deviations from physiological dynamic conditions in HBMEC lead to the activation of stress signaling cascades Src and ERK, which in turn triggered a downregulation of tight junction markers (Figure 2.23). The proposed mechanism depicted in Figure 2.23 is originated by shear stress mechanosensing by G-coupled protein receptors (GPCR). This leads to activation of tyrosine-protein kinases (Src) and extracellular signal-regulated kinases (ERK1/2), which directly induces downregulation of the expression of tight junction markers.

2. Pulsatility and high shear stress deteriorate barrier phenotype in brain microvascular endothelium

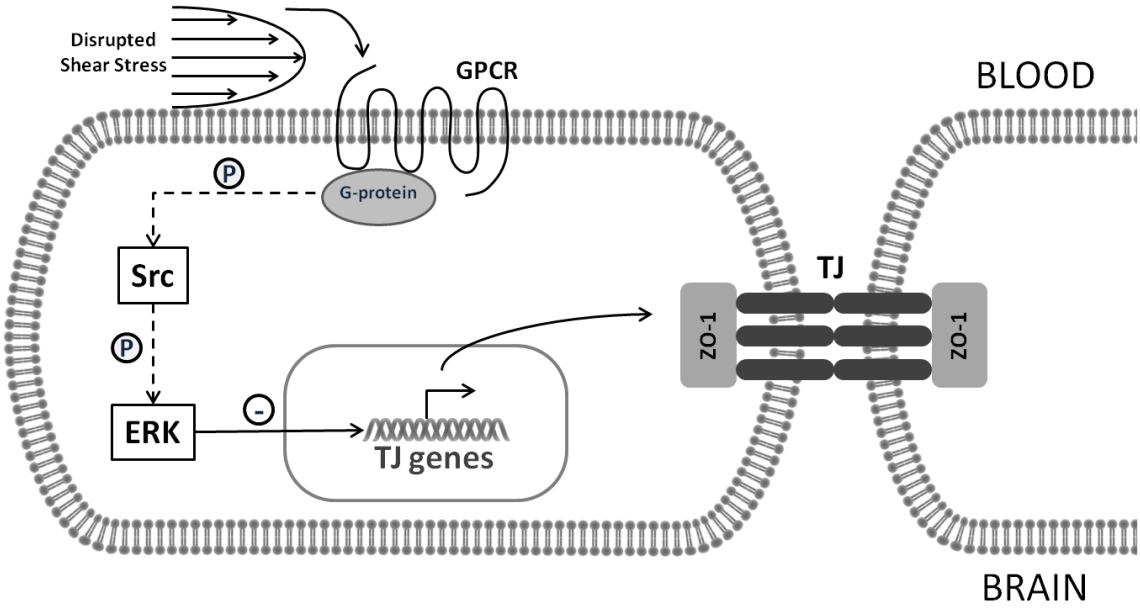

Figure 2.23. Proposed mechanism for tight junction modulation induced by shear stress via Src/ERK signaling pathway.

2.5. Study of BBB markers and permeability in hypertensive rats

Shear stress effects on the BBB found in Chapter 2.4 were evaluated in a small group of normotensive (Control; n = 2) and stroke-prone spontaneously hypertensive (SPSHR; n = 4) rats, with the latter as a model of altered shear stress with higher pulse pressure and blood velocity reaching the brain microcirculation. Tight junction markers ZO-1 and Claudin 5 were analyzed, followed by a permeability assay using Evans Blue dye (EBD), a common vascular permeability tracer in animal models.[176,177]

2.5.1. ZO-1 and Claudin 5 expression in hypertensive rats

Protein lysates from homogenized rat brains were analyzed with Western blot, where ZO-1 and Claudin 5 were detected and quantified (Figure 2.24).

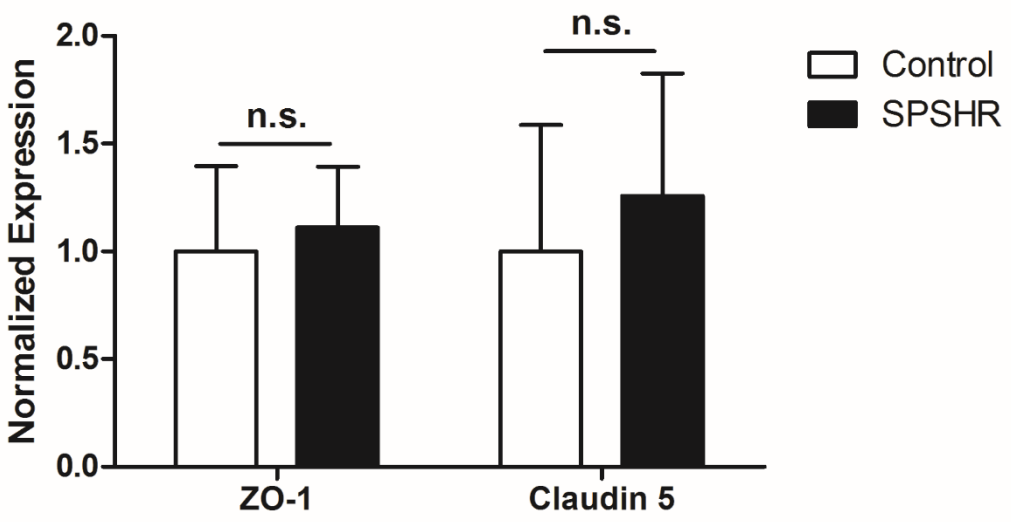

Figure 2.24. Expression of ZO-1 and Claudin 5 in normotensive and hypertensive rats.

No significant differences were found on the expression of both ZO-1 and Claudin 5 between normotensive and hypertensive rats.

2.5.2. EBD permeability assay in hypertensive rats

EBD was incorporated in the animal vasculature through intravenous tail vein injection. After 2 hours, rats were euthanized and EBD concentration was measured in brain homogenates. Figure 2.25 shows EBD concentration in extravasated rat brains, showing no significant difference between the control and the hypertensive groups.

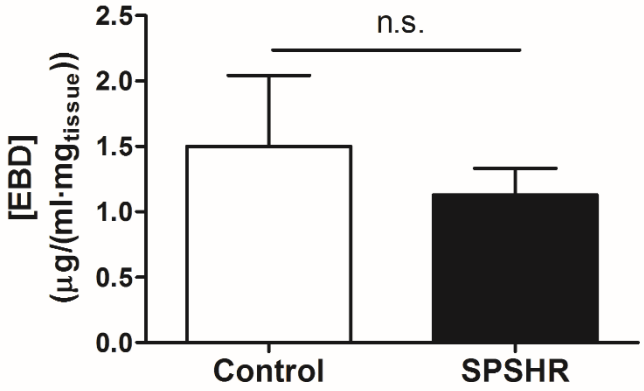

Figure 2.25. Cerebral concentration of extravasated Evans Blue dye in hypertensive rats.

2.5.3. Limitations and future improvements in animal experiments

No significant difference was found on both the expression of tight junctional markers and permeability assay between normotensive and hypertensive groups. Statistical relevance in *in vivo* experimentation is typically harder to assess compared to *in vitro* research. Experimental groups need to be larger in order to detect patterns. The main limitation of our preliminary animal study was the small number of rats per group, which was only 2 and 4 in the control and hypertensive groups, respectively. As a preliminary study, the complex techniques performed had to be learned, adapted and tested for the first time in our research group.

Furthermore, both techniques had additional limitations with potential error increases. First, protein lysis was done on whole brain. While ZO-1 and Claudin 5 are specific markers of microvascular endothelium, α-tubulin, which was used as a loading control, is present in all cells. Normalized junctional expressions resulted in lower ratios compared to the same technique in cell lysates. Endothelial cell purification from brain samples should be added as an additional step before sample lysis. In the case of permeability assays, longer EBD exposure time through brain vasculature might provide would allow detecting larger differences.

Higher study groups and optimized techniques might allow a better evaluation of the effect of vascular alterations in the BBB.

2.6. Discussion

Understanding the mechanisms underlying BBB phenotype is essential for the study of brain-related diseases. Better drug candidates targeting the CNS may be developed if these mechanisms are fully understood. This study adds to our understanding of the pathophysiology of neurological diseases linked to BBB dysfunction caused by systemic hemodynamic factors.

This chapter demonstrates that a biomechanical stimulus like shear stress is crucial to maintain a functional BBB. When physiological conditions are lost, a decrease of junction markers expression, an efflux activity reduction, and junctional widening is observed. The findings shown suggest that brain microvascular endothelial cells state is critical to cerebrovascular function. Abnormal flow patterns in the systemic vasculature may jeopardize endothelial behavior at the neurovascular unit, and impact transport at the BBB, resulting in a loss of functionality of the neurovascular unit. Results from this chapter show that high shear stress and pulsatile flow downregulated significantly the total expression of tight junction markers ZO-1 and Claudin-5. Moreover, abnormal flow induced ZO-1 delocalization from cell junctions towards cytoplasm and nuclei.

Flow waveform corrections are limited by ageing-associated arterial stiffness, which transports increased pulse pressure to peripheral organs.[120] While shear stress in healthy brain capillaries is mostly steady and typically lower than 20 dyn/cm^2 [71,109,110] higher levels and pulsatile patterns might reach the endothelium in patients with increased arterial stiffness. Similarly, patients who suffer stroke or trauma lose the signaling mechanisms that regulate microvessel hemodynamics in brain microcirculation.[139]

Shear-induced effects on the endothelium have been widely studied in larger vessels[108,178,179], but less is known about the consequences of shear stress alterations in the brain microvascular endothelium. Here, the dynamic vascular spectrum is extended beyond capillary-like rates at the BBB and hemodynamics at the cellular level in HBMEC are analyzed. It is shown how critical markers of tight junctions (ZO-1 and Claudin-5) or efflux transport (P-gp) are upregulated under capillary-like shear stress. Conversely, high shear stress (40 dyn/cm2) and pulsatile profiles downregulate the expression of tight junction markers and the efflux activity of P-gp. To date, studies using *in vitro* dynamic models of the neurovascular unit have focused on capillary-like shear stress only. Results using physiological conditions agree with previous reports as shear stress in such ranges promotes barrier phenotype. In a recent study, moderated shear stress (6.2 dyn/cm^2) showed significant benefits in brain microvascular endothelial cells when compared to static cultures.[71] Using a hollow-fiber based co-culture device, an upregulation was

observed in genes related to tight junctions, drug transporters, ion channels, adhesion molecules and integrins. As a difference to this study, the *in vitro* system used in this thesis allows cellular visualization, local protein expression quantification and a wide range of hemodynamic parameterization. The lack of astrocytes was corrected with the incorporation of human astrocyte-conditioned medium into the experimental setup, which enhanced tight junctional formation. Characterization of HBMEC in this series of experiments showed maximal total expression of BBB markers in static cultures after 96 hours, a duration that falls inside the duration range of other dynamic published studies.[71,109,112,113] We repeated the same experiment under dynamic physiological conditions and, in agreement with the static data, total expression of BBB markers was also highest at 96 hours. Using this time point, we avoided the typical loss of phenotype due to long-term *in vitro* cultures. Although this model is not fully representative of the neurovascular unit, some of the BBB hallmarks were reproduced in a dynamic environment where barrier phenotype was altered by abnormal shear stress on the microvascular endothelium.

The results presented indicate that BBB can be disrupted when cells are exposed to altered flow patterns. Barrier phenotype loss is critical to the etiology of different types of neurological diseases.[36,180] Recent findings have shown how disruptive effects in HBMEC of tumor necrosis factor-α (TNF-α) and interleukin-6 (IL-6) can be relieved by capillary-like (8 dyn/cm^2) shear stress.[112,113] However, such protective effect may be lost under high shear stress and pulsatile flow patterns.

Special attention must be paid on pulsatile flow reaching the brain microvasculature. Cerebrovascular damage can be caused by arterial stiffening and hypertension, which provoke high shear and/or pulsatile flow in brain capillaries.[132,140] Here, we show that pulsatile flow in the microvasculature can cause tight junctional impairment and loss of barrier phenotype in brain microvascular endothelial cells. In the experiments performed, steady high shear stress and all pulsatile shear stresses deteriorated the endothelial barrier functionality. Pulsatile shear stress induced ZO-1 translocation significantly from cell-cell junctions towards the cytoplasm and nucleus. It has been proved in the past that nuclear presence of ZO-1 can be caused by tight junction immaturity in *in vitro* cultures.[181] In our study, endothelial cells were in culture for a total of six days, two days during the seeding process and four days under flow. Despite observing some nuclear presence of ZO-1 under static conditions, we only observed significant translocation when we exposed our cells to high shear or pulsatile shear stress. Our results indicate then that high and pulsatile shear stress may be an impediment in cell-cell contacts formation and tight junction maturation. Our findings also suggest an inverse correlation of

phosphorylation ratio of Src and ERK1/2 with tight junction expression levels. This finding is in agreement with the literature that shows that this pathway is flow sensitive[182–184] and how different insults to HBMEC lead to activation of Src[185,186], ERK1/2[187] and BBB alterations.[188]

A novel finding of this study is that shear-induced damage in the microvascular endothelium may be reversed if regular cerebral blood flow is recovered. Using non microvascular endothelial cells, other authors proved that alterations of electrical impedance in endothelial monolayers were reversible between static and dynamic cultures.[189,190] Here, loss of tight junction markers due to high shear stress was recovered if physiological conditions were restored. We have also observed that ZO-1 but not Claudin-5 was downregulated after imposing non-physiological flow. This observation is consistent with the reported plasticity of ZO-1 as rapid trigger of barrier phenotype loss, which should eventually be followed by Claudin-5 downregulation.[191] As the interface separating blood and the CNS, hemodynamic repair (pharmacological or interventional) could improve the performance of the neurovascular unit and mitigate the progression of neurological diseases through stabilizing shear stress at the BBB. A recent study showed how renal denervation treatment lead to permeability decrease and recovery of occludin expression in hypertensive rats.[164] The preliminary *in vivo* study performed on hypertensive rats did not show significant difference in both permeability assay and expression of ZO-1 and Claudin 5. Further technique optimization and increased study groups are required in order to evaluate the *in vitro* findings of this chapter in animal models. Carotid ligation surgery on a single brain hemisphere is a possibility that may induce increased vascular impairment in a specific region of the animal, allowing the assessment of functional BBB contrasts on each specimen directly.

This chapter adds insight into how shear stress governs barrier phenotype in microvascular endothelial cells. Physiological shear stress promotes the expression of tight junctions and transport markers. When such conditions are lost, mechano-transductors activate stress signaling pathways leading to a decrease in the expression of tight junction markers and a reduction of the efflux activity. Preliminary evidence is provided supporting the hypothesis that shear-induced damage in the endothelium may be reversed if physiological cerebral blood flow is recovered. Correlations between flow patterns and endothelial cell state at the BBB might be of help for the diagnosis and treatment of neurological diseases. This study opens a new frame to better understand and model cerebral diseases in which hemodynamic disorders and BBB disruption are involved.

3. Design and characterization of a dynamic *in vitro* BBB model

3.1. Device conception and requirements

In Chapter 2, shear stress alterations on brain microvascular endothelial cells showed significant impact in dynamic HBMEC monocultures. While it was shown that astrocyte-conditioned medium (ACM) as a supplement for endothelial cultures enhanced tight junction formation, the model used was not fully representative of the BBB, as it lacked of the presence of astrocytes as neighboring cells providing biophysical support to the microvascular endothelium. Exposure of shear stress to brain microvascular endothelial cells in co-culture with astrocytes further promotes functional BBB phenotype in *in vitro* models.[71] In the following chapter, a dynamic *in vitro* model of the BBB is designed and characterized with the aim of reproducing the results previously obtained in a more relevant biological environment.

Given that commercially available culture systems that allow shear stress exposure and co-culture are expensive and have a small size that limits genomic and proteomic assays, such requirements are often achieved by cell culture chambers custom-made for a given study. As described in Chapter 1.1.6, different approaches currently exist to include circulation in BBB *in vitro* models. Here, we designed a two-compartment parallel plate flow chamber (PPFC) system, based on a modified Boyden chamber device. Table 3.1 collects the main requirements of the PPFC after consideration of handling and post-process aspects. Figure 3.1 shows the final design of the chamber with its main components, including the abluminal/astrocytic and luminal/endothelial compartments (1, 2), a porous membrane separating them and allowing exchange of soluble factors with no cell migration between compartments (3), inlet and outlet ports (4) and two frames to hold the system together (5).

Table 3.1. Parallel-plate flow chamber design requirements.

Requirement	Justification
All PPFC components need to be autoclavable and transparent.	The whole system needs to be sterile prior to cell culture and inside visibility must be guaranteed to check proper media coverage during experiments.
Presence of two independent compartments separated by a porous membrane.	Compartmentalized co-culture of endothelial cells and astrocytes on each side with continuous exchange of soluble factors and potential cell contact via membrane pores with no migration of cells from one side to the other.
Presence of inlet/outlet ports on each compartment.	Cell seeding, media perfusion for dynamic cultures and sample collection.
High cell seeding area (50x18mm).	Possibility to seed high cell number to perform proteomic and genomic assays.
Height-to-width ratio higher than 20 on the endothelial compartment.	Controlled and constant shear stress along the chamber (Equation 3.1).

Besides allowing compartmentalized co-culture, an additional benefit of this customized PPFC is that the membrane can be selected according to the assay that will be performed. Membrane pore size and thickness can be adapted for experimental techniques such as drug transport or permeability assays (small pore size)[64,192] or cell migration, invasion and chemotaxis (larger pore size).

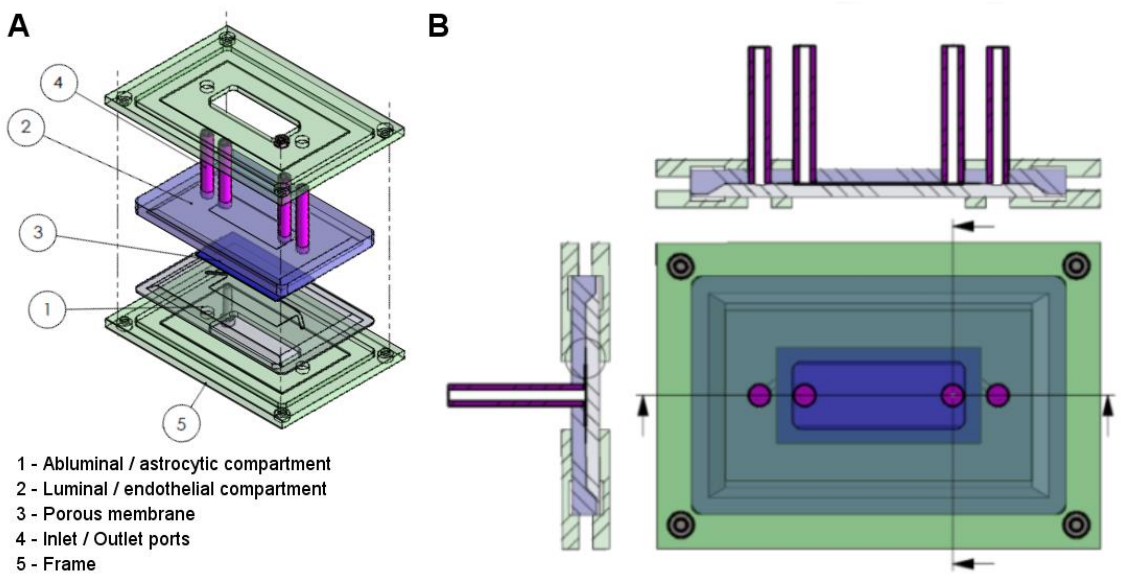

Figure 3.1. Exploded view of the parallel-plate flow chamber assembly (A) and top and lateral views of the assembled device (B).

3.2. Device manufacture

Negative Teflon molds were first manufactured (Figure 3.2.A), which allowed manufacturing of endothelial and astrocytic compartments with PDMS (Figure 3.2.B). Silicone tubing parts were placed in the circular protrusions on the endothelial negative mold prior to PDMS polymerization in order to integrate inlet and outlet ports. The resulting parts were coupled with a porous Teflon membrane in between. The membrane was first glued to the astrocytic side (Figure 3.2.C) and then both compartments were glued together (Figure 3.2.D). The final assembly was then autoclaved and ready to be used.

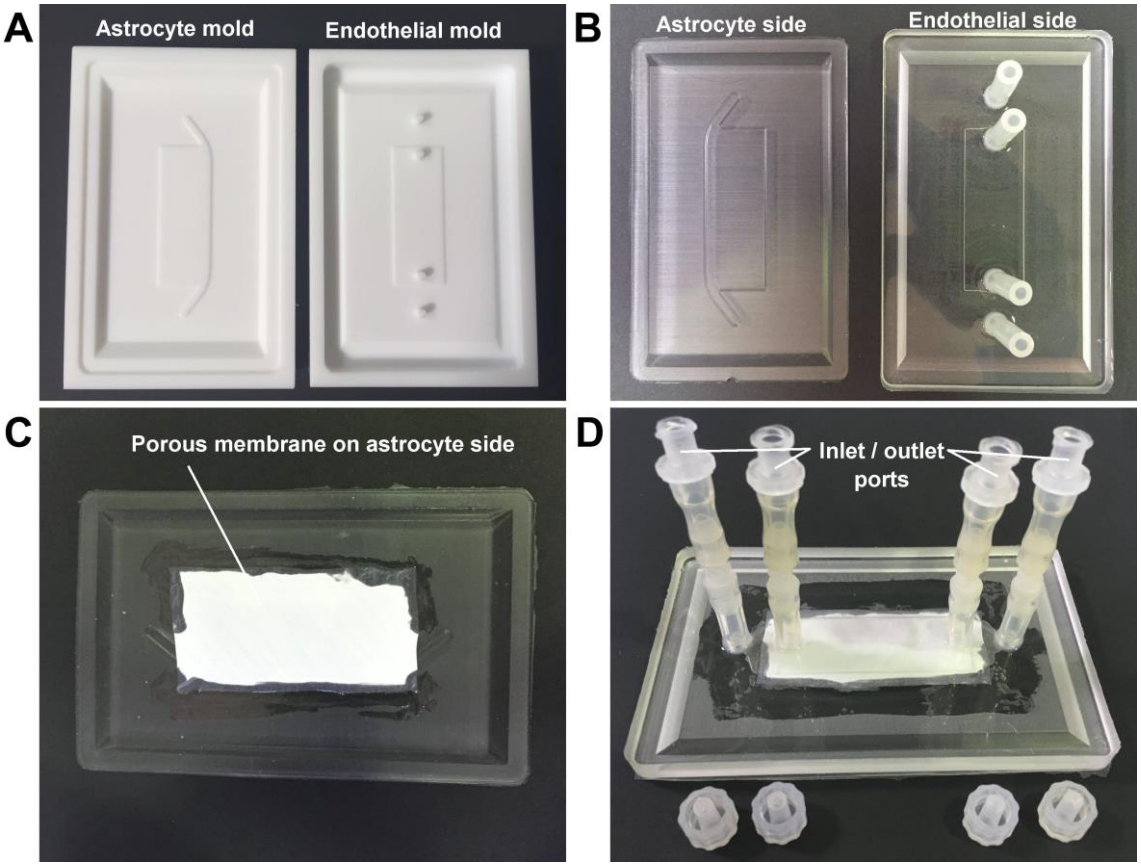

Figure 3.2. Manufacture steps of the parallel-plate flow chamber.

3.3. Fluid dynamics validation

Shear stress along a PPFC can be estimated assuming the fluid considered is Newtonian. Assuming steady flow (Q) in an infinitely wide flow channel, Equation 3.1 allows the estimation of shear stress (τ) on the surface of the chamber.

$$\tau = \frac{6 \cdot \mu \cdot Q}{w \cdot h^2}$$ **Equation 3.1**

Where w and h are the width and height of the channel and μ is the viscosity of the fluid. Flow profile is parabolic between both plates of the chamber, with a maximal and constant shear along the surface. Equation 3.1 is valid to evaluate the average and/or maximal shear stress with dynamic flow patterns in PPFC with a width-to-height ratio (w/h) higher than 20. The necessary distance for flow to develop in the chamber can also be estimated according to Equation 3.2.

$$L_e = 0.04 \cdot h \cdot Re$$ **Equation 3.2**

In order to evaluate shear stress along the endothelial compartment of the designed PPFC, computational fluid dynamics (CFD) simulations were performed using a computer-aided design (CAD) model of the PPFC. For shear stresses of 10, 20 and 40 dyn/cm^2, calculated velocities through the circular inlet of the channel were 7.7, 15.3 and 30.7 cm/s, respectively. Given those inlet velocities as boundary conditions of the model, steady state simulations provided velocity and shear stress profiles. Expected parabolic velocity profiles between plates (vertical direction in Figure 3.3) were observed in all scenarios. Constant shear stress was also observed along the surface of the PPFC (Figure 3.4), with the exception of inlet and outlet regions where shear stress is significantly higher due to the 90° flow direction change.

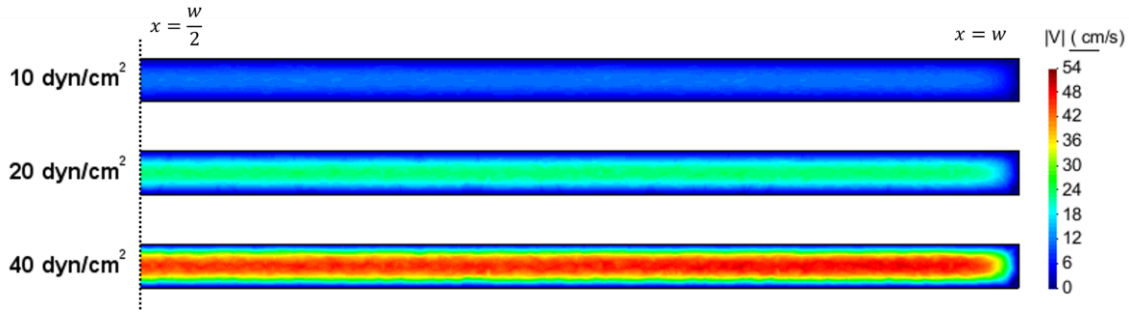

Figure 3.3. Laminar parabolic velocity profiles between plates in half symmetric cross-sections of the parallel-plate flow chamber.

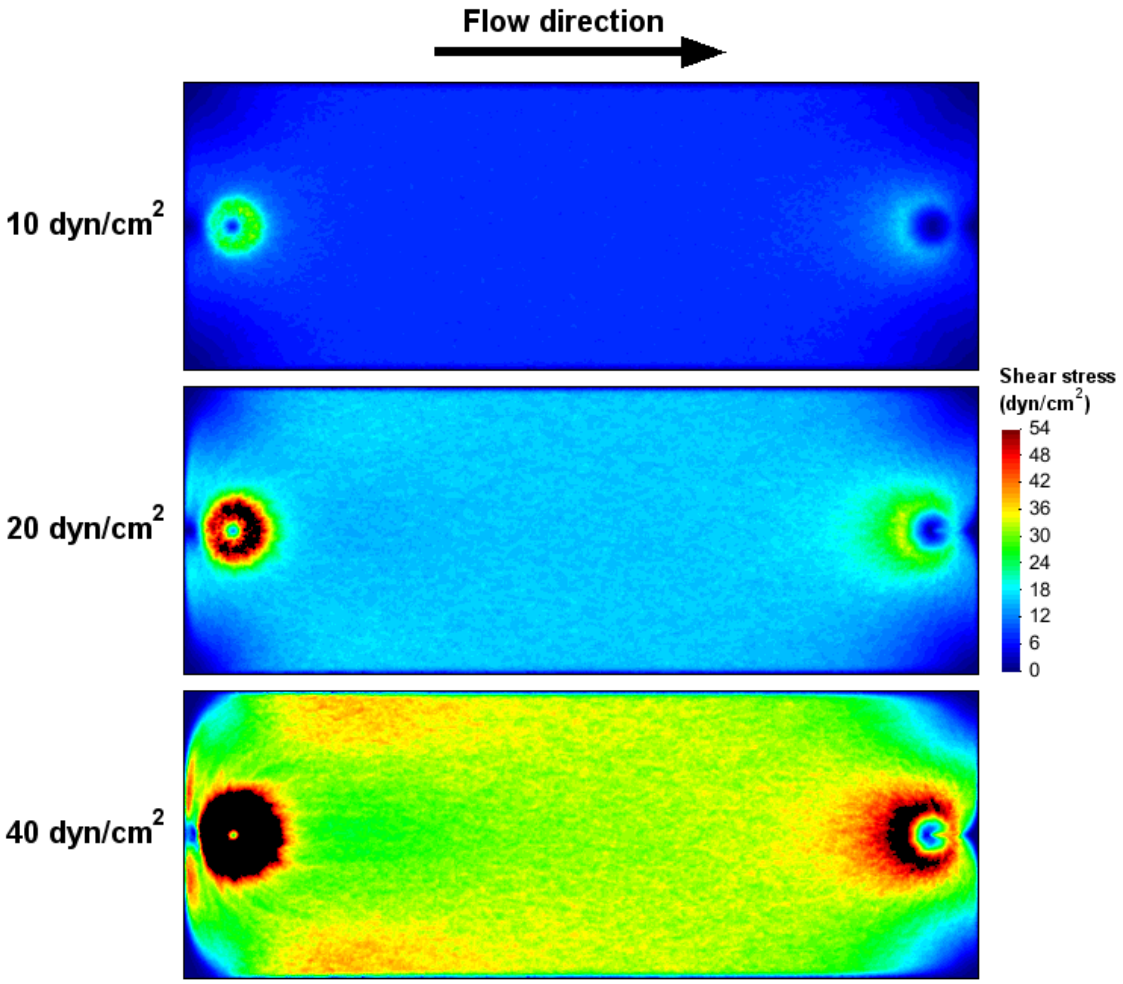

Figure 3.4. Shear stress profile in bottom endothelial plate of the parallel-plate flow chamber.

Shear stress profiles were represented between the lower surface boundaries at the middle region of the PPFC (Figure 3.5), confirming constant profiles.

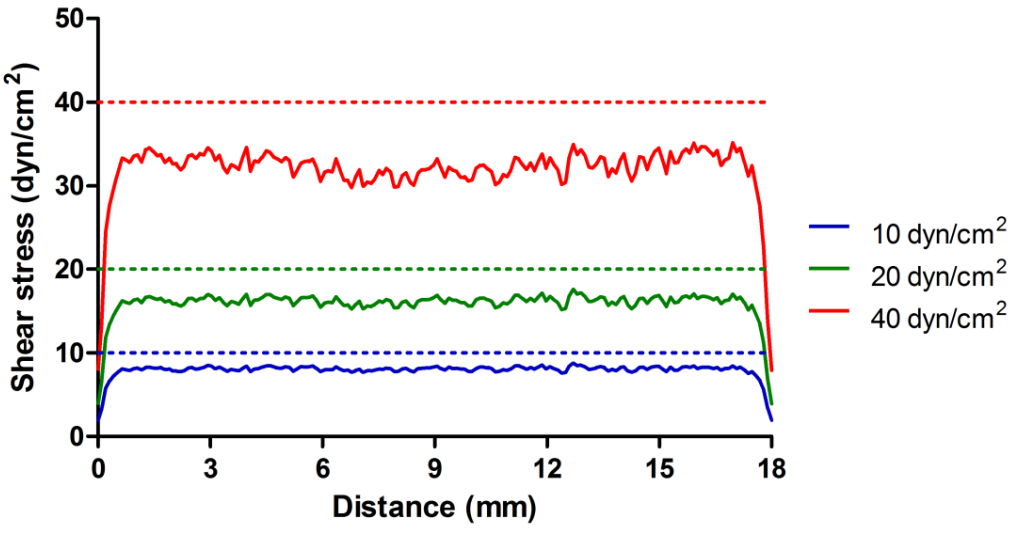

Figure 3.5. Shear stress profiles along the lower surface of the parallel-plate flow chamber.

Despite having a high width-to-height ratio (w = 450 μm; h = 18 mm; w/h = 40), the expected theoretical forces (dashed lines) were not achieved and discrepancies increased with velocity. The vertical disposition of the inlet port might generate turbulences when flow enters the channel, resulting in a reduced shear stress after parabolic flow is developed. A linear trend between velocity and average surface shear stress (Figure 3.6) allowed calculating the target velocities that would provide the expected shear stress (Table 3.2).

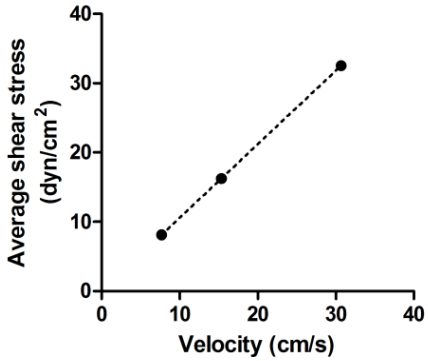

Figure 3.6. Linear correlation between theoretical velocity and average shear stress.

Table 3.2. Computational fluid dynamics average shear stress and target velocities.

Velocity (cm/s)	Average shear stress (dyn/cm²)	Expected shear stress (dyn/cm²)	Target velocity (cm/s)
7.7	8.1	10	9.5
15.3	16.2	20	18.9
30.7	32.5	40	37.7

A second set of simulations using new velocities was run. Figure 3.7 shows that the expected constant shear stress profiles were reached using target velocities. Velocities calculated in Table 3.2 will be used in future dynamic culture experiments with the PPFC.

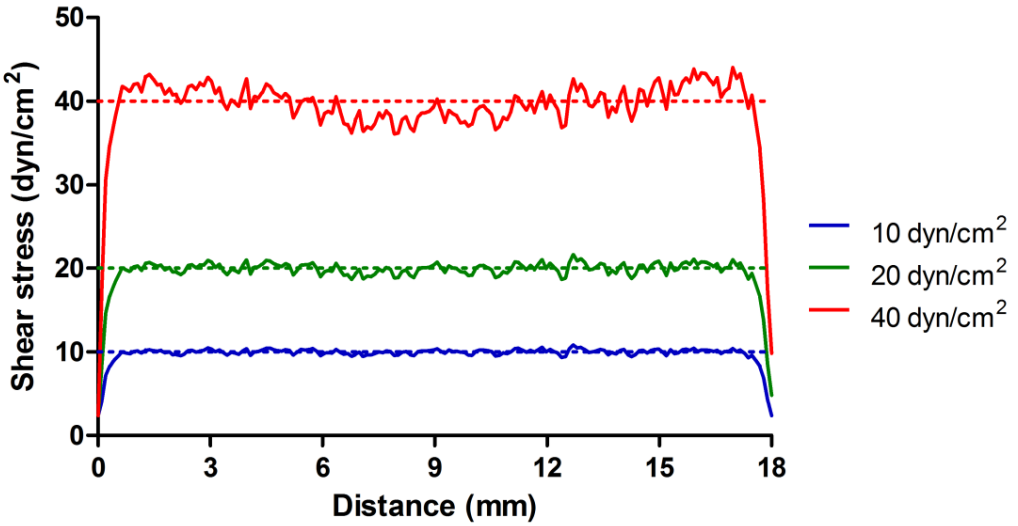

Figure 3.7. Corrected shear stress profiles along the lower surface of the parallel-plate flow chamber.

3.4. Cell seeding and attachment

Before exposing cells to flow in the PPFC, proper cell seeding and attachment to the membrane needed to be ensured. Primary human brain microvascular endothelial cells (HBMEC) and human astrocytes (HA) were seeded on each side of the PPFC and fluorescent stains allowed the evaluation of cell coverage and confluence.

3.4.1. HBMEC and HA mono-culture

HBMEC and HA were first seeded independently on the porous membrane in their respective compartments in different PPFC. After 24 hours, cells were fixed and actin filaments were stained with phalloidin. Figure 3.8 shows successful cell attachment to the membrane for both cell types. However, confluence was not reached after 24 hours, with a lower abundance of non-covered gaps in the case of HBMEC than in HA (Confluence of 87.9% and 49.2%, respectively). Longer static culture time lead to 100% cell confluence along the membrane.

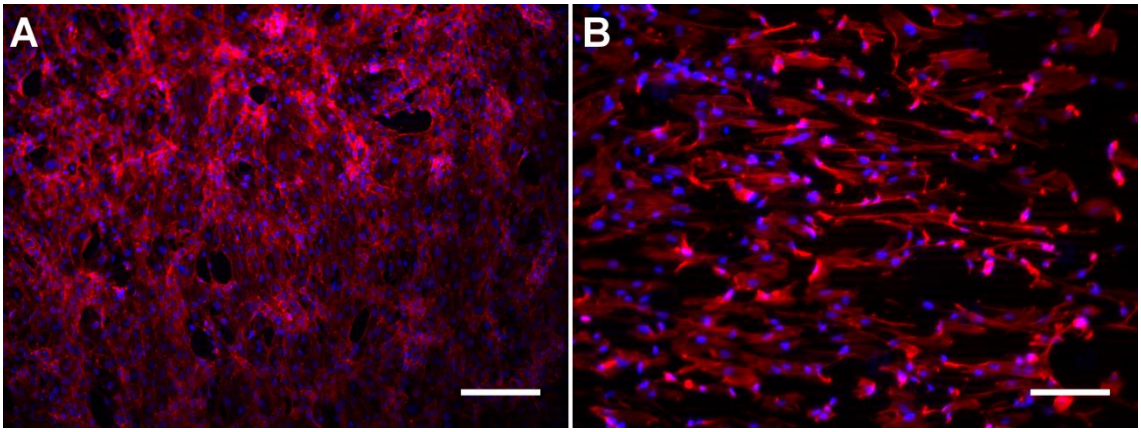

Figure 3.8. Mono-culture of HBMEC (A) and HA (B) on the membrane of the parallel-plate flow chamber. (Red: actin; Blue: nuclei; Scale bar = 20µm.

3.4.2. HBMEC/HA co-culture

HBMEC and HA were co-cultured on both device compartments of the PPFC to evaluate simultaneous cell attachment to opposite sides of the membrane. Phalloidin staining showed confluent monolayers of HBMEC (Figure 3.9.A-B) and HA (Figure 3.9.C-D) on each side of the membrane. The different cellular morphology displayed by stained actin filaments suggested the presence of both cellular entities on each side, with no cross-contamination between the PPFC compartments.

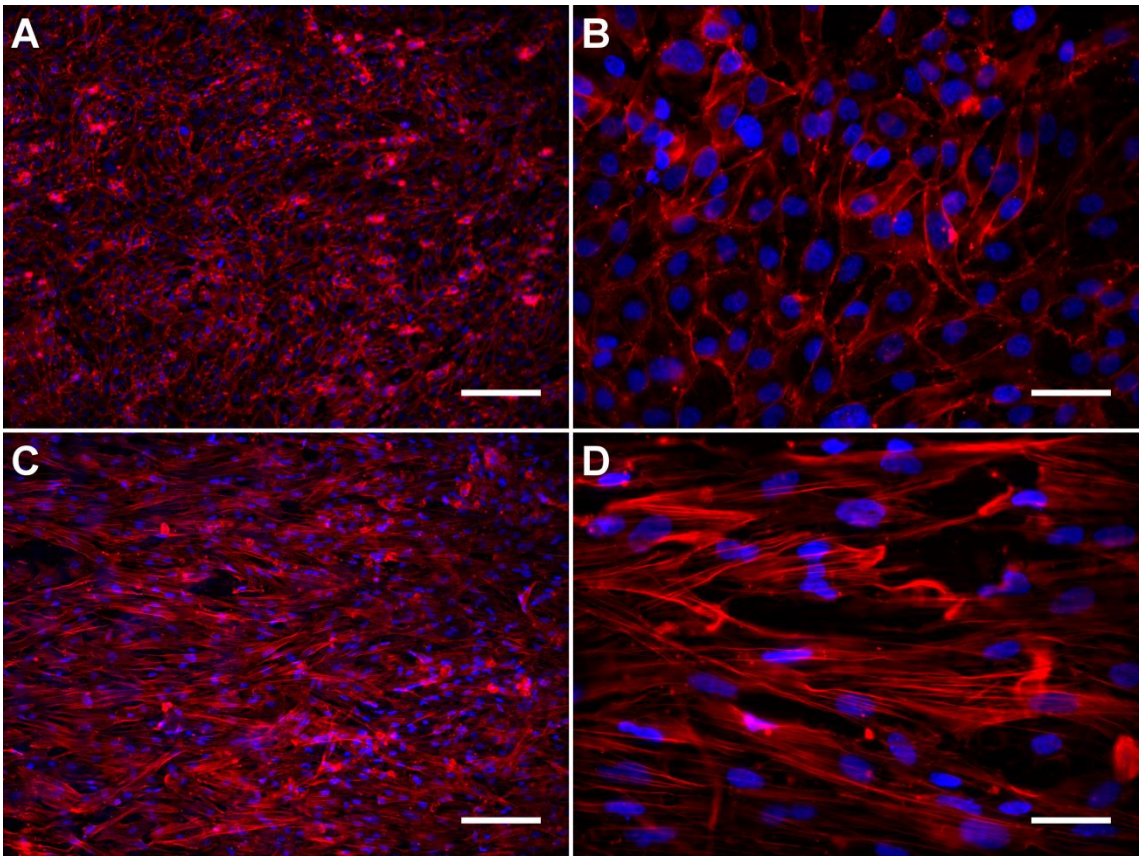

Figure 3.9. Co-culture of HBMEC (A, B) and HA (C, D) on the membrane of the parallel-plate flow chamber. (Red: actin; Blue: nuclei; Scale bar = 20µm (A, C) / 5 µm (B, D)).

However, when confluent layers were focused on each side of the membrane (Figure 3.9), the layer behind could not be visualized under an epifluorescent microscopy. In order to evaluate the presence of each cell on its respective side simultaneously, unstained HBMEC and green cell tracker stained HA were co-cultured in a PPFC and allowed to attach with a short culture time avoiding confluence. Imaging of the same area allowed focusing at both sides of the membrane. Focused cell nuclei on the astrocytic compartment (Figure 3.10.A) became fuzzy when the focus was switched to the endothelial compartment (Figure 3.10.B) and vice versa. The distance between both focus points matched the thickness of the membrane (85 µm), corroborating that cells were attached on both sides. Furthermore, focused green cell tracker was only present on the astrocytic compartment, confirming optimal co-culture seeding with no cross-contamination.

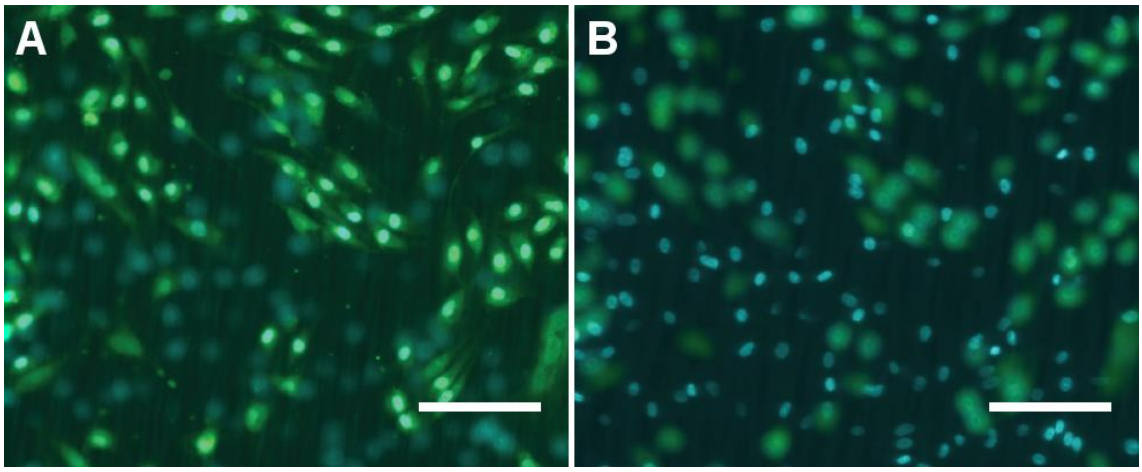

Figure 3.10. Co-culture of HBMEC and HA focusing the astrocytic (A) and endothelial (B) sides of the membrane (Green: astrocytes; Blue: nuclei; Scale bar = 10 µm).

In order to confirm that cells were properly attached on its corresponding side of the membrane, an additional membrane was fixed, HA and HBMEC were stained with green cell-tracker and CD31, respectively, and observed under a confocal fluorescent microscope. Figure 3.11 shows that both cells are attached in opposite sides of the membrane validating again that no cross-contamination occurred during the co-culture steps in the PPFC.

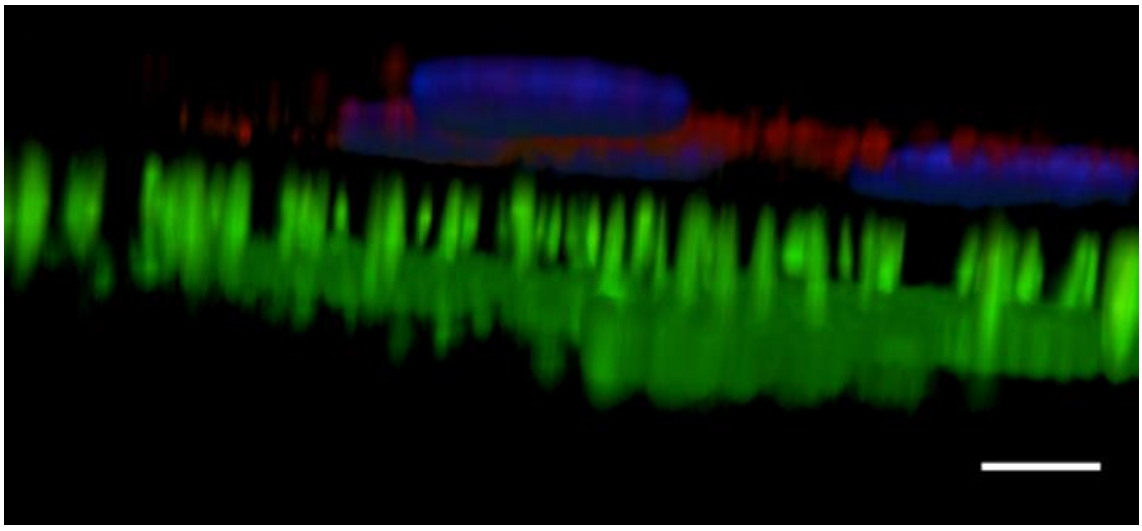

Figure 3.11. Three-dimensional reconstruction of HBMEC and HA in co-culture on each side of the membrane in the parallel-plate flow chamber (Green: astrocytes; Red: HBMEC; Blue: nuclei; Scale bar = 1 µm).

3.4.3. Microvascular endothelial morphology

Endothelial morphological verification is essential in order to perform *in vitro* BBB assays in any cell culture platform. Cell morphology and the expression of key endothelial markers were assessed in a PPFC where HBMEC were grown to confluence. Cells were immunostained with endothelial specific marker CD31[193] and tight junction specific marker ZO-1.[14] Figure 3.12 shows positive staining of both markers in a confluent monolayer of HBMEC. Cells displayed their typical endothelial cobblestone morphology with co-localization of gap junction and tight junction markers in intercellular contacts.

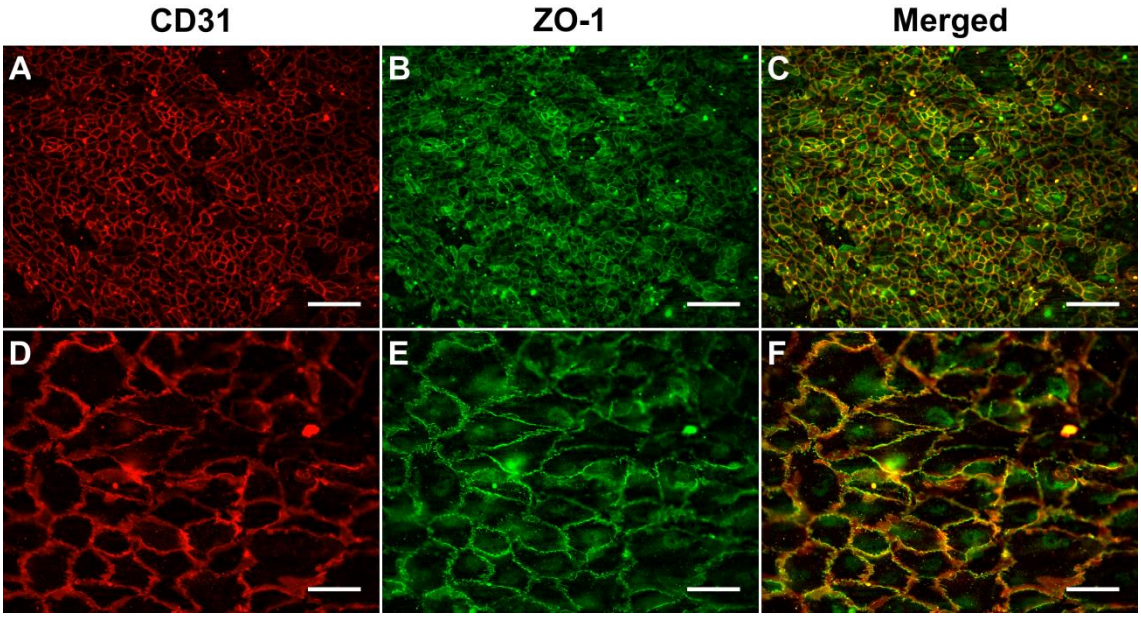

Figure 3.12. Expression of CD31 (A, D, red) and ZO-1 (B, E, green) in HBMEC, co-localizing at cell-cell junctions (C, F) (Scale bar = 20µm (A – C) / 5 µm (D – F)).

3.5. Assay development

Immunofluorescence staining protocols in the PPFC are relatively simple to perform even for co-culture in both sides of a membrane, as cells are fixed and attached. However, typical cell lysis protocols would result in a mix of protein or mRNA from different origin, given the presence of different cell types in porous membranes where reagents can easily diffuse. Techniques requiring cell lysis need to be properly defined in this type of culture device.

3.5.1. Cell lysis techniques

In order to obtain cell lysates from both sides of the membrane with no cross contamination, two different preliminary approaches (n=1) were followed after 24 hours of co-culture of HBMEC and HA in the PPFC. In the first case (method 1), the PPFC system was disassembled, membrane was extracted and lysis buffer was carefully added to each side, collecting lysates independently and keeping them in a centrifuge tube during incubation. The second option (method 2) consisted on harvesting cells from the assembled device by following the standard trypsinization protocol on each compartment and lysing cell pellets in centrifuge tubes. Western blots were performed on endothelial and astrocytic lysates from both techniques (Figure 3.13.A). Claudin 5 and GFAP, specific markers of HBMEC[13] and HA[26], respectively, were studied.

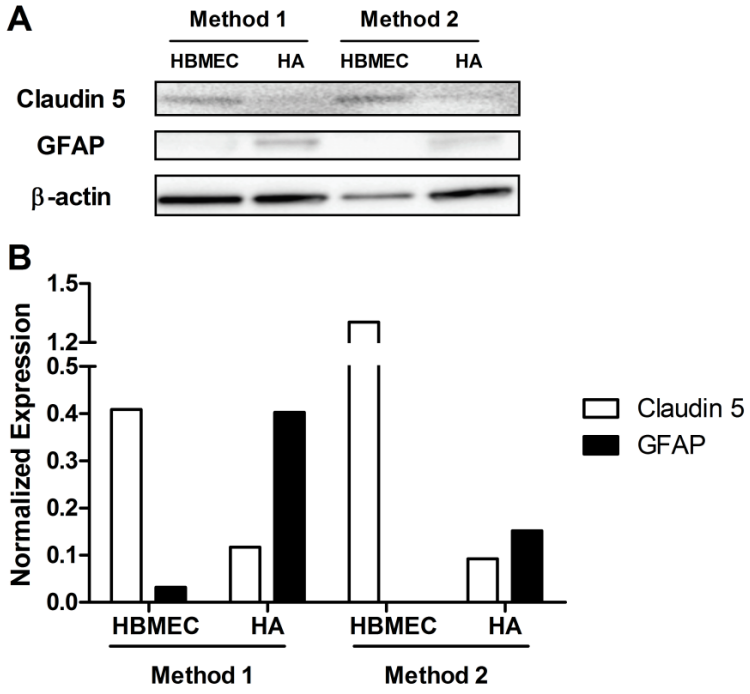

Figure 3.13. Expression of Claudin 5 and GFAP from HBMEC and HA lysates of the PPFC using different lysis techniques (n=1).

As seen in Figure 3.13.B endothelial and astrocytic lysates were positive and showed predominance on their respective analyte. However, impurities from the other side of the membrane were found in most cases. In the first method, GFAP blot intensity on the endothelial lysate represented 8% of the intensity on the astrocytic one, whereas Claudin 5 intensity on the astrocyte lysates was 29% of its endothelial counterpart. Lower impurity percentages were found on the second method where previous ratios were 0% and 7%, respectively. While the trypsinization method provided less contaminated samples, the total protein concentration of endothelial lysates was much lower compared to the *in situ* direct lysis procedure (0.2 mg/mL against 1.2 mg/mL). Further optimization of the direct lysis method was followed to obtain high protein concentration lysates with low impurities.

3.5.2. *In situ* direct lysis on PPFC membrane

Since microvascular endothelial cells are the main focus of study in dynamic BBB *in vitro* cultures, the following methods were developed to evaluate cell lysis efficiency from the endothelial compartment of the PPFC. Two cell separation methods were tested prior to cell lysis. On one hand, HA were scraped out of the membrane and lysis buffer was then poured in the membrane (method 1.1). On the other hand, HBMEC were first scraped and collected with PBS in a centrifuge tube followed by lysis buffer addition (method 1.2). HA were also lysed from the membrane in this case to compare GFAP expression with endothelial lysates from both methods.

Again, both options yielded positive Claudin 5 and GFAP positive detections in Western blot (Figure 3.14.A). Both methods showed low GFAP impurities on the endothelial lysates of methods 1.1 and 1.2, with a total amount of 2% and 7%, respectively, compared to the GFAP amount in the astrocyte lysate (Figure 3.14.B). While both methods showed negligible cross-contamination, method 1.2 had an additional protocol step resulting in a lower protein concentration (0.1 mg/mL) than method 1.1 (0.7 mg/mL).

Previous results suggest that HBMEC lysis is more efficient when HA are scraped out and HBMEC are lysed directly on the membrane. When astrocytes are not only needed as a BBB phenotype inducer for HBMEC, but are also of interest for post-analysis, cell separation by trypsinization in each compartment can still yield pure cell lysates from both cell types, but with lower protein concentration.

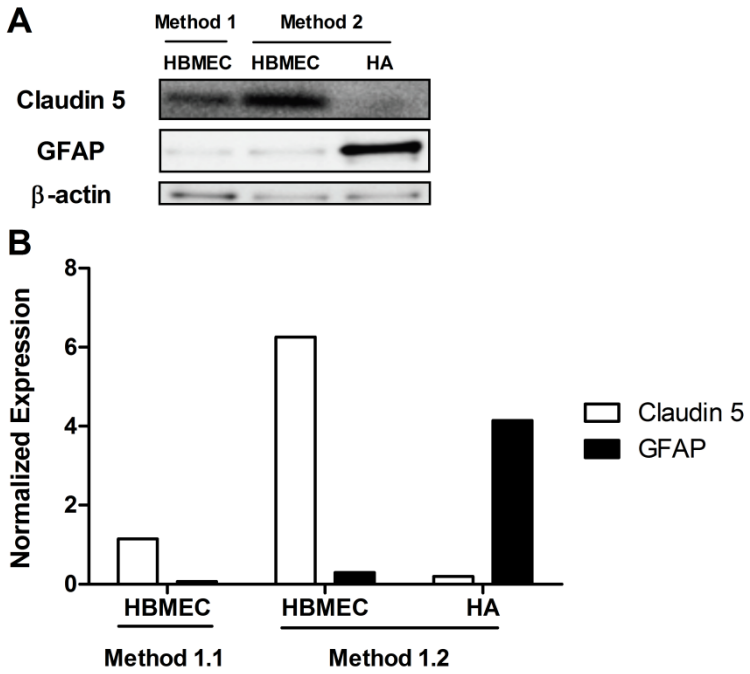

Figure 3.14. Expression of Claudin 5 and GFAP from HBMEC and HA lysates of the PPFC using different *in situ* membrane lysis techniques (n=1).

3.6. Exposure to flow

HBMEC were grown on the endothelial compartment of the PPFC for 24 hours. Then, cells were exposed to shear stress from 5 to 40 dyn/cm^2 for 48 hours. Unfortunately, the lowest shear stress chamber was the only to withstand the experiment. At 5 dyn/cm^2, the PPFC showed no apparent damage and cells remained attached to the membrane and confluent (Figure 3.15).

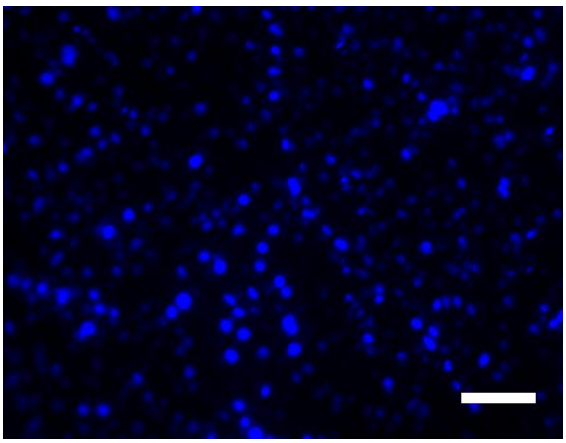

Figure 3.15. Nuclei labeling of HBMEC after 48 hours of exposure to 5 dyn/cm^2 (Scale bar = 20µm).

At higher flow rates, either no cells were on the membrane or both chamber compartments had detached and media had leaked out from the system. The performance of the device in such

dynamic conditions was then re-evaluated in non-sterile uncultured devices. Distilled water was used to perfuse through the system. When the system was filled with water, constant swelling of the endothelial compartment exposed to flow was clearly noticeable (Figure 3.16). After thorough inspection of the chamber, it was concluded that an over pressure was being generated inside the chamber by the fact that the membrane was not attached to the PDMS compartments tight enough and was very close to the inlet/outlet ports (0.45 mm). Both ports perfuse media on a 90° direction with respect to the PPFC flow direction which moves the outlet part of the membrane towards it, reduces the outlet section and increases pressure inside the device.

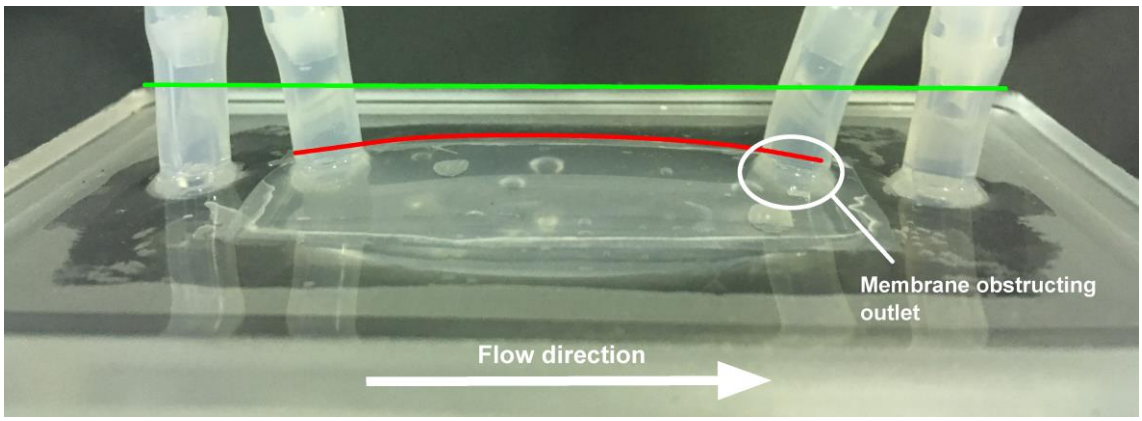

Figure 3.16. Swelling of the endothelial compartment of the PPFC. (Green: Straight PPFC; Red: Swelled surface).

Such overpressure causes three main problems. First, cells seeded on the PPFC would be exposed to undesired pressure inside the chamber, leading to cell detachment from the membrane. Secondly, at high flow rates the whole system might burst if the PDMS attaching both compartments is unable to resist the pressure. Finally, a higher and variable chamber height would lead to harder estimation of fluid dynamics inside the chamber, limiting the use of Equation 3.1.

Pressure in the chamber was relieved by positioning the media reservoir above the PPFC and stretching the perfusion ports. However, this was not enough to allow the performance of dynamic experiments. A tighter membrane attachment and a different polymer formulation with lower elastic properties might lead to an improved PPFC performance in dynamic experiments.

3.7. Advantages, limitations and future improvements

In this part of the work, a BBB dynamic *in vitro* system has been designed and characterized. The final configuration is a parallel-plate flow chamber with a double-compartment separated by a porous membrane. The manufacture protocol is simple and straightforward, with all parts composed of autoclavable materials. As opposed to other models[73,74], this system enables co-culture of two different cell types at the opposite sides of the membrane. HBMEC and HA attached successfully and reached confluent monolayers on both sides. The PPFC provides a tight seal with no fluid leaks when inserting culture media on the device and, most importantly, with no cross-contamination when seeding different cells on each compartment.

An additional benefit from this system is that immunofluorescent staining can be performed on the system and the membrane can be removed and imaged. This allows evaluating cell seeding efficiency and morphological analysis after use, which cannot be done in some of previously published models.[72] One of the future improvements of the PPFC will be to obtain bright surfaces with no roughness after polymerization, in order to enable *in situ* cell visualization during experiments. Moreover, the dimensions of the compartments allow the presence of a high cell number in the system, which can yield high concentrations for post-process techniques such as Western blot or RT-PCR. Such techniques require sufficient volume of highly concentrated protein or mRNA in order to analyze protein or gene expression. Dynamic models have a tendency to minimize the culture area, limiting the performance of such techniques.[73,75,194]

The PPFC maintained HBMEC adhered on the PPFC for 48 hours at shear stress of 5 dyn/cm^2 or lower. However, increased flow resulted in cell detachment and PDMS swelling due to overpressure inside the chamber. The lack of tightness of the attached membrane obstructed the outlet port, limiting fluid evacuation. A more rigid polymeric formulation needs to be tested on the chamber with a better system to keep the membrane on its natural position. With the afore-mentioned improvements, it is expected that the PPFC will be able to operate under dynamic conditions.

While, HBMEC grown on the PPFC displayed endothelial morphology and expressed tight junction marker ZO-1, no other barrier phenotype evaluations could be performed within the duration of this thesis. After correction of the PPFC dynamic performance, permeability assays will be performed. Also, incorporation of electrode wire insertion ports will allow live TEER monitoring as an additional barrier formation parameter.[71,72]

Overall, the designed PPFC is able to reproduce endothelial-astrocyte co-cultures and allows successful post-experimental cell visualization and cellular extraction. Shear stress exposure in

this model will allow the evaluation of the dual effect of HA and flow on BBB phenotype in both physiological and pathological conditions. The physical presence and the direct contact of astrocytic feet with the abluminal side of HBMEC instead of astrocyte-conditioned medium may add to the effect of hemodynamic alterations at the BBB. Also, the membrane of use can be adapted to the design of experiments. Study of dynamic effects on the BBB in disease will also be possible by adaptation of pore size in membranes. For instance, leukocyte migration or amyloid-β permeability assays, key components in the study of multiple sclerosis[195,196] and Alzheimer's disease[197–199], will be possible by using larger or smaller pore size membranes.

4. Study of renal artery microanatomy to maximize efficacy of renal denervation

4.1. Introduction

Catheter based renal denervation (RDN) has emerged as a non-pharmacological treatment for resistant hypertension.[156,157] A study in hypertensive rats showed that RDN might also be indirectly beneficial to the recovery of BBB behavior.[164] However, RDN efficacy was not achieved as expected in the latest Symplicity HTN-3 controlled trial.[160] While the reasons for the lack of efficacy in HTN-3 are still a matter of debate, it has been hypothesized that procedural issues limited the extent of actual nerve ablation and that this was compounded by the complexity and variability of the target anatomy.[161] Focal delivery points may not achieve maximal efficacy if lymph nodes or veins are close and high nerve regions are missed.[163] Better understanding of the microanatomical environment of renal arteries (RAs) is crucial to optimize RDN therapy to reduce hypertension, improve proper vascular activity and recover physiological conditions in peripheral entities such as the BBB, where the role of sympathetic nerves is also critical.[200,201]

The following chapter aims to study anatomical patterns in RAs using swine as an animal model with a cardiovascular anatomy that closely represents the human.[202] In Chapter 4.2, nerve distribution patterns using different geometrical parameters are analyzed along all directions of the RA; circumferential direction on a quadrant basis, axial direction at different subgroups located at different distances of the aortic ostium and radial direction as the distance from the RA lumen. Then, lymph nodes (LN) surrounding RA lumens are quantified in Chapter 4.3 following the same directional analysis. The purpose of this multidimensional analysis allowed detecting the regions of high nerve density and low lymph node coverage and therefore those of highest interest as a target for RDN treatment. Veins were not analyzed in this study because of technical limitations; histology sectioning induced shape deformation on these. Finally, RDN ablation coverage is evaluated in Chapter 4.4 under different patterns of energy delivery. Affected nerves and LN presence in ablated areas are quantified.

Figure 4.1 illustrates the counter-clockwise quadrant nomenclature followed along the Chapter based on the orientation of histological RA sections, the latter coming from tissue trimmed at different distances of the RA ostium (~0, ~3, ~6, ~9, ~12, ~15 and ~21 mm).

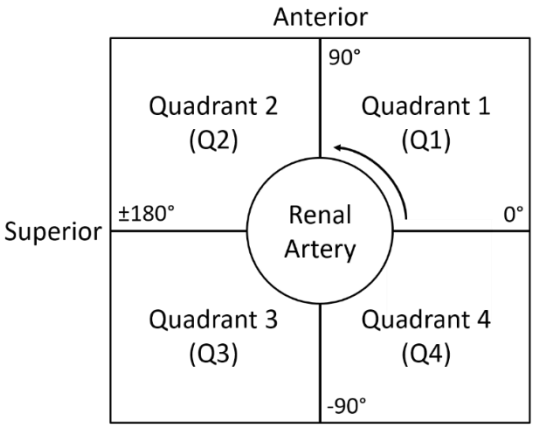

Figure 4.1. Orientation and nomenclature followed in histological renal artery sections.

4.2. Nerve distribution in renal arteries

4.2.1. Nerve distribution in circumferential quadrants

All nerves detected and analyzed in the histological section data set were represented in a composite normalized map, independently of their distance to the ostium (Figure 4.2).

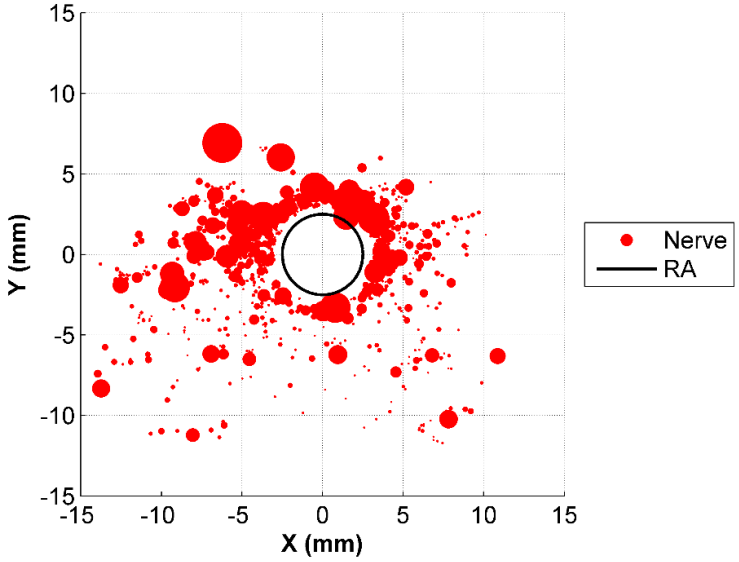

Figure 4.2. Composite overlay map of nerves around renal arteries in all histological sections analyzed.

Figure 4.2 shows that nerves were present all around the RA. Visually, the anterior quadrants appeared to contain a higher population of nerves, compared to the posterior quadrants. Moreover, the density in anterior quadrants is higher at small distances from the lumen, while posterior quadrants are less dense and with nerves more spread deep in the tissue.

The average number of nerves per quadrant and artery was calculated overall (Q) and in each specific sector (Q1 to Q4) (Figure 4.3).

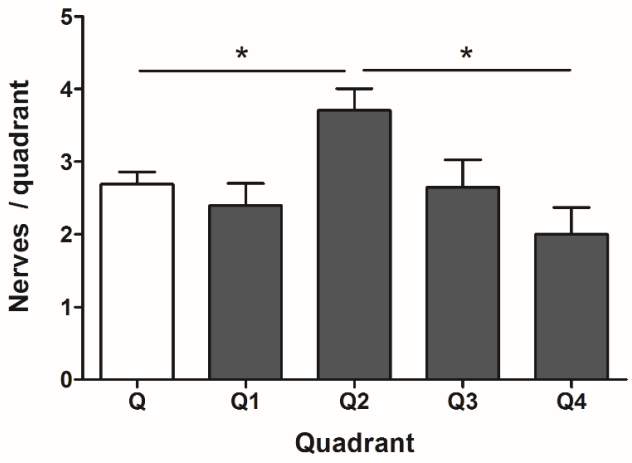

Figure 4.3. Quadrant nerve density in renal arteries.

The average number of nerves in any quadrant was 2.7±0.2. The superior-anterior quadrant (Q2) was the region containing the highest density of nerves (3.7±0.3/section), which was significantly higher than the general average. The opposite side of the RA, the inferior-posterior quadrant (Q4) was the area containing the lowest amount of nerves (2.0±0.4/section). While not significant compared to the general average, the difference between opposite quadrants Q2 and Q4 was significant, suggesting that RDN therapy is more likely to succeed if the superior-anterior quadrant is targeted.

4.2.2. Nerve distribution at different renal artery axial locations

The average number of nerves per section was calculated overall and in each subset of sections corresponding to different distances from the aortic ostium (Figure 4.4). The average number of nerves per section was 10.7±0.7, independently of the distance. While no statistical significance was found, the average number of nerves per section decreased from the aortic ostium, with an above-average density of 12.3±1.6 nerves/section, towards a low nerve density region between 3 and 12 mm, with the lowest density (6.7±1.2/section) at 6 mm. Then, nerve density increased at the farther regions reaching a maximal density of 13.7±2.5 at 21 mm.

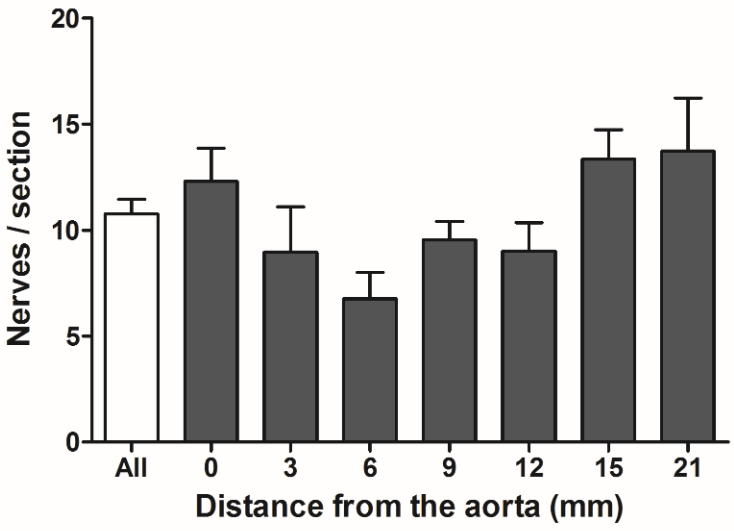

Figure 4.4. Nerve density at different locations of renal arteries.

4.2.3. Nerve distribution per quadrant at different renal artery locations

All nerves detected and analyzed in each subgroup of ostium distant sections were individually represented in normalized maps (Figure 4.5).

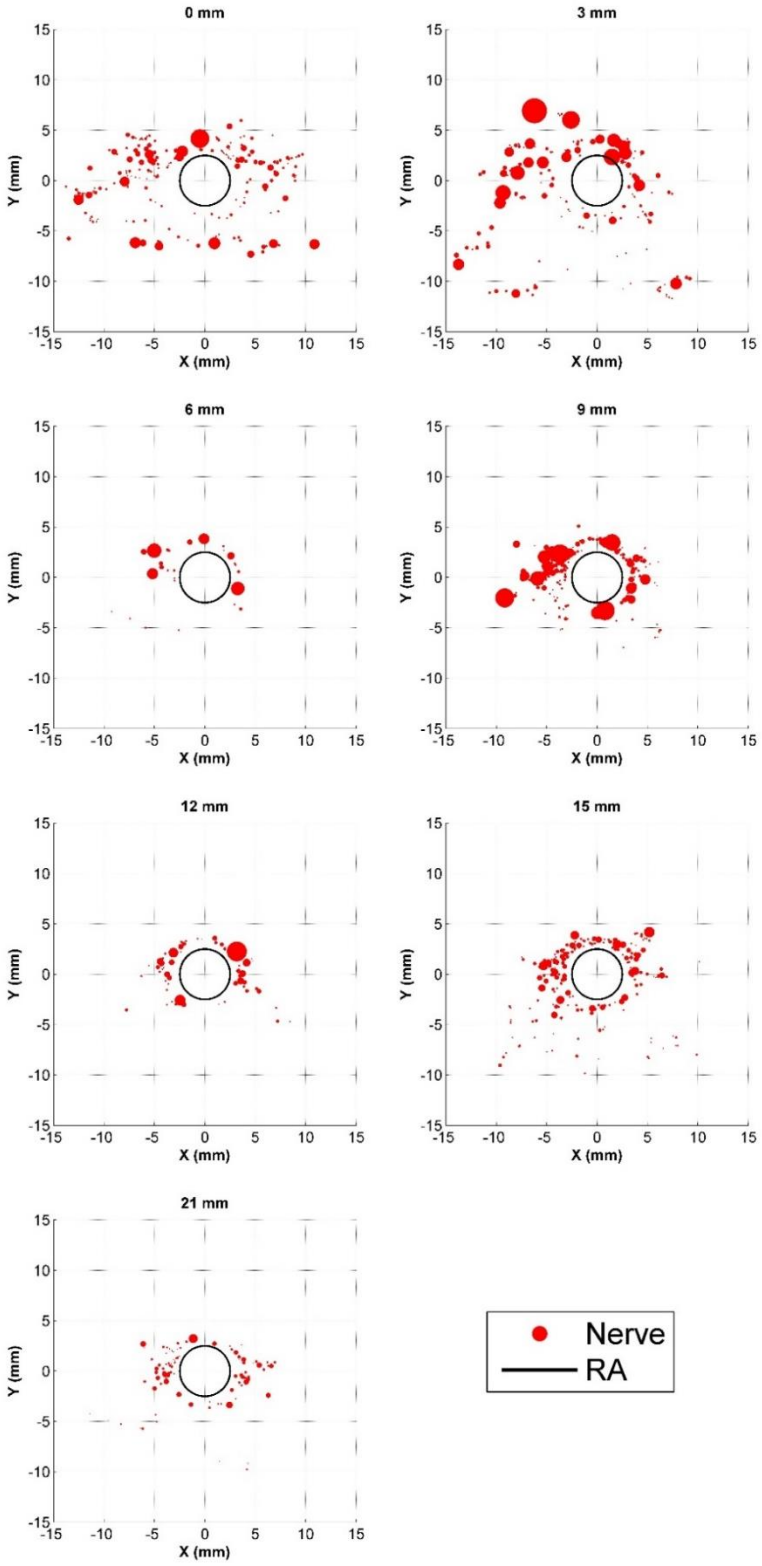

Figure 4.5. Composite overlay maps of nerves around renal arteries at different distances from the aortic ostium.

The finding that on average, nerves in anterior quadrants were more abundant carried through to individual representations of each RA sector. Generally, quadrants Q1 and Q2 were more populated with nerves of higher diameter (Figure 4.5). However, lower nerve densities compared to Figure 4.2 and variability in the sample number per group (ranging from 7 to 17) limited the quadrant contrast between RA locations. Figure 4.6 provides a quantified version of Figure 4.5, where the average number of nerves per quadrant and axial distance is shown.

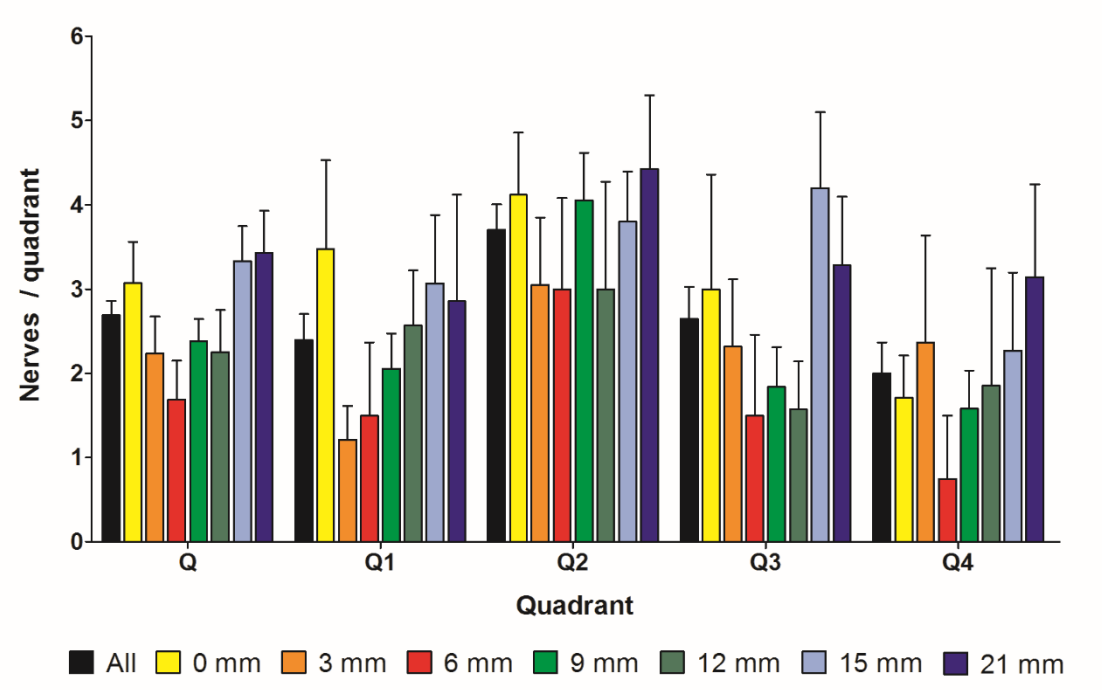

Figure 4.6. Quadrant nerve density at different locations of renal arteries.

The superior-anterior quadrant Q2 was the predominant nerve containing region with all RA blocks containing more than 3.0 nerves/section (Figure 4.7). Also, quadrant Q2 is the least variable among all quadrants, with a difference of 1.4±1.9 nerves/section between the more and least abundant regions.

Figure 4.7. Representative section of predominant nerve abundance in superior anterior quadrant (Q2) of a renal artery (black: renal artery; red: nerve).

By contrast, the inferior-posterior quadrant is the most variable quadrant, with a difference of 2.4±1.8 nerves/section. Overall, all quadrants display the same pattern described in the circumferential nerve abundance in Figure 4.4. With increasing distance from the ostium, average nerve abundance first decreases down to a minimal density at a distance of 3 – 6 mm, and then increases reaching maximal abundances at distances of 15 – 21 mm (Figure 4.8).

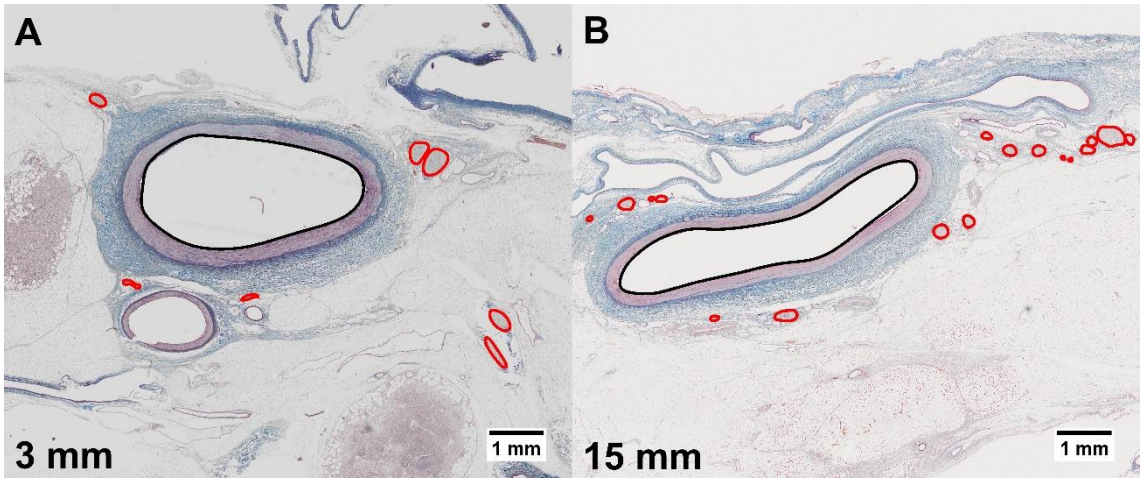

Figure 4.8. Representative sections of low and high nerve abundance in renal arteries at 3 mm (A) and 15 mm (B) of the aortic ostium (black: renal artery; red: nerve).

While no statistical significance was found, the fact that the same pattern is observed in all quadrants suggests that there might be a common circumferential distribution of nerves reaching the renal artery towards the kidneys.

4.2.4. Radial nerve distribution

Radiofrequency catheter-based RDN treatment originates in the RA lumen and spreads into the tissue. Nerves surrounding the RA lumen are more susceptible to be targeted than distant nerves. When radial distribution along RAs was observed in Figure 4.5, two distribution areas were detected. On one hand, nerves at the aortic ostium and at 3 mm were more spread and distant, with a higher number of nerves far from the lumen. On the other hand, nerves in all regions beyond 3mm were closer to the wall. Moreover, bigger size nerves were generally located closer to the lumen than smaller ones. Cumulative radial nerve distributions were quantified using both nerve frequency and area in order to evaluate not only distributions but also any potential difference between number frequency and area radial presence. Results are shown in Figure 4.9 and Figure 4.10, respectively.

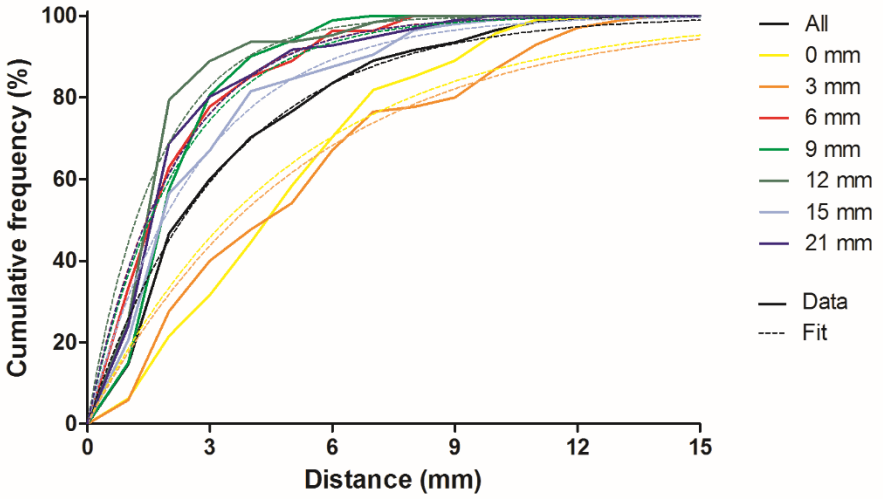

Figure 4.9. Cumulative radial distribution based on nerve frequency.

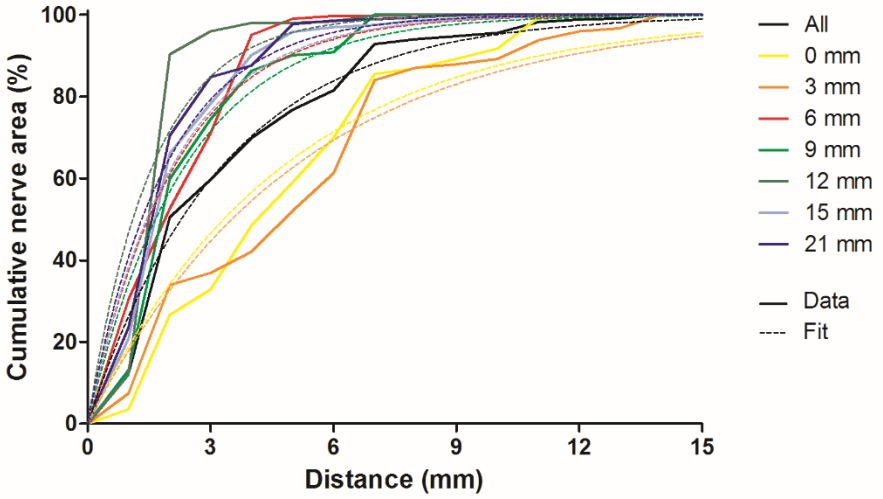

Figure 4.10. Cumulative radial distribution based on nerve area.

The same pattern was found in both cumulative nerve frequency and area distributions. Regardless of the group, distributions increased gradually with radial distance, following an inverse exponential growth tendency (Equation 4.1). At 0 and 3 mm away from the ostium, a higher nerve percentage was found at longer distances from the lumen, with the farthest nerve located at 13.6 mm. Cumulative frequencies in those two blocks were lower than the overall trend (black lines in Figure 4.9 and Figure 4.10). Beyond 3 mm, nerve accumulation was faster, with all nerves present below 10 mm of the RA wall.

$$\%_{\text{cumulative}} = 1 - e^{-k \cdot \text{radial distance}} \qquad \textbf{Equation 4.1}$$

Coefficient k in Equation 4.1 was fit by the least squares method in all curves, with all coefficients of determination (R^2) above 0.85 (Table 4.1). Curve fitting allowed the evaluation of the radial distance including 80 % of nerves, based on number and area (Table 4.2).

Table 4.1. Curve fitting parameters of cumulative radial distributions.

	Frequency		Area	
Distance (mm)	k	R^2	k	R^2
All	0.30	0.99	0.30	0.98
0	0.20	0.93	0.21	0.94
3	0.19	0.97	0.20	0.95
6	0.48	1.00	0.47	0.97
9	0.45	0.95	0.42	0.96
12	0.58	0.96	0.63	0.85
15	0.37	0.99	0.48	0.97
21	0.47	0.98	0.52	0.97

Table 4.2. Radial distances containing 80% of nerves.

	Radial distance (mm)	
Distance (mm)	Frequency	Area
All	5.3	5.4
0	7.7	7.9
3	8.2	8.4
6	3.4	3.4
9	3.8	3.5
12	2.6	2.8
15	3.3	4.3
21	3.1	3.4

As seen in Table 4.2, 80% of nerves are found below 5.4 mm away from the RA lumen. In the region closest to the aorta (3 mm or less), the same distance is of 7.9 and 8.1 mm, based on nerve frequency and area, respectively. Such distances were 2.5 and 2.3-fold higher than those in RA regions beyond 3 mm. Both frequency and area radial distributions showed equivalent results with no significant difference between them.

4.2.5. Optimal renal artery target to maximize nerve ablation

Morphometric nerve distribution around RAs was evaluated in a multi-dimensional manner by analysis of nerves in the circumferential (quadrant), axial (distance to the aortic ostium) and radial (distance to the wall) directions. Table 4.3 compiles the regions with highest and lowest nerve population based on the above-mentioned directions.

Table 4.3. Regions along the renal artery with maximal and minimal nerve abundance on multiple dimensions.

Direction	High nerve density	Low nerve density
Quadrant (Circumferential)	Superior-anterior quadrant (Q2)	Inferior-posterior quadrant (Q4)
Distance to the aortic ostium (Axial)	15 - 21 mm	3 - 6 mm
Distance to the lumen wall (Radial)	>3 mm	0 - 3 mm

Optimal RDN treatments are located at distal regions from the RA bifurcation, where a higher and more concentrated nerve population was found at distances below 4 mm from the lumen.

4.3. Lymph node distribution in renal arteries

The interest in lymph node (LN) distribution is motivated by suggestions that their presence has an effect on the distribution of RDN electric potential[163] and to evaluate if their distribution affects the distribution of nerves. LN distribution was quantified along the same three directions followed in Chapter 4.2 in order to detect the regions with the lowest LN abundances that would allow a more efficient treatment. In this chapter, LN were quantified relative to their area. Their frequency based on number was low; each slide commonly displayed either one to two LN or none. It was decided that an area analysis would provide better distribution results. Moreover, LN extension can reach areas beyond RDN ablation areas, where the distribution analysis would be of no use. For that reason, the analysis was limited radially. All areas were measured inside a 5 mm ring from the RA lumen.

4.3.1. Lymph node distribution in circumferential quadrants

All lymph nodes detected and analyzed in the histological section data-set were represented in a normalized map, independently of their distance to the ostium (Figure 4.11).

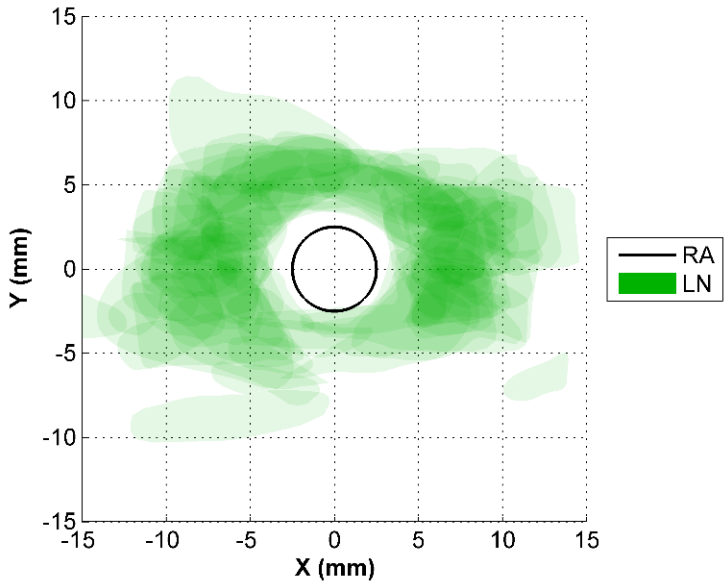

Figure 4.11. Composite overlay map of lymph nodes around renal arteries in all histological sections analyzed.

LN were present all around RAs, as seen in Figure 4.11 with a continuous green area surrounding the arterial lumen. Each lymph node was represented with a semi-transparent green area. When more than one LN is present at the same point, the green transparence is added. Therefore, the higher the green intensity, the higher the LN abundance was. The anterior quadrants (Q1 and

Q2) displayed more abundant LN presence compared to posterior quadrants (Q3 and Q4) (Figure 4.12), which had a low LN presence between -135° and -45°. Interestingly, LN were not detected close to the RA, below 1 mm approximately.

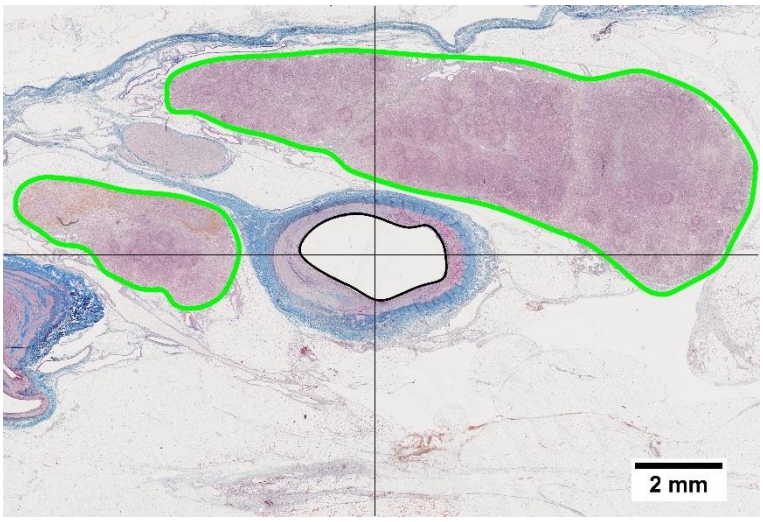

Figure 4.12. Representative section of predominant lymph node coverage in anterior quadrants of a renal artery (black: renal artery; green: lymph node).

The average percentage of LN coverage per quadrant was calculated in each specific sector (Figure 4.13).

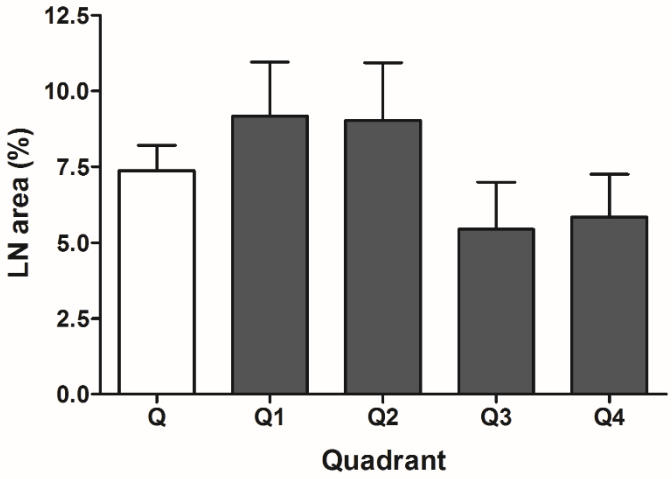

Figure 4.13. Quadrant lymph node distribution in renal arteries

As previously stated, average LN quantification showed a 1.5-fold higher LN area coverage in the anterior quadrants (9.2±1.8% and 9.0±1.9%), compared to the posterior quadrants (5.4±1.5% and 5.8±1.4%). However, the difference between Q1 and Q2 with Q3 and Q4 were not statistically significant.

4.3.2. Lymph node distribution at different renal artery axial locations

All LN detected and analyzed in each subgroup of ostium distant sections were individually represented in normalized maps (Figure 4.14).

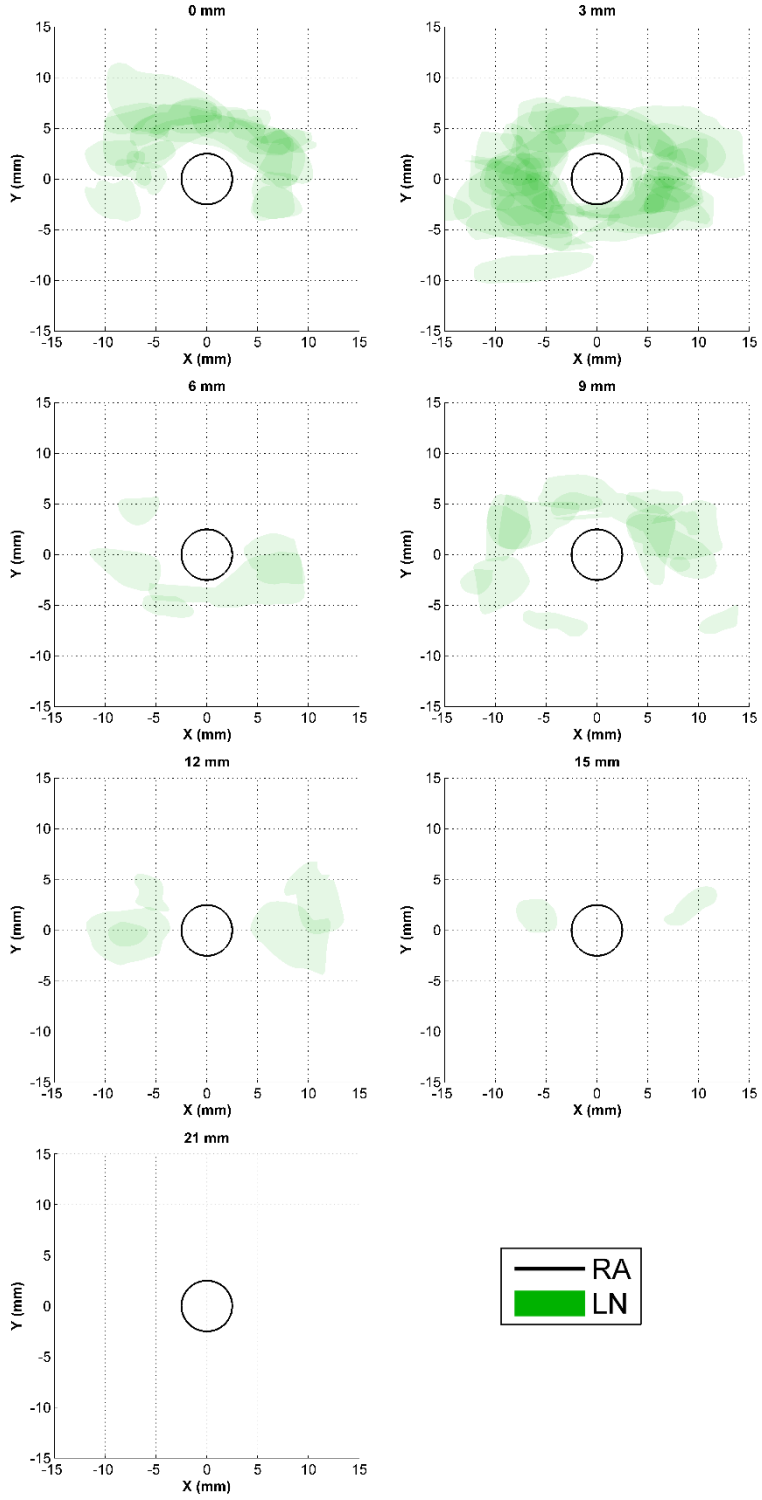

Figure 4.14. Composite overlay maps of lymph nodes around renal arteries at different distances from the aortic ostium.

As opposed to the complex visual analysis of nerve density in Figure 4.5, LN coverage patterns along the axial direction of the RA were more detectable in normalized maps in Figure 4.14. Sections below 3 mm from the aortic ostium showed larger LN areas compared to farther regions.

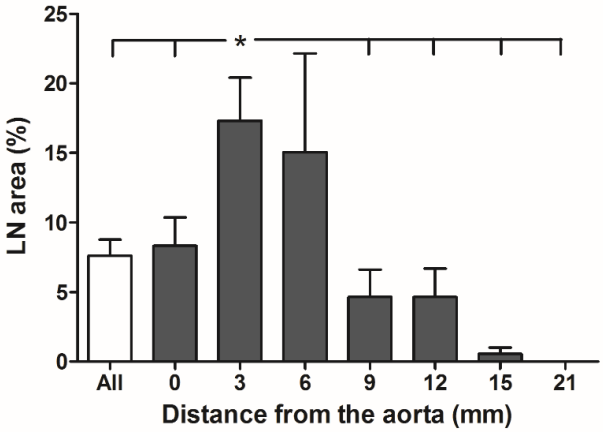

Figure 4.15. Lymph node coverage at different locations of renal arteries.

Average area quantification in all subgroups (Figure 4.15) confirmed the previous statement. LN were most abundant and covered the largest area fraction (17.3±3.1%) 3 – 6 mm from the ostium. LN area decreased significantly 9 mm from the ostium and reached very low levels by 15 and 21 mm (0.5±0.4% and 0.0±0.0%, respectively). Figure 4.16 illustrates the significant difference between maximal and minimal LN coverage locations.

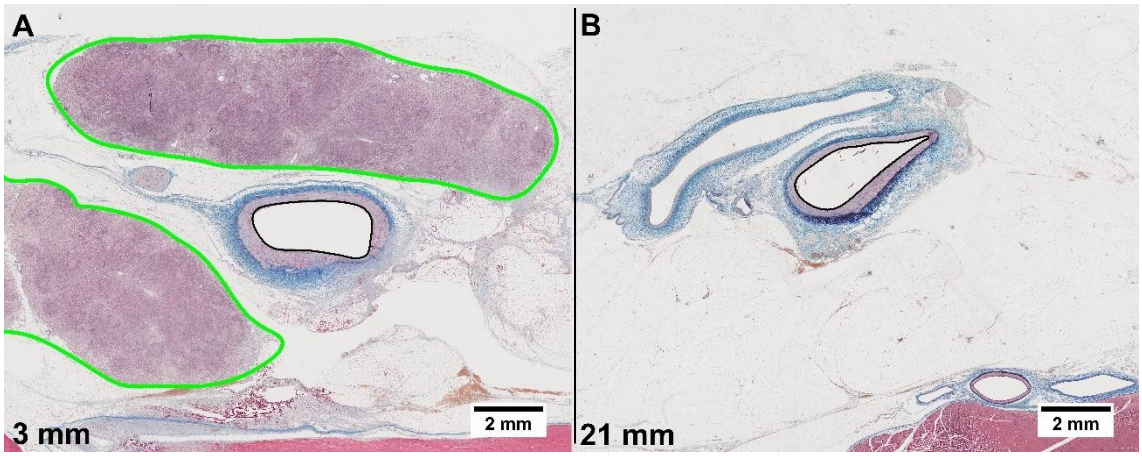

Figure 4.16. Representative sections of high and low lymph node coverage in renal arteries at 3 mm (A) and 21 mm (B) of the aortic ostium (black: renal arteries; green: lymph node).

4.3.3. Lymph node distribution per quadrant at different renal artery locations

The average LN coverage per quadrant and axial location is shown in Figure 4.17.

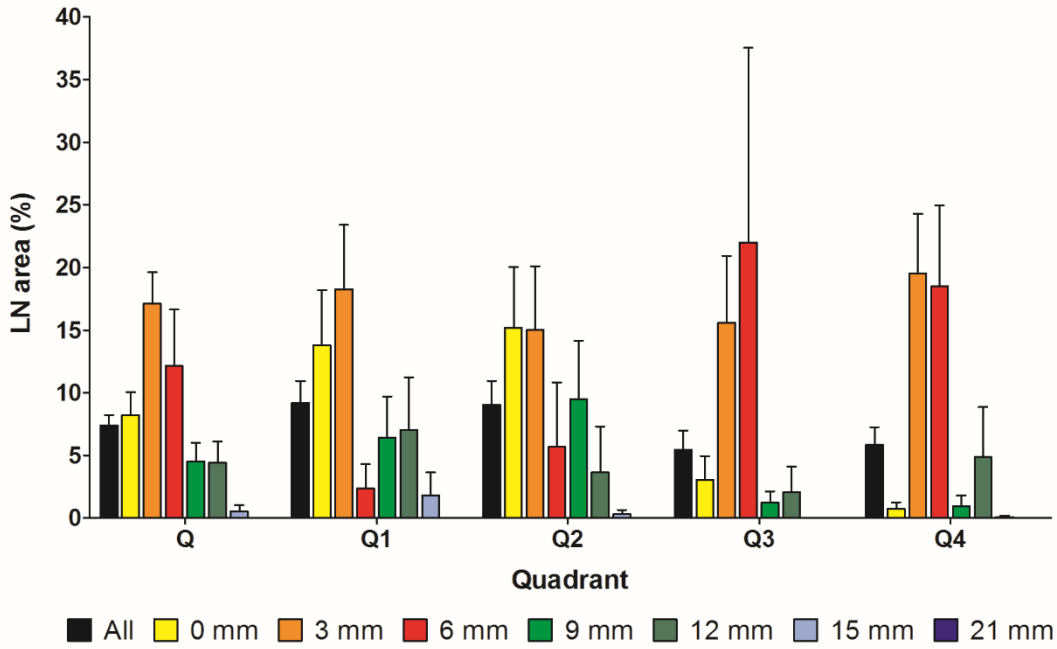

Figure 4.17. Quadrant lymph node coverage at different locations of renal arteries.

As in the overall results in Figure 4.15, individual quadrants had a higher presence of LN in regions between 0 and 6 mm from the ostium. Predominant quadrants, however, were variable in the subgroups included in that range. Anterior quadrants showed higher LN presence at 0 mm whereas LN primed in posterior quadrants at 6 mm. At 3 mm, all quadrants showed a similar area coverage. Regions farther than 6 mm showed a progressive decrease in LN area, all of them below their respective total average. While no clear pattern was found in circumferential heterogeneous distributions, results in Figure 4.17 suggest that larger distances from the ostium are an optimal target for RDN treatments, where lower LN abundance would allow a deeper spread of ablation areas. Further analysis of vein distribution will contribute to strengthen the previous statement.

4.3.4. Radial lymph node distribution

LN area coverage was evaluated from the RA wall to 5 mm away from the lumen. Two subgroups were defined in that distance, separated at 2.5 mm. LN presence around RAs was evaluated in both subgroups and represented in Figure 4.18. Results showed a significantly lower LN presence from 0 to 2.5 mm of the RA (4.2±0.9%), compared to the 2.5 – 5 mm region (9.5±1.3%).

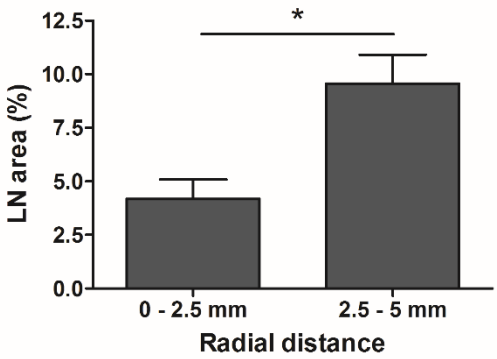

Figure 4.18. Lymph node radial coverage below 5 mm.

Given that LN coverage was significant lower below 2.5 mm and in order to detect the optimal region that also contained high nerve density, the percentage of nerves below 2.5 mm was evaluated for each axial group. Radial nerve distribution fitting curves from Table 4.1 were used to evaluate the nerve population between 0 and 2.5 mm away from the lumen (**Error! Not a valid bookmark self-reference.**).

Table 4.4. Nerve population at a radial distance below 2.5 mm based on frequency and area.

Distance to the ostium (mm)	Frequency (%)	Area (%)
All	52.6	53.2
0	39.8	40.6
3	38.0	38.9
6	69.6	69.1
9	67.9	64.9
12	76.8	79.3
15	60.5	70.0
21	69.5	73.1

RDN treatment in RA positions beyond 6 mm from the aortic ostium would not only benefit from a lower LN presence but also with more than 70% of nerve population in narrow distances, which is higher than the nerve percentage reported to have a significant effect on reduction of norepinephrine levels.[161]

4.3.5. Optimal renal artery target to reach maximal nerve ablation with minimal lymph node presence

Morphometric LN distribution around RAs was evaluated in a multi-dimensional manner by analysis of LN area coverage in the circumferential (quadrant), axial (distance to the aortic ostium) and radial (distance to the wall) directions. Table 4.5 compiles the regions with lowest and highest nerve population based on the above-mentioned directions.

Table 4.5. Regions along the renal artery with minimal and maximal lymph node presence on multiple dimensions.

Direction	Low LN presence	High LN presence
Quadrant (Circumferential)	Posterior quadrants (Q3 – Q4)	Anterior quadrants (Q1 – Q2)
Distance to the aortic ostium (Axial)	9 - 21 mm	3 - 6 mm
Distance to the lumen wall (Radial)	0 – 2.5 mm	2.5 – 5 mm

Regardless of circumferential differences, nerve density and LN presence were represented in Figure 4.19. In the different subgroups analyzed based on their distance to the ostium, the optimal distances to deploy RDN catheters are 15 and 21 mm, where nerve density is maximal and LN density is minimal.

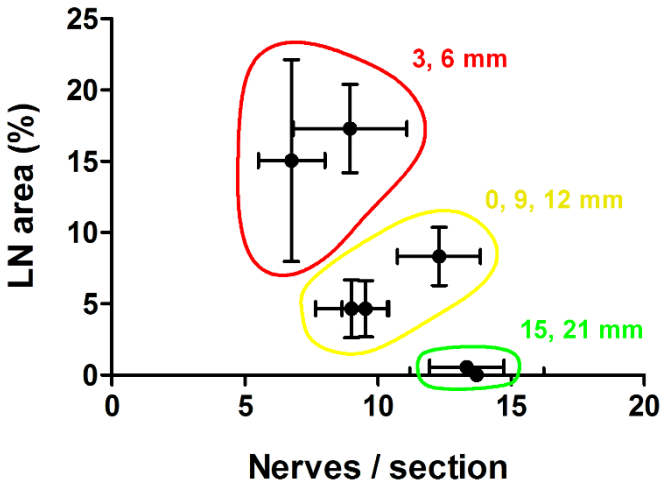

Figure 4.19. Average nerve density and lymph node area in axial groups studied.

4.4. Ablation efficacy on single and dual renal denervation treatments

While it is critical to understand RA microanatomy by detecting regions with high nerve density and low LN coverage, it is of equal importance to deliver RDN treatment efficiently. Current designs of RDN electrode catheters operate by delivering radiofrequency or ultrasound energy at RA wall contact points of the electrode. Energy spreads from there and, as a consequence, ablation depth and efficacy is very dependent on nerves and lymph nodes present at those specific focal points. Norepinephrine (NEPI) levels may be significantly reduced by an extended area affecting a higher nerve percentage.[163] Furthermore, previous studies have shown that nerve ablation at different RA axial locations may have an additive effect on NEPI levels.[161] While histological sections are analyzed in two dimensions, ablation energy is spread three-dimensionally from the contact points. In order to maximize overall circumferential ablation efficacy, a dual RDN treatment was evaluated as a novel protocol to increase ablation depth. While in single treatments the electrodes are kept intact the whole duration of the energy delivery, dual treatment divides time in two treatments with a 180° electrode circumferential rotation between them.

4.4.1. Pilot evaluation of single/dual ablation penetration patterns with catheter 1

Single and dual treatments were tested in two different animals and sections were extracted from RAs at different distances from the aortic ostium. Initial histological visualization showed examples of increase in ablation depth and area coverage (Figure 4.20). Dual treatment locations are visible in Figure 4.20.B, where double ablation spread and combined, resulting in an increased circumferential extent compared to the single treatment in Figure 4.20.A.

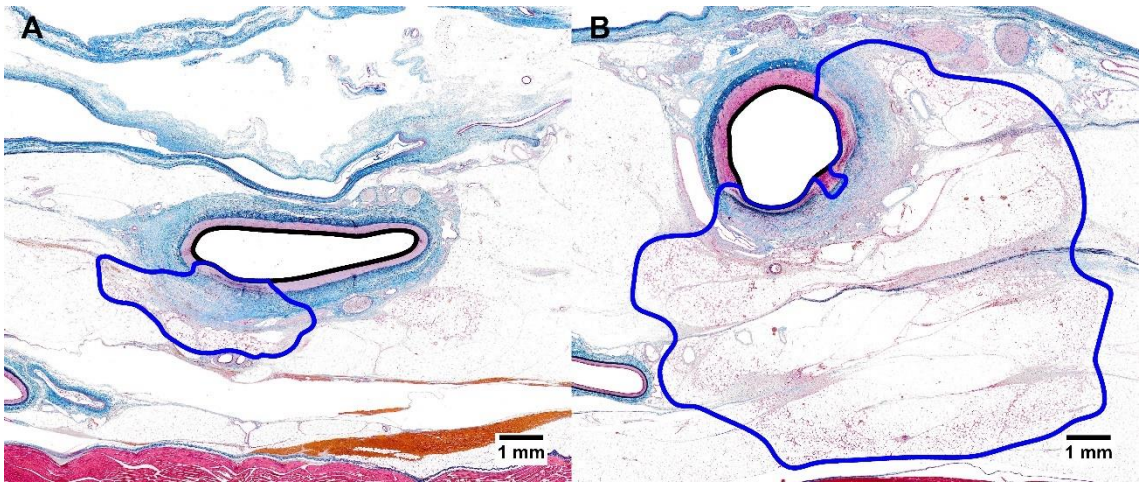

Figure 4.20. Ablation circumferential coverage and depth increase from single (A) to dual (B) renal denervation treatment at 15 mm from the aorta (black: renal artery; blue: ablation area).

In order to evaluate additive circumferential extent between both treatments, histological sections from different RA locations were analyzed and ablation areas were represented in normalized maps (Figure 4.21). While average ablation depth and area coverage per section were not significantly different between both treatments (Table 4.6), overlaid maps in Figure 4.21 showed a deeper additive ablation depth and area, with a 2.4-fold increase in circumferential luminal ablation.

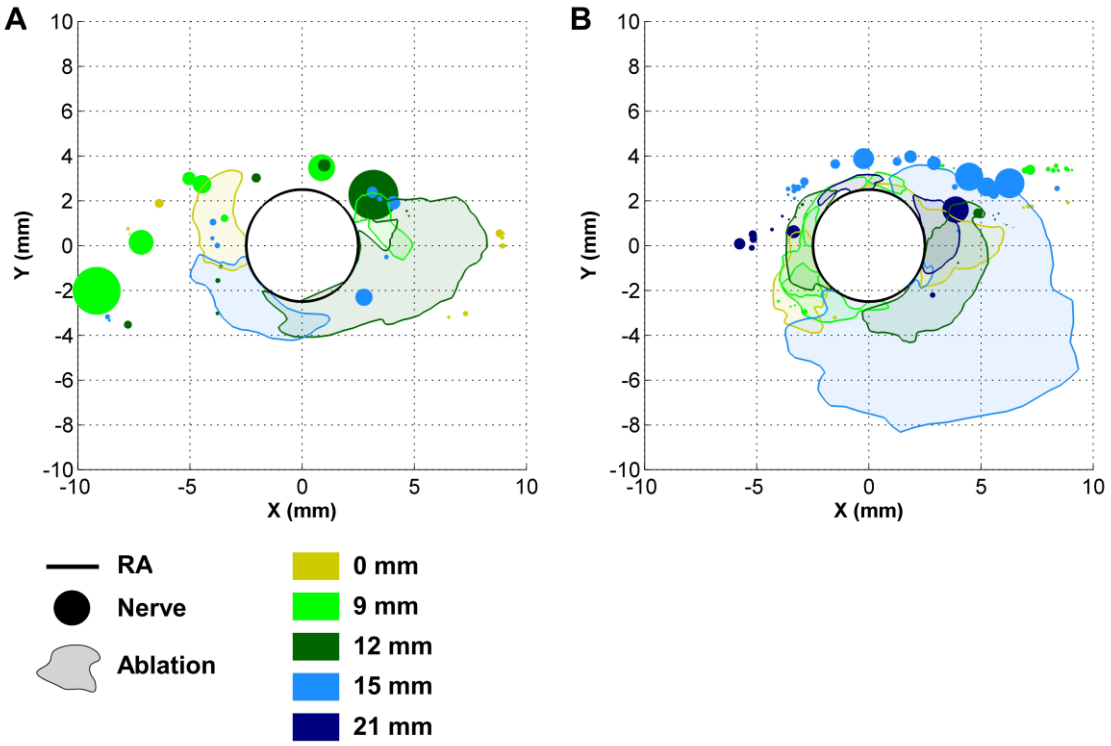

Figure 4.21. Composite normalized 5-electrode treatment maps of single (A) or dual (B) treatments with equal power and duration. (Color code: axial distance from the aortic ostium).

Table 4.6. Renal denervation ablation extent parameters in pilot comparison between single and dual treatments.

	Single	Dual
Depth (mm)	3.2 ± 0.9	3.3 ± 1.1
Area (mm^2)	7.7 ± 3.0	16.6 ± 10.8
Circumferential coverage	151.6°	360°

Previous results showed that dual treatment had potential to provide a higher circumferential extent.

4.4.2. Ablation circumferential coverage in single and dual renal denervation treatments with catheter 2

In this second study using catheter 2, two animals underwent single treatment and three animals underwent dual treatment. The same depth and area coverage metrics were measured (Table 4.7), showing no statistical difference between them. The duration of separate treatments in dual treated animals was half of the single treatment group. Maximal depth and area coverage were possibly limited by this lower duration, as each treatment spread at different focal points in the RA wall.

Table 4.7. Ablation extent parameters are equivalent in single and dual treatments.

	Single	Dual
Depth (mm)	4.4 ± 1.0	3.6 ± 0.3
Area (mm^2)	16.8 ± 4.1	16.5 ± 2.0

The main interest in this study was to measure the additive circumferential coverage of single and dually treated arteries. As seen in Figure 4.20, affected lumen perimeter was higher in the second case. Here, histological sections showed that single treatments displayed low affected lumen while some dual treatment sections even showed total affected lumen perimeter (Figure 4.22).

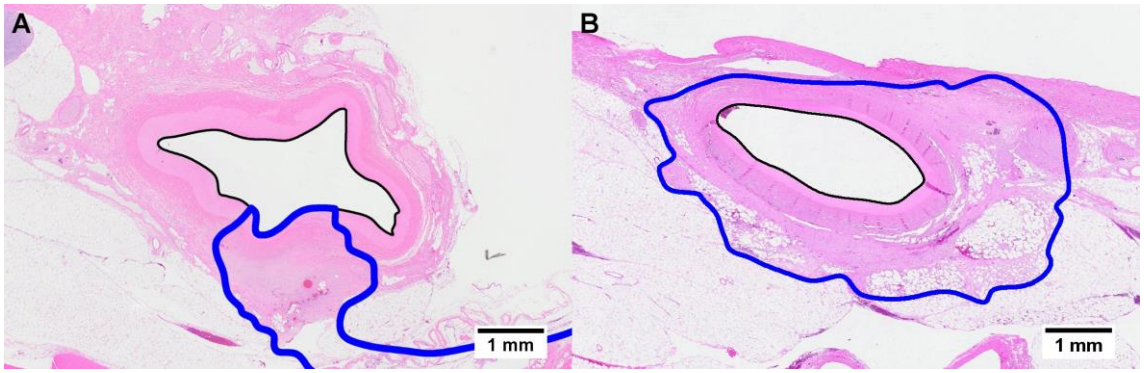

Figure 4.22. Representative image of RA sections treated with single (A) and dual (B) treatment, the latter with all lumen perimeter affected by RDN treatment (black: RA; blue: ablation area).

Additive circumferential extent was evaluated at the arterial lumen and at radial distances between 0 and 5 mm from the RA. For each subgroup, the whole circumference was divided in 10° intervals resulting in 37 angularly equidistant points. At each radial distant, a point was considered affected if it was included in an ablation area in at least one section from that artery. Average affected circumferential arc is represented in Figure 4.23.

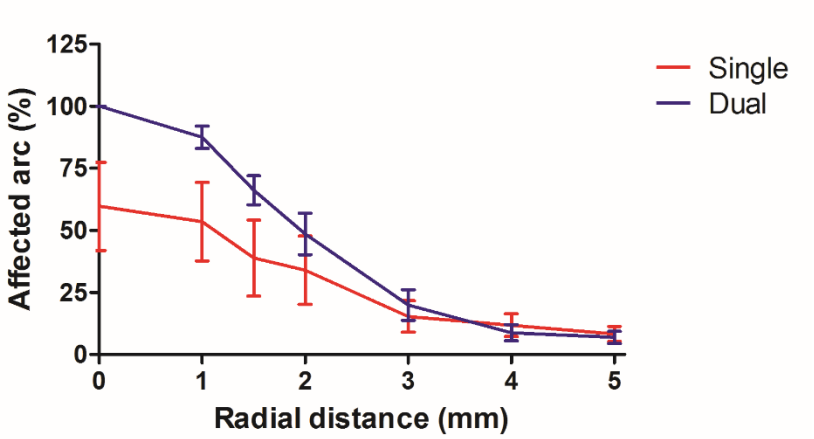

Figure 4.23. Circumferential arc affected by RDN single and dual treatments.

Summation of ablation effects over multiple tissue sections revealed that a larger percentage of the total circumferential arc was affected by dual treatments compared to single treatments up to 3 mm from the lumen. The difference between single and dual treatments was particularly pronounced up to 1 mm away from the lumen (87.5±4.6% and 53.5±15.8% in dual and single treatments, respectively). Beyond 3 mm, both treatments displayed low affected arcs below 20%. Results from Table 4.4 showed that radial distances below 2.5 mm displayed low LN presence and around 70% of nerves in distal regions beyond 6 mm from the aorta. Dual treatment provided a more effective circumferential ablation which would be translated into a higher effective ablation of nerves closely surrounding RA, independently of their angular position.

4.5. Discussion

Catheter-based RDN is an emergent technique for the treatment of resistant hypertension by reducing sympathetic nerve activity, known to have a significant role in hypertension development.[149,203] Initial European clinical trials on RDN showed promising results lowering blood pressure in patients.[156–159,204] However, a later pivotal trial in the US failed to meet the expected efficacy results.[160] While some of the causes for this lack of efficacy were attributed to uncontrolled procedural reasons, consideration was also given to heterogeneity in renal artery anatomy. From there, several studies have been published on histological renal nerve distributions in both human[205,206] and animals.[162]

Most studies on nerve distribution around RAs analyzed nerves in axial (distance to the aorta), circumferential (posterior/anterior, superior/inferior quadrants) and radial (distance to the lumen) directions. Axial distribution is typically distributed into proximal, middle and distal positions from the aorta.[161,162,205,206] As a difference in the present chapter, divisions in the axial distribution were incremented from three to seven divisions as an attempt to increase the optimal catheter position for energy delivery in the RA. Results showed that nerves were more abundant in the superior-anterior region compared to the inferior-posterior. On the axial direction, nerve density decreased from the average amount at the ostium towards a lower peak in middle regions (3 – 6 mm), reaching its maximal density at distal regions between 15 and 21 mm. Discrepancies were found in literature; while some studies showed higher nerves at proximal ostium distances[162,205], others found the distal region to be more nerve abundant.[206] The total number of nerves counted in those studies was significantly higher than this study. Higher histological sections might be required to confirm the axial results showed in this chapter. Regarding radial nerve distribution, results shown agree with literature on the statement that nerves are closer to the RA at distal positions, where more than 70% of nerves can be found within 2.5 mm of the lumen.

One of the limitations of this study is that nerves were identified from H&E and Masson's trichrome histological stains. In such scenario, sympathetic efferent nerves could not be distinguished from parasympathetic or sensory afferent nerves and therefore the distributions obtained were from all nerves independently of their type. Immunohistochemical stainings such as labeling of tyrosine hydroxylase, a specific marker for sympathetic nerves, would be a suitable option for the specific morphometry analysis of RDN target nerves.[207] A recent study, however, showed that sympathetic nerves were significantly predominant (73.5%) in human RAs, compared to parasympathetic (17.9%) and afferent nerves (8.7%).[208] As a consequence of

sympathetic nerve predominance, the results showed in this study can be extrapolated to the nerves of interest.

Despite the unavoidable interest in locating high nerve densities in RAs, it is of equivalent importance to detect other anatomical entities such as LN, skeletal muscle, fibrous sheaths or neighboring veins. A recent publication demonstrated that electrical and thermal conductivity differences between tissue types may lead to inefficient ablation spread.[163] Computational modeling showed that the close presence of LN at RDN energy delivery locations decreased the ablation depth extent. The results exposed in this chapter show for the first time the distribution of LN around RAs. Interestingly, the LN analysis supported the results observed in the nerve analysis. LN distribution on the axial direction of the RA showed a higher but not significant presence on the middle blocks (3 – 6 mm) and the lowest area coverage at the distal blocks (9 – 21 mm). Moreover, LN area was significantly higher beyond than below 2.5 mm of the lumen. Incidentally, areas richest in nerves showed the lowest LN presence. Unfortunately, no literature allowed the comparison of the results shown.

RDN ablation are commonly analyzed by different morphometry parameters, such as ablation depth, width and area.[207] A study recently reported that norepinephrine (NEPI) levels correlated with the percentage of affected nerves after RDN treatment, suggesting also that there is likely a minimal nerve percentage threshold to affect and that NEPI levels can be affected by an additive circumferential coverage of ablation areas.[161] In the comparison between single and dual treatments using catheter 2, it was shown that both treatments were able to achieve equivalent ablation areas and depths. However, dual treatments showed a higher circumferential affected arc compared to the single treatment up to 3 mm from the lumen, with the highest difference at 1 mm (Single: 53.5±15.8% – Dual: 87.5±4.6%). Ongoing research will confirm whether circumferential coverage correlates with NEPI reduction levels.[209]

Combination of the three components analyzed in this chapter suggest that RDN might be more efficient at distal regions where nerves are more abundant and closer to the aorta while LN are located farther. Additionally, most nerves were located at distance that were easily achieved in both single and dual RDN treatments performed. The dual treatment, however, showed more potential as it increased the circumferential coverage up to 3 mm from the lumen. While the study of RA microanatomy and the efficacy evaluation of single/dual treatments were performed independently, future studies will aim to achieve maximal RDN efficacy by targeting the optimal treatment areas detected in this chapter by performing single and dual treatments.

The therapeutic potential of RDN extends beyond resistant hypertension. Known to be a risk factor for several vascular-related diseases in peripheral organs[117], reduction of blood-pressure by sympathetic nerve ablation could reduce the progression of such diseases. Clinical studies are still on the way of studying the safety and efficacy of the technology for resistant hypertension, which implies that the literature on the effect of RDN on other medical conditions is still poor. A recent study, however, showed key findings on BBB phenotype recovery in hypertensive rats treated with RDN.[164] The relationship between BBB permeability and sympathetic nerve activity has been studied for decades.[200,201] Further research combining the evaluation of RDN parameters, such as RA anatomical environment, NEPI levels and ablation circumferential extent, and BBB permeability markers will help elucidate the potential of such technology for neurological BBB-related diseases.

Better understanding of the anatomical environment of renal artery is critical to optimize energy-delivery techniques and protocols for renal sympathetic nerve ablation. Renal denervation therapy has a promising future towards the treatment of resistant hypertension and its related consequences, including the recovery and functional stabilization of the Blood-Brain Barrier.

5. Materials and Methods

5.1. Parallel-plate flow chamber manufacture

The parallel-plate flow chamber (PPFC) developed was designed as a two-component device made by polymerization of polydymethylsiloxane (PDMS). In order to build the two components, Teflon molds of each compartment (Figure 5.1 and Figure 5.2) were machined using a computer numerical control (CNC) machine Fagor® 8055.

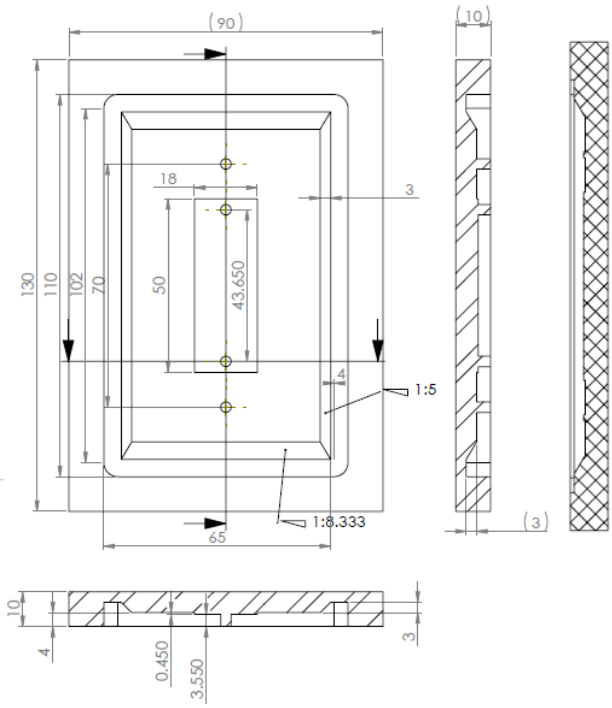

Figure 5.1. Sized drawing of the endothelial compartment negative mold (unit: mm).

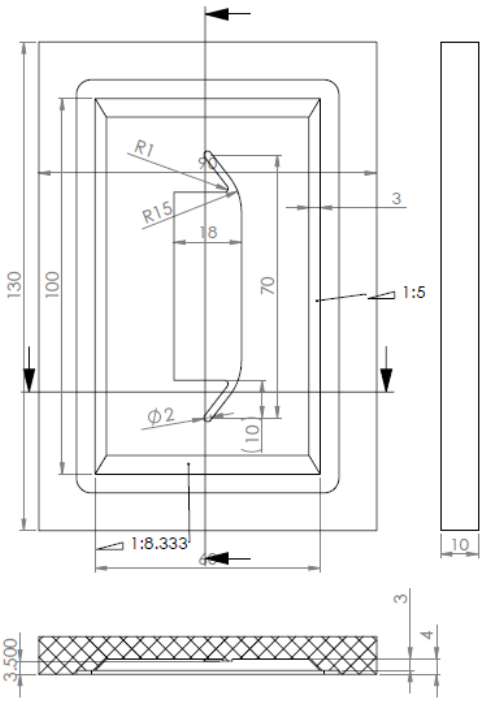

Figure 5.2. Sized drawing of the astrocytic compartment negative mold (unit: mm)

A Sylgard 184 Silicone Elastomer Kit (Dow Corning, USA) was used for PDMS polymerization. Monomer and curing agents were vigorously mixed in a 10:1 proportion and degasified in a vacuum chamber. Silicone tubing parts (3 mm ID, 2 cm long, Cole Parmer, USA) were cut and placed in the cylinders of the endothelial molds. The liquid monomer mixture was poured on the negative Teflon molds and those were then placed in a pre-heated oven at 100°C to accelerate the PDMS polymerization. After 2 hours, the molds were allowed to cool down and the polymerized parts were separated from the Teflon molds. A Teflon membrane (60 x 25 mm – 80 µm thickness – 0.4/1/5 µm pore size, Millipore, USA) was cut, placed and glued on top of the astrocytic compartment with additional liquid monomer mixture. After the membrane was fully attached, both compartments were joined with additional monomer mixture between them to avoid leaks after polymerization. Polyvinylidene fluoride (PVDF) connectors were placed on the outlet tube to allow cell seeding and connection to flow system. The final assembly was then sterilized in an autoclave.

5.2. Computational fluid dynamics

Geometries used for computational fluid dynamics (CFD) simulations were generated with computer-aided design (CAD) software CATIA®. The geometry of the parallel-plate flow chamber (PPFC) was manually drawn using basic drawing steps (Figure 5.3).

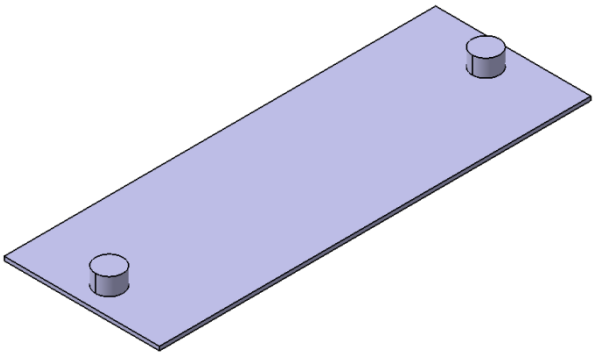

Figure 5.3. Three-dimensional geometry of the parallel-plate flow chamber.

However, the complexity of the arteriolar bifurcation tree required automatic drawing with the help of a computational platform previously implemented for automatic generation of vascular fractal networks.[172] Geometric parameters such as arteriolar diameters and segment lengths (Table 5.1) were extracted from human neuroangiographies of a healthy 53 year-old female (Figure 5.4) and introduced into the Blood-Brain Barrier Capillary Network Design interface (Figure 5.5). Execution of the script obtained automatically provided the final geometry (Figure 5.6).

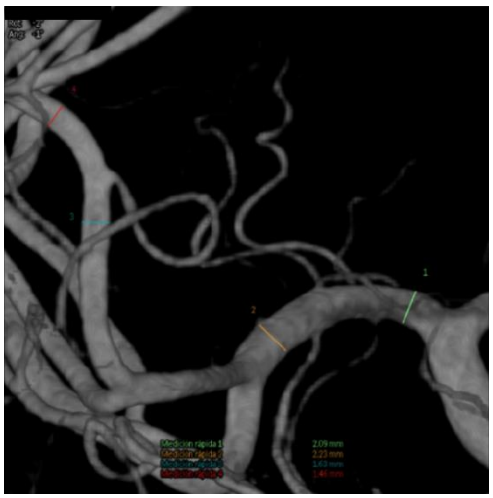

Figure 5.4. Human neuroangiography.

Table 5.1. Geometrical parameters of the vascular network model.

N	3
R (µm)	775
Ratio$_R$	0.71
ω (°)	45.00

N	L_C (µm)	L_B (µm)	α_L (°)	α_R (°)
0	19050	-	-	-
1	40280	1310	20	60
2	23580	1640	30	40
3	19550	588	30	60

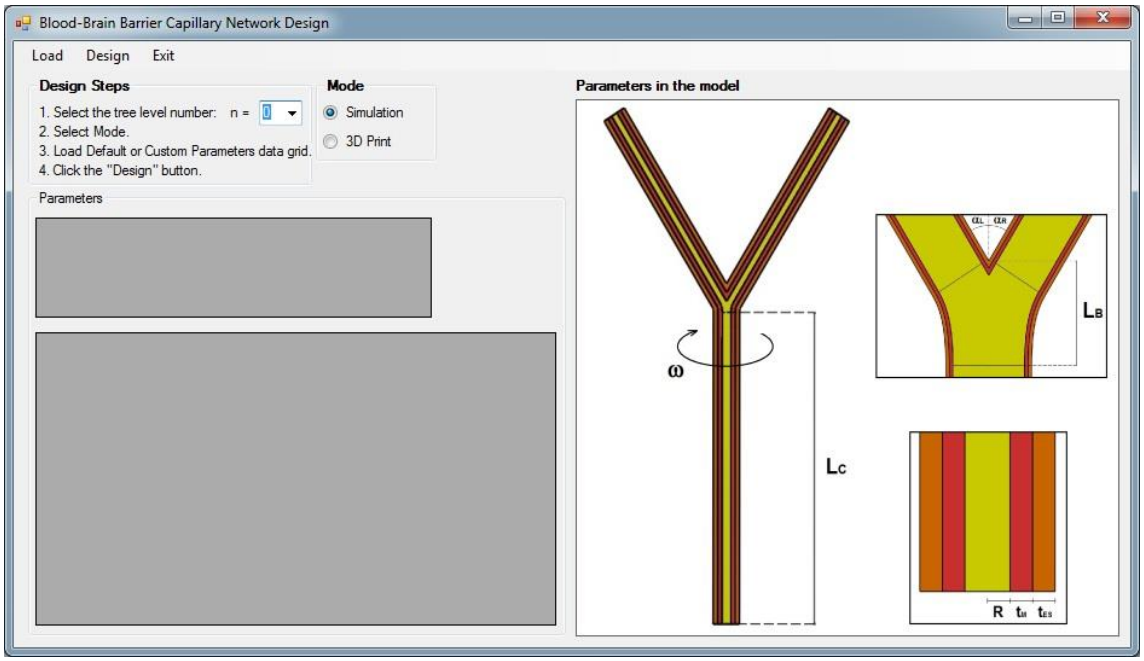

Figure 5.5. Blood-Brain Barrier Capillary Network Design user interface.

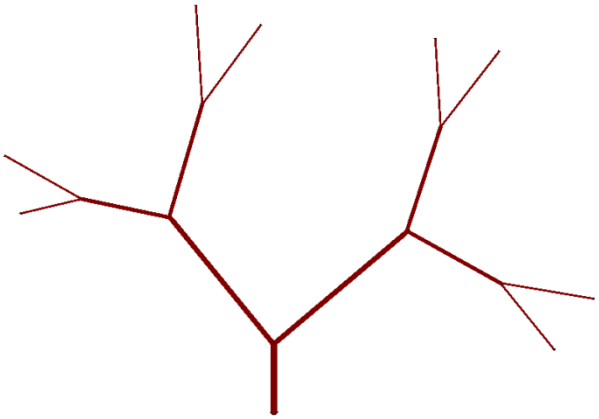

Figure 5.6. Three-dimensional geometry of the vascular fractal tree.

CAD geometries were saved as IGES files and imported in Tdyn CFD software. All simulated geometries were pre- and post- processed with GiD software, which is directly coupled to Tdyn.

A series of boundary conditions and geometry meshing parameters need to be given to all geometries before running a CFD solver.

Table 5.2 and Table 5.3 show the parameters modified in the simulations for both the PPFC and the vascular tree models, respectively, the rest were left as default. The mesh parameters were adjusted so as to find the thinnest possible mesh providing accurate results with the least computational effort. The resulting meshes are shown in Figure 5.7 and Figure 5.8.

When all simulation steps were run, visual color results and numerical data were extracted with GiD post-process tools.

Table 5.2. Tdyn parameters for parallel-plate flow chamber simulations.

GID Command	Value		
User defined problem	3D / Fluid flow		
Units	Units system	CGS	
	Geometry	mm	
Results	Velocity, Pressure, Wall Shear Stress		
Fluid Solver	Solver	Stab Bi-Conjugate Gradient	
	Tolerance	1.00E-09	
Fluid Properties	Density	1 g/cm^3	
	Viscosity	0.01 g/(cm·s)	
Fluid boundaries	Wall	Boundary type	VfixWall
		Object	All surfaces except circular inlet/outlet
	Inlet	Boundary type	Inlet VelC
		Vel Z field	-2·V·(1-(y^2+(x+21.825)^2)/1.5875^2) [cm/s]
		Object	Circular inlet
	Outlet	Boundary type	Outlet Pres
		Pressure field	0 Pa
		Object	Circular outlet
Analysis	Steady state solver		On
	Number of steps		100
Output	Output Step		10
	Output Start		1
Mesh Generation	Mesh Size		0.11
	Size Transition		0.3

Table 5.3. Tdyn parameters for vascular network simulations.

GID Command	Value		
User defined problem	3D / Fluid flow		
Units	Units system	CGS	
	Geometry	µm	
Results	Velocity, Pressure, Wall Shear Stress		
Fluid Solver	Solver	Stab Bi-Conjugate Gradient	
	Tolerance	1.00E-07	
Fluid Properties	Density	1.035 g/cm^3	
	Viscosity	0.035 g/(cm·s)	
Fluid boundaries	Wall	Boundary type	VfixWall
		Object	All surfaces except circular inlet/outlets
	Inlet	Boundary type	Inlet VelC
		Vel Z field	V [cm/s]
		Object	Circular inlets
	Outlet	Boundary type	Outlet Pres
		Pressure field	3300 Pa
		Object	Circular outlets
Analysis	Time increment		0.001 s
	Steady state solver		50
	Number of steps		15
Output	Output Step		10
	Output Start		1
Mesh Generation	Mesh Size		150
	Size Transition		0.7

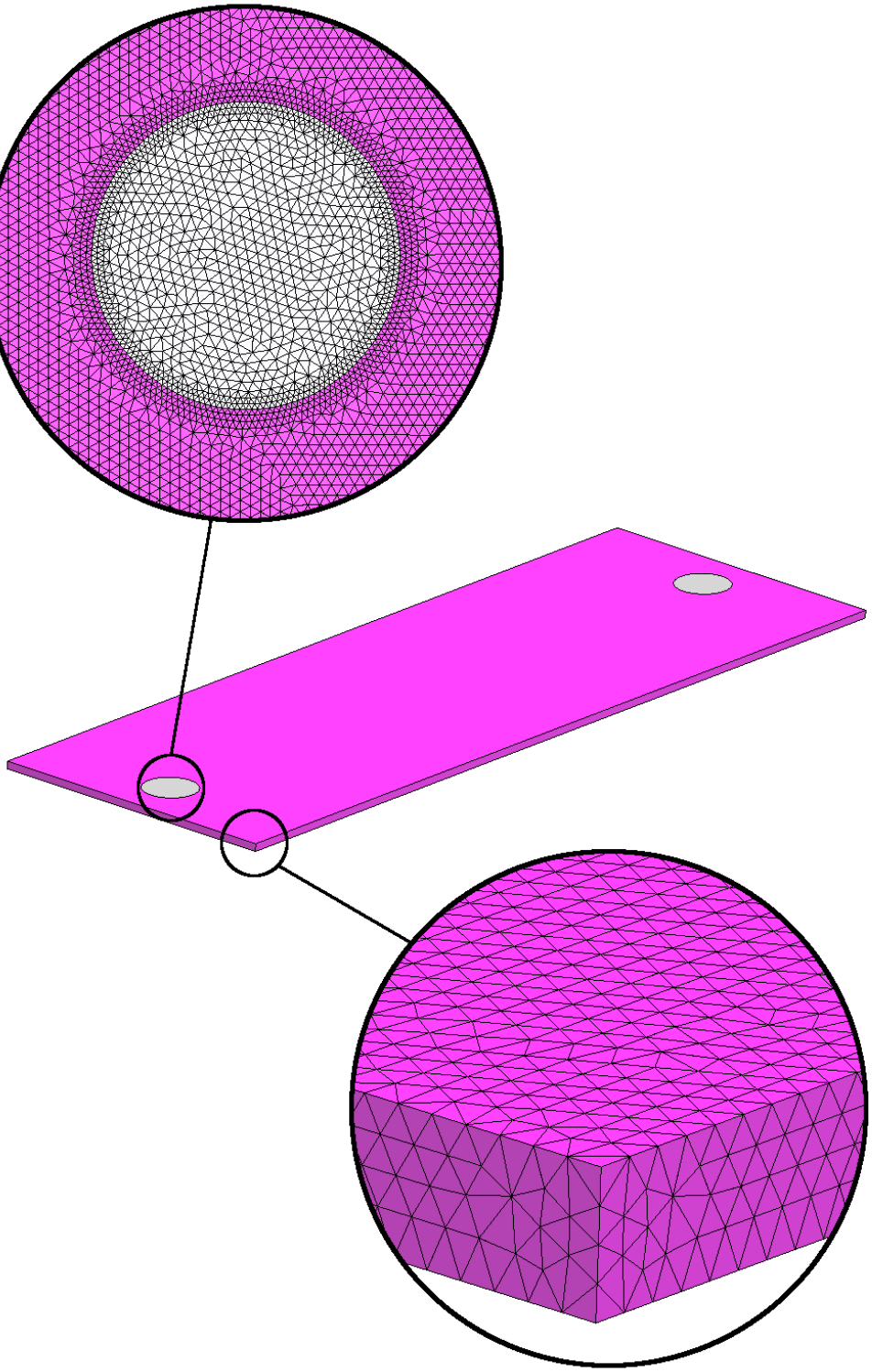

Figure 5.7. Mesh details in the three-dimensional geometry of the parallel-plate flow chamber.

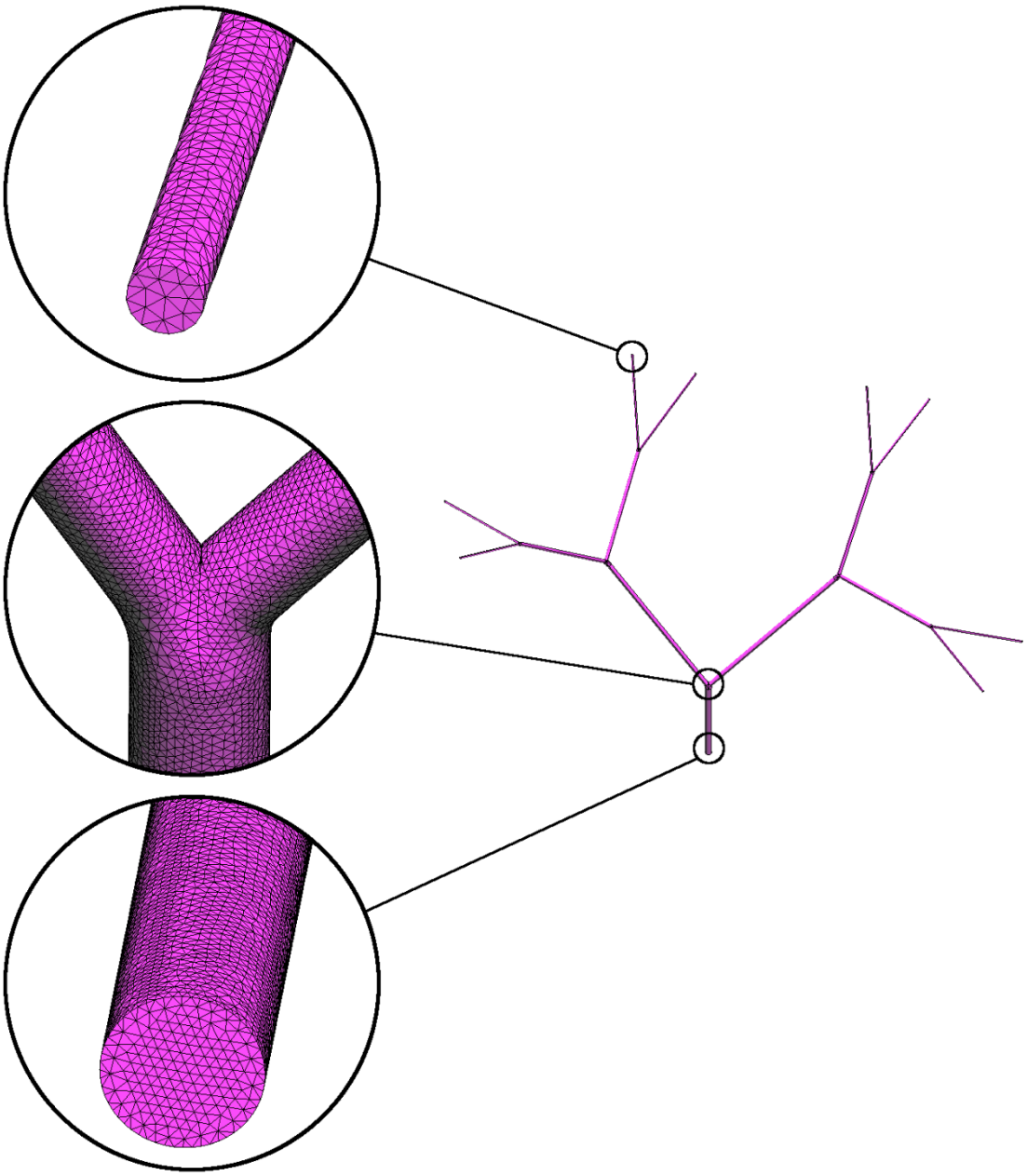

Figure 5.8. Mesh details in the three-dimensional geometry of the vascular fractal tree.

5.3. Cell culture

5.3.1. Materials and reagents

ACM: Human astrocyte Conditioned Medium, EBM-2 with secreted factors from human astrocytes.

AM: Astrocyte Medium (ScienCell, #1801, USA), supplemented with 2% FBS, 1% PS and 1% astrocyte growth supplement and sterile-filtered with a 0.22 µm filter.

Dextran: Dextran from *Leuconostoc mesenteroides* (1.5 – 2.8 MDa) (Sigma, D5376, USA).

DMEM: Dulbecco's Modified Eagle Medium with low glucose (1 g/L), 110 mg/mL sodium pyruvate (Thermo Fisher, 11054-020, USA) with 5% FBS, 1% PSG and sterile-filtered with a 0.22 µm filter.

EBM-2: Endothelial cell Basal Medium-2 (Lonza, CC-3156, USA).

EDCM: Endothelial dynamic culture medium, used for culture of HBMEC in dynamic conditions and prepared with EGM-2 and ACM in a 1:1 ratio.

EGM-2: Endothelial cell Basal Medium-2 bulletkit (Lonza, CC-3162, USA) supplemented with 5% FBS, 1% PS, bFGF 10 ng/mL, ascorbic acid 1 µg/mL, and hydrocortisone 1 µg/mL and sterile-filtered with a 0.22 µm filter.

FBS: Fetal Bovine Serum (Thermo Fisher, 26140-079, USA).

Fn: Fibronectin, bovine, stabilized solution (Alfa Aesar, J65696, USA).

HA: Human astrocytes, cryopreserved cells (ScienCell, #1800, USA).

HBMEC: Human brain microvascular endothelial cells, cryopreserved cells (Cell Systems, ACBRI 376, USA).

PLL: Poly-L-lysine solution (Sigma, P4707, USA).

PS: Penicillin 10,000 units/mL penicillin G sodium with streptomycin 10 mg/mL streptomycin sulfate in 0.85% NaCl (Thermo Fisher, 15140-122, USA).

PSG: PS with L-glutamine 200mM, 29.2 mg/mL in 0.85% NaCl (Thermo Fisher, 25030-081, USA).

Trypsin: 0.05% Trypsin in 0.53 mM EDTA (Thermo Fisher, 25300-054, USA).

5.3.2. Equipment

Cell Counter: Cellometer Auto X4 Cell Counter (Nexcelom Bioscience, USA).

Centrifuge:Eppendorf 5702 (Eppendorf, USA), Max. Speed 3000 xg (4400 rpm).

FM: Fluorescence Microscope, Nikon Eclipse Ti epifluorescence microscope (Nikon, USA) coupled to Hamamatsu CA 4742-95 camera (Hamamatsu Corporation, USA).

OM: Optical Microscope, Nikon Diaphot inverted tissue culture microscope (Nikon, USA).

5.3.3. Cell culture on plates

Cryopreserved human brain microvascular endothelial cells (HBMEC) and human astrocytes (HA) were thawed, seeded, grown and passaged onto 150 mm tissue culture polystyrene plates (TCP150, Corning, USA) as follows. The same procedure was followed for each cell type. 15 mL of previously warmed EGM-2 or AM, for HBMEC and HA, respectively, were poured into a TCP150. Then, a 2 mL cryovial containing about 10^6 cells was thawed in a water bath at 37°C for less than 2 minutes and poured in the TCP 150. The TCP150 was placed in the incubator at 37°C, 5% CO_2 and 80% humidity. After 3-5 hours, cell attachment was visually confirmed under the optical microscope and culture medium was replaced with 15 mL of fresh medium. Every 2-3 days, culture medium was replaced with 15 mL of fresh medium and cells' health was visually checked under the optical microscope. Culture plates were kept in humidified CO_2 incubator while not being manipulated. Once the cell surface coverage reached 95% of the plate, cells were split in a ratio 1:3 to continue culture. Supernatant was removed and cells were rinsed with 15 mL PBS. After aspirating off PBS, 5 mL of trypsin were poured on the cells and incubated during 5 minutes. Then, trypsin was neutralized by addition of 10mL of DMEM. The content of the plate was transferred into a 50 mL Falcon® tube and the plate was rinsed with additional 5 mL of DMEM, transferring again the content of the plate into the same tube. The cell suspension was centrifuged for 5 minutes at 2000 rpm and the supernatant medium was removed, keeping only the cell pellet. The pellet was resuspended in 45 mL of corresponding medium and split into three new TCP150.

5.3.4. Cell culture on Transwell inserts

Static HBMEC/HA co-cultures were performed on 6- and 24-well plates using Transwell polyester (PET) permeable supports with a pore size of 0.4 μm. Before cell seeding, inserts were coated with PLL and Fn coating solutions. Inserts were placed upside down with sterile tweezers and coated with PLL solution (2 $\mu g/cm^2$) on the basolateral side for 45 minutes at room temperature. Then, PLL was aspirated and inserts were flipped and placed in well plates containing PBS. Fn solution (5 $\mu g/cm^2$) was added in the upper compartment to coat the apical side for 1 hour at 37°C. Fn solution was aspirated off and coated inserts were inverted again. Meanwhile, a HA suspension was prepared and cells were seeded on top of the basolateral side with a density of $2 \cdot 10^4$ cells/cm^2. Cells were allowed to attach at room temperature inside a sterile hood. After 45 minutes, the residual cell suspension was aspirated off, inserts were flipped and placed in well plates containing pre-warmed AM. Additional AM was poured on the apical side of the inserts and culture plates were kept in the incubator at 37°C, 5% CO_2 and 80% humidity. HA were allowed to grow for 24 hours before HBMEC were seeded on the apical side. AM was substituted by EGM-2 media with 2.5% FBS and a HBMEC suspension was added in the top compartment of the inserts in order to seed at a density of 10^5 cells/cm^2. HBMEC were allowed to grow for additional 24 hours before any further experiment.

5.3.5. Cell culture on tubes

Flow experiments required culturing cells on the luminal surface of tubes. After cell expansion on TCP150, cells were seeded and cultured on straight tubes following the procedure detailed below. Prior to cell seeding, tubes were washed in 0.2% sodium dodecyl sulfate (SDS) for 20 minutes, rinsed twice with distilled water for 20 minutes and autoclaved. Sterile tubes were coated with fibronectin (Fn) 100 μg/mL in PBS overnight at 4°C. A cell suspension was prepared as described above and resuspended at 10^6 cells/mL. In order to ensure homogeneous distribution of cells along the inner surfaces of tubes, these were placed in a cylindrical, 25 cm diameter rotator turning at 3 rpm inside a 37°C, 5% CO_2 humidified incubator. After 48 hours of static culture, tubes were ready to be connected to a perfusion bioreactor. During dynamic culture, HBMEC were cultured with EDCM.

5.3.6. Astrocyte conditioned medium collection

HA were cultured in TCP150 with AM during the expansion phase. At confluence, supernatant was removed and cells were rinsed with 15 mL PBS. After aspirating off PBS, cells were incubated in EBM-2 for 48h. During that period of time, secreted cellular factors were released, conditioning the medium. Then, supernatant was collected and sterile-filtered to remove cellular debris. Resulting astrocyte-conditioned media (ACM) was aliquoted and stored at -80°C until use.

5.4. Perfusion bioreactor

The perfusion bioreactor is a flow delivery system designed to provide the tubular constructs with any flow pattern (steady, pulsatile, oscillatory) and to enable study of how cells react to different flow stimuli. It was designed coupled to a humidified incubator (37°C, 5%CO_2) where tubing and cell-seeded constructs are placed and connected to flow. Flow is driven by analogic peristaltic pumps consisting of a digital drive and a pump head with 12 channels and 8 rollers (MCP-Standard ISM 404, Ismatec, Vancouver, WA, USA). The setup used to propel flow through the cell-seeded tubes was organized as a sterile closed-system with a set of elements connected between them (Figure 5.9). Generally, the outlet of a glass reservoir was connected to two-stop pump Pharmed BPT tubing with the help of Silastic® tubing and PVDF straight connectors (Cole Parmer, USA). The outlet of the pump tube was followed by additional Silastic® tubing, the cell-seeded tube (10-15 cm) and an additional Silastic® tube connected to the inlet of the glass reservoir, closing the dynamic loop. Static control loops consisted in Silastic® tubing connecting both extremes of the cell-seeded tubes. Cells were exposed to both steady and pulsatile (1 Hz) flow with an average shear stress ranging from 10 to 40 dyn/cm^2. Prior to the experiments, flow profiles were validated by measuring flow using ultrasound flow probes (Transonic Systems, USA) coupled to a data acquisition system. The average shear stress applied to the cells and associated to the measured flow did not differ more than 5% from the theoretical shear stress in any of the flow patterns used (Figure 5.10).

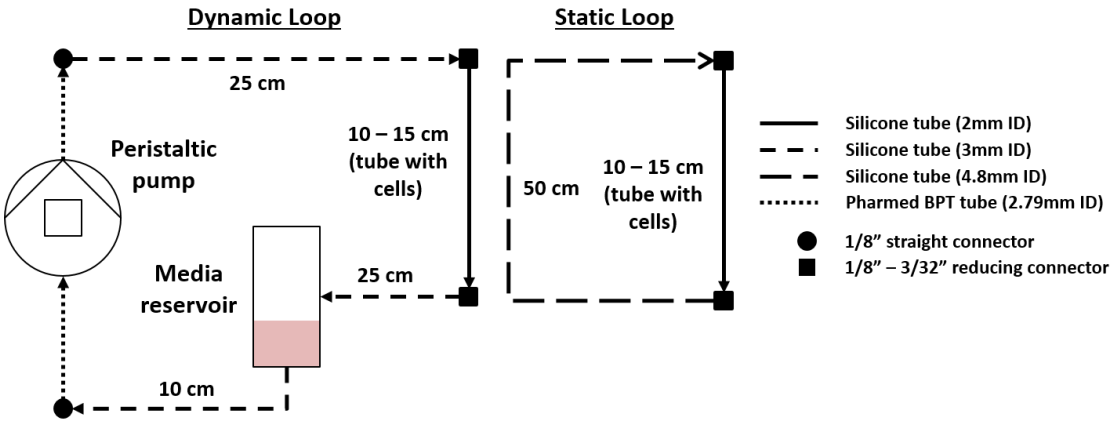

Figure 5.9. General connection disposition and scheme of the bioreactor.

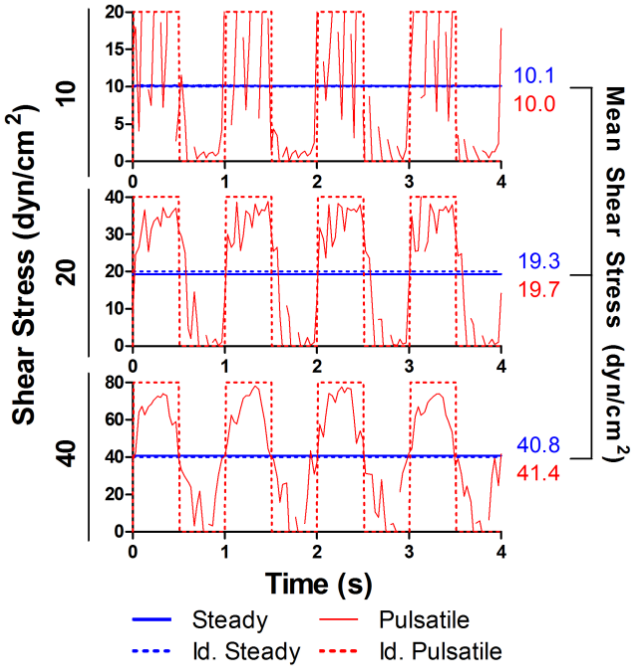

Figure 5.10. Shear stress profiles of measured and idealized flow patterns.

5.5. Permeability assay

Permeability assays were performed on HBMEC/HA co-cultures in 24-well plate Transwell inserts. Stock solutions (1 mg/mL) of fluorescent-labeled dextrans (FITC-Dextran, Sigma) of 4, 20 and 70 kDa were prepared. 10 µL of stock solutions were added per mL of cell culture media for a final experimental concentration of 10 µg/mL. Prior to the assay, media was changed from the bottom compartment of the inserts for 1 mL of fresh non-fluorescent media. Then, apical media was aspirated and 250 µL of fluorescent media were poured so that fluorescent dyes diffuse

from the apical to the basolateral side. Samples of 100 µL were taken from the basolateral side every 30 minutes for 2.5 hours and added to black 384-well plates where fluorescence was measured (excitation: 492 nm / emission: 520 nm). Permeability coefficients (P_e) were calculated from the slope of the linear regression between the amount of solute diffusing across the membrane and diffusion time, according to Equation 5.1.

$$\frac{B}{T} \cdot V_B = P_e \cdot A \cdot 60 \cdot t \qquad \textbf{Equation 5.1}$$

Where B and T are the raw fluorescence units from the bottom and top compartments, V_B is the bottom compartment volume, A is the cross-sectional area of the membrane and t is time. In order to subtract the inherent permeability of the membrane, permeability from non-cultured insert controls was subtracted using the inverse relationship in Equation 5.2.

$$\frac{1}{P_e} = \frac{1}{slope_{cells+insert}} - \frac{1}{slope_{insert}} \qquad \textbf{Equation 5.2}$$

5.6. Cell viability assay (MTT)

Cell viability assays were performed using the MTT assay (Thermo Fisher). Prior to any assay, a stock solution of MTT 5 mg/mL in PBS was prepared. At the time of the experiment, the medium was aspirated and cells were washed with PBS. Then, fresh medium supplemented with 10% (v/v) MTT stock solution was added and cells were incubated at 37°C. After 3 – 4 hours, an equal volume of MTT solubilization solution was added with gentle mixing to dissolve the formazan crystals formed. Absorbance and background absorbance were measured at wavelengths of 570 and 690 nm, respectively. Cell viability was expressed as relative absorbance between study and control samples (Equation 5.3).

$$\text{Cell viability} = \frac{A_{570} - A_{690}}{A_{570_{CONTROL}} - A_{690_{CONTROL}}} \qquad \textbf{Equation 5.3}$$

5.7. Western Blot analysis in cell culture samples

Cells were washed twice with ice-cold PBS and were lysed with radioimmunoprecipitation assay (RIPA, Sigma) buffer containing 50 mM Tris-HCl, pH 7.4, 150 mM NaCl, 1% NP-40, 0.5% deoxycholate, 0.1% SDS and 5mM EDTA. The buffer was supplemented with protease inhibitor cocktail (Sigma) containing 2 mM AEBSF, 1mM EDTA, 130 µM bestatin, 14 µM E-64, 1 µM leupeptin and 0.3 µM aprotinin. Lysates were centrifuged at 16000 g for 30 minutes at 4°C and

supernatants were stored at -80°C until use. Protein concentration was determined using the Pierce BCA Protein Assay Kit (Thermo Fisher). Sample volumes corresponding to 5μg of total protein were dissolved with 1:10 v/v of sample reducing agent 10X (Thermo Fisher) containing 500 mM dithiothreitol, 1:4 v/v of LDS sample buffer 4X (Thermo Fisher) and enough volume of distilled water to equal 25 μL of loading samples. 10% Bis-Tris polyacrylamide gels (Thermo Fisher) were used for protein separation. Gels were transferred to nitrocellulose membranes using the iBlot transfer system from Thermo Fisher. Membranes were blocked for 60 minutes with 5% non-fat dry milk (LabScientific) solution in PBS-T (PBS with 0.05% Tween-20, Thermo Fisher) and incubated overnight at 4°C and gentle rocking with primary antibody of interest diluted at their optimal concentration in PBS-T and 10% blocking buffer (Thermo Fisher). After washing twice with PBS-T, membranes were incubated for 1 hour at room temperature and gentle rocking with appropriate HRP-conjugated secondary antibodies at their optimal concentration in PBS-T and 10% blocking buffer. Then, membranes were washed twice with PBS-T, and protein bands were detected after membrane incubation in Luminata™ Forte Western HRP substrate (Millipore, USA) with a chemiluminescent image analyzer ChemiDoc XRS+ System (BioRad, USA). Blots were quantified using Fiji imaging software (NIH). β-actin and α-tubulin served as loading controls, depending on the molecular weight of the proteins of interest.

5.8. Immunofluorescence

Tissue culture plates or cell-seeded tubes were washed with PBS and fixed with 4% paraformaldehyde for 10 minutes at room temperature. Excessive aldehydes were quenched with 0.2 M glycine in PBS for 10 minutes. After washing with PBS, cells were permeabilized using 0.5% Triton X-100 in PBS for 20 minutes at room temperature and blocked with 5% goat serum (Sigma) in PBS for 60 minutes at room temperature. Then, cells were labeled overnight at 4°C with primary antibodies diluted at their optimal concentration in 1.5% goat serum in PBS, followed by a 1.5-hour incubation at room temperature in secondary antibodies diluted at their optimal concentration in 1.5% goat serum in PBS. Two additional washes with PBS were performed to remove any unbound antibody. Nuclear staining with DAPI 1 μg/mL in PBS (Thermo Fisher) was also routinely conducted. Samples were imaged using an epifluorescence microscope Nikon Eclipse Ti-E. Antibody controls were included in all experiments.

5.9. Antibodies

Table 5.4 and Table 5.5 summarize the primary and secondary antibodies used for Western Blot (WB) and immunofluorescence (IF) with their respective dilutions.

Table 5.4. Primary antibodies used in WB and IF.

Primary antibodies	IF dilution	WB dilution
Mouse monoclonal anti-Claudin 5 (Thermo Fisher)	N/A	1:2000
Rabbit polyclonal anti-β actin (Cell Signaling)	N/A	1:1000
Rabbit polyclonal anti-CD31 (abcam)	1:200	N/A
Rabbit polyclonal anti-ERK (Cell Signaling)	N/A	1:1000
Rabbit polyclonal anti-pERK (Cell Signaling)	N/A	1:2000
Rabbit polyclonal anti-GFAP (abcam)	1:1000	1:5000
Rabbit polyclonal anti-GLUT1 (abcam)	N/A	1:1000
Rabbit polyclonal anti-P-glycoprotein (abcam)	N/A	1:1000
Rabbit polyclonal anti-Src (Cell Signaling)	N/A	1:1000
Rabbit polyclonal anti-pSrc (Cell Signaling)	N/A	1:1000
Mouse monoclonal anti-α-tubulin (Sigma)	N/A	1:2000
Rabbit polyclonal anti-ZO1 (Thermo Fisher)	1:50	1:1000

Table 5.5. Secondary antibodies used in WB and IF.

Secondary antibodies	IF dilution	WB dilution
Alexa Fluor® 488 goat anti-mouse IgG (H+L) (Thermo Fisher)	1:100	N/A
Alexa Fluor® 488 goat anti-rabbit IgG (H+L) (Thermo Fisher)	1:100	N/A
Alexa Fluor® 568 goat anti-mouse IgG (H+L) (Thermo Fisher)	1:100	N/A
Alexa Fluor® 568 goat anti-rabbit IgG (H+L) (Thermo Fisher)	1:100	N/A
Alexa Fluor® 647 goat anti-mouse IgG (H+L) (Thermo Fisher)	1:100	N/A
Alexa Fluor® 647 goat anti-rabbit IgG (H+L) (Thermo Fisher)	1:100	N/A
HRP-conjugated goat anti-mouse IgG (H+L) (Bio-Rad)	N/A	1:1000
HRP-conjugated goat anti-rabbit IgG (H+L) (abcam)	N/A	1:1000

5.10. Efflux activity assay

Cell-seeded tubes were incubated with 10 µM Rhodamine-123 (Rho123, Thermo Fisher), a fluorescent dye and substrate of P-gp, in EGM-2 for 60 minutes. Then, cells were washed three times with PBS and incubated with fresh media for 60 minutes, period in which incorporated Rho123 is released by efflux activity. Conditioned supernatant was collected and cells were washed again three times with ice-cold PBS before lysis with 2% Triton X-100 in PBS supplemented with protease inhibitor cocktail. Total protein concentration was determined using the Pierce BCA Protein Assay Kit and Rho123 concentrations were obtained after fluorescent measurements (excitation: 490 nm / emission: 520 nm) against standard curves using a Varioskan Flash Multimode Reader (Thermo Fisher). Rho123 concentrations were normalized to total protein in cell lysates.

5.11. Rat animal models

The procedures that involved experimental animals with rats were conducted in accordance with the international European Guidelines in Use of Experimental Animals and were approved by the Ethic committee of Parc de Recerca Biomedica de Barcelona and Direcció General del Medi Natural i Biodiversitat Committee (IACUC) of Generalitat de Catalunya (Protocol reference: AOS-15-1712AE). Normotensive and stroke-prone spontaneously hypertensive (SPSHR) male Sprague-Dawley rats (250 g) were used in this study. The rats had free access to rat chow and water *ad libitum* prior to use in the experiments.

5.12. Evans Blue dye permeability assay

Evans Blue dye (EBD, Sigma) was dissolved in PBS at 4% (w/v). 1 mL of stock solution was injected in each rat through an intravenous (IV) tail vein injection. After 4 hours, animals were euthanized and a saline solution was perfused through the animal vasculature to clear blood vessels from residual EBD. Rat brains were extracted and allowed to dry for 48 hours before weighting the samples. EBD was extracted by addition of a 50% (w/v) solution of trichloroacetic acid (TCA) and tissue homogenization with the help of pellet pestles. Samples were centrifuged for 30 minutes at 10000 g and supernatant was collected. 30 µL of each sample were added to a black 96-well plate and were supplemented with 90 µL of 95% ethanol. EBD concentrations were obtained after fluorescent measurements (excitation: 620 nm / emission: 680 nm) against standard curves using a Varioskan Flash Multimode Reader (Thermo Fisher). EBD concentrations were normalized to dry-weight of samples.

5.13. Western Blot analysis in brain tissue samples

Brains were extracted from euthanized animals and contained in microcentrifuge tubes. 300 µL of RIPA buffer (containing 50 mM Tris-HCl, pH 7.4, 150 mM NaCl, 1% NP-40, 0.5% deoxycholate, 0.1% SDS and 5mM EDTA) were added in each tube. Then, tissue samples were homogenized manually using pellet pestles (Sigma) for 2 min at 4°C in order to allow cell lysis and protein dissolution into the buffer. Lysates were centrifuged at 16000 g for 30 minutes at 4°C and supernatants were stored at -80°C until use. Further steps were performed as indicated in Chapter 5.7.

5.14. Renal artery microanatomy and renal denervation study

5.14.1. Animal models and experimental overview

All animal experiments with swine were performed at CBSET, Inc. (Lexington, Massachusetts, USA) and adhered to the Guide for the Care and Use of Laboratory Animals under an institutional animal care and use committee (IACUC)-approved protocol. In total, 30 renal arteries from 15 castrated male Yorkshire swine (age 4.5 to 5.0 months) were assessed.

Group 1 consisted of 8 pigs that did not undergo ostial RDN but were used to analyze nerve size and positional distribution at the same 7 distances from the aorta.

Group 2 consisted of 2 pigs undergoing denervation with five electrodes of a prototype irrigated multi-electrode helical catheter (catheter 1).

Group 3 consisted of 5 pigs undergoing denervation with eight electrodes of a prototype multi-electrode basket catheter (catheter 2).

In animals undergoing renal denervation (Groups 2 and 3), a custom designed generator controlled the power of each electrode based on pre-specified power and temperature set points, and also controlled the irrigation rate of room temperature saline (~23°C) via ports along each electrode. Arteries were ablated for 60 seconds and, in the case of group 2, with an irrigation rate of 30 mL/s. In one animal from Group 2 and three animals from Group 3, the catheter was rotated 180° between two consecutive 30 seconds treatments. Angiography was performed pre and post-treatment to identify and confirm treatment locations.

All animals were euthanized on day 7 and a limited necropsy performed. Each renal artery with associated aorta and surrounding tissue was removed and fixed in neutral buffered formalin.

5.14.2. Histology of renal arteries

Each renal artery (RA) with surrounding tissue was trimmed at intervals of 3 to 5 mm to yield 3 cross sections at the aortic ostium. Anatomic orientation was preserved through tissue harvest and processing (e.g., via inking, tagging, and standardization of embedding and slide generation). One hematoxylin and eosin-stained slide and one elastin Masson's trichrome-stained slide were generated per paraffin-embedded section.

5.14.3. Histopathology evaluation and nerve assessment of renal arteries

A board-certified veterinary pathologist, using light microscopy, examined the histologic sections of the renal arteries and associated tissue. Tissue ablation areas were detected by visualization of coagulative or necrotic changes. Nerves were counted on a quadrant basis and their status with regard to treatment zone was determined.

RA microanatomy was evaluated in histological sections located at 7 different distances from the RA aortic ostium (~0.0, ~3.0, ~6.0, ~9.0, ~12.0, ~15.0, ~21.0 mm), where nerve distributions differ. Nerve size was defined by its shape area. Nerve location was defined by its distance from the RA luminal surface and angle relative to the lumen centroid. Lymph node and ablation areas were outlined by a set of points whose distance and angle relative to the lumen were evaluated as well. A set of semi-automatic ImageJ scripts (Annexes 8.1, 8.2 and 8.3) allowed measuring all metrics after manually outlining the RA lumen, nerves, lymph nodes and ablation areas (Figure 5.11.A).

Normalized illustrative maps were generated with MATLAB after shifting each individual depth by a representative RA lumen radius of 2.5 mm.[210] As both left and right arteries contributed to the composite maps, the orientation of right arterial structures was shifted by 180° to maintain consistent orientation. Maps included overlays of nerves, lymph nodes and/or traced ablation areas (Figure 5.11.B).

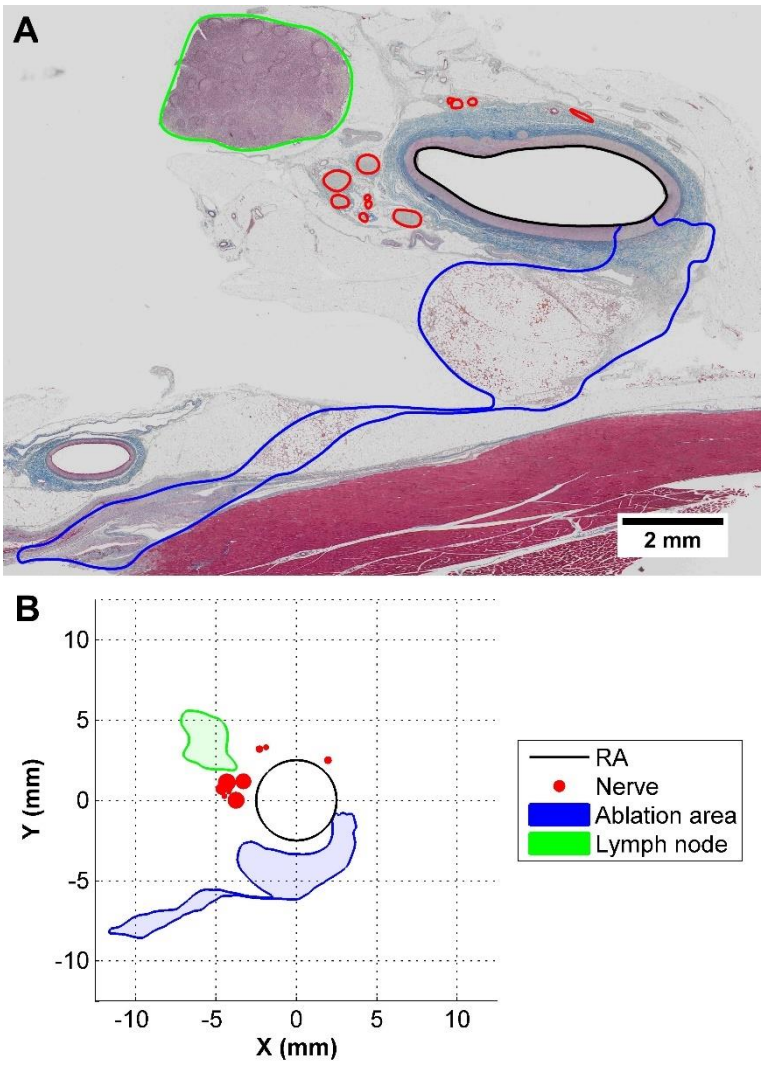

Figure 5.11. Outlined histological section of porcine renal artery (A) and normalized illustrative map (B).

5.15. Statistical analysis

All *in vitro* experiments were performed on triplicate or quadruplicate specimens (n=3-4) and repeated at least in two independent experiments. Data from each experiment are expressed as mean ± standard error of the mean (SEM). Statistical differences were analyzed using GraphPad Prism 5 software. Difference between two measurements was tested using unpaired Student's t-test. Difference between sets of measurements was tested using one-way analysis of variance (ANOVA), followed by Tukey´s *post hoc* comparison test. Values of $P < 0.05$ were considered statistically significant and are represented with an asterisk symbol (*) in graphical representations.

5.16. Permissions

- Figure 1.1 was reproduced from *Journal of Inherited Metabolic Disease*, Blood-brain barrier structure and function and the challenges for CNS drug delivery, 2013, 36(3), 437 – 449, N.J. Abbott, with permission from Springer.
- Figure 1.2 and Figure 1.3 were reprinted by permission from Macmillan Publishers Ltd: *Nature Reviews Neuroscience*, Astrocyte-endothelial interactions at the blood-brain barrier, 2006, 7(1), 41 – 53, N.J. Abbott, L Röhnbäck, E. Hansson, copyright 2006.
- Figure 1.4 was reprinted from *NeuroRx*, Blood-brain barrier active efflux transporters: ATP-binding cassette gene family, 2005, 2(1), 86 – 98, W. Löscher, H. Potschka, with permission from Springer.
- Figure 1.6 was reproduced from *Journal of Cerebral Blood Flow & Metabolism*, A dynamic in vitro BBB model for the study of immune cell trafficking into the central nervous system, 2011, 31(2), 767 – 777, L. Cucullo, N. Marchi, M. Hossain, D. Janigro.
- Figure 1.6.B was reproduced from *Biomedical microdevices*, BBB on chip: microfluidic platform to mechanically and biochemically modulate blood-brain barrier function, 2013, 15(1), 145 – 50, L. Griep, F. Wolbers, B. de Wagenaar, P.M. ter Braak, B.B. Weksler, I. A. Romero, P.O. Couraud, I. Vermes, A.D. van der Meer, A. van der Berg, with permission from Springer.
- Figure 1.6.C was reproduced from *Lab on a Chip*, Sym-BBB: A Microfluidic Blood-Brain Barrier Model, 2013, 13(6), 1093 – 1101, B. Prabhakarpandian, M. Shen, J.B. Nichols, I.R. Mills, M. Sidoryk-Wegrzynowicz, M. Aschner, K. Pant, with permission of The Royal Society of Chemistry.
- Figure 1.6.D was reproduced from *Lab on a Chip*, Characterization of a microfluidic in vitro model of the blood-brain barrier (μBBB), 2012, 12(10), 1784 – 1792, R. Booth, H. Kim, with permission of The Royal Society of Chemistry.
- Figure 1.6.E was reproduced from *Lab on a Chip*, A modular approach to create a neurovascular unit-on-a-chip, 2013, 13(4), 542 – 553, A. Achyuta, A. Conway, R. Crouse, E.C. Bannister, R.N. Lee, C.P. Katnik, A.A. Behensky, J. Cuevas, S.S. Sundaram, with permission of The Royal Society of Chemistry.
- Figure 1.7 and Figure 1.8 were reproduced from *American Journal of Physiology. Heart and Circulation Physiology*, Mechanotransduction and endothelial cell homeostasis: the wisdom of the cell, 2007, 292(3), H1209 – H1224, S. Chien.

- Figure 1.9, Figure 1.10 and Figure 1.11 were reprinted from *Journal of the American College of Cardiology*, Mechanical factors in arterial aging: A clinical perspective, 2007, 50(1), 1 – 13, M. O'Rourke, J. Hashimoto, with permission from Elsevier.
- Figure 1.12 was reproduced with permission from Wolters Kluwer: Circulation, H. Krum, P. Sobotka, F. Mahfoud, M. Böhm, M. Esler, M. Schlaich, Device-based antihypertensive therapy: Therapeutic modulation of the autonomic nervous system, 2011, 123(2), 209 – 215.

6. Conclusions

Conclusions

The hypothesis that the performance of the Blood-Brain Barrier (BBB) is affected by vascular hemodynamics was tested in a series of *in vitro* experiments performed in human brain microvascular endothelial cells exposed to different shear stress levels and pulsatile flow. Renal artery denervation therapy was studied, as a potential recovery strategy of BBB phenotype.

Human brain microvascular endothelial cells were exposed to physiological or abnormal flow patterns. Physiologic shear stress upregulated the expression of tight junction markers Zonula Occludens 1 (ZO-1) and Claudin-5. High shear stress and/or pulsatility, however, decreased their expression to basal levels and modified their cellular distribution. Junctional signaling pathways (Src/ERK) were affected analogously. While P-glycoprotein expression was only down-regulated by pulsatile flow, efflux activity significantly declined at high shear stress. When cells were exposed to pathological shear stress patterns followed by capillary-like conditions, results showed reversible recovery on the expression of tight junction markers, suggesting that hemodynamic repair is a potential therapeutic target for the recovery of BBB functional features. Overall, the exposure of human brain microvascular endothelial cells to an extensive fluid dynamic spectrum *in vitro* revealed that shear stress governs barrier phenotype at the BBB. The loss of physiological conditions showed significant damage at different aspects of the barrier phenotype of microvascular endothelium.

Tight junction markers and permeability assays were performed in rat hypertensive models to validate *in vitro* findings. Results failed to show significant alterations compared to normotensive animals. Future animal experiments require larger study populations and optimized techniques.

A dynamic *in vitro* model of the BBB was designed as a two-compartment parallel-plate flow chamber (PPFC) separated by a porous membrane. Computational fluid dynamics (CFD) validated shear stress distribution within the chamber. Proper attachment of human brain microvascular endothelial cells and human astrocytes was assessed in both PPFC. Flow exposure was successful at flow rates lower than 5 dyn/cm^2, but higher rates lead to overpressure and cell detachment. Further improvements need to be considered to use the PPFC chamber as a tool for *in vitro* BBB research.

Amongst the findings of this thesis, preliminary evidence showing that barrier phenotype is reversible upon physiological hemodynamic recovery is of special interest for the development of novel tools to repair such damage by patients' vasculature. Renal denervation, a novel technology for the treatment of resistant hypertension, has the potential to correct vascular

alterations leading to BBB impairment based on published findings. Heterogeneous results in clinical trials suggest that knowledge of renal artery microanatomy is essential to optimize renal denervation treatments. An *in vivo* study in swine models was assessed to evaluate nerve distribution and, for the first time, lymph node distribution along circumferential, axial and radial directions of the renal artery. The superior-posterior region showed higher nerve density than the anterior-posterior. Distal locations of the renal artery were more rich in nerves than proximal and middle groups. Moreover, distal nerves were closer to the arterial lumen making them more susceptible to be affected by renal denervation. Lymph node analysis showed that optimal distal regions not only had minimal presence of lymph nodes but also that such presence was more abundant beyond 2.5 mm of the lumen. Single and dual renal denervation treatments were tested. Both treatments displayed equivalent ablation depths and affected are, but the circumferential affected arc along renal arteries was higher in dual treatments. Correlation of circumferential effect and norepinephrine level in treated animals will confirm if dual treatments increase renal denervation efficacy. Results from this study indicate that understanding the renal artery microanatomy is essential for proper renal denervation therapy and its therapeutic outcomes for not only hypertension but also its consequences in peripheral areas such as the BBB.

This thesis adds new insight on vascular biology and its complicated environment, showing how hemodynamic alterations from upstream vessels may lead to downstream consequences, which can in return be corrected by targeting peripheral vessels. Here, abnormal shear stress inherent to systemic vascular disease leads to Blood-Brain Barrier impairment, which could be reverted by hemodynamic interventions. Renal denervation is a potential therapy that needs to be further characterized in order to correlate its effects on blood pressure decrease and functional features of the Blood-Brain Barrier.

7. References

1 Abbott NJ, Rönnbäck L, Hansson E. Astrocyte-endothelial interactions at the blood-brain barrier. *Nat Rev Neurosci* 2006; **7**: 41–53.

2 Ehrlich P. *Das Sauerstoff-Bedürfnis des Organismus. Eine farbenanalytische Studie*. 1885.

3 Abbott NJ. Blood-brain barrier structure and function and the challenges for CNS drug delivery. *J Inherit Metab Dis* 2013; **36**: 437–449.

4 Bernacki J, Dobrowolska A, Nierwiñska K, Maecki A. Physiology and pharmacological role of the blood-brain barrier. *Pharmacol Rev* 2008; **60**: 600–622.

5 Gingrich MB, Junge CE, Lyuboslavsky P, Traynelis SF. Potentiation of NMDA receptor function by the serine protease thrombin. *J Neurosci* 2000; **20**: 4582–4595.

6 Abbott NJ, Patabendige AAK, Dolman DEM, Yusof SR, Begley DJ. Structure and function of the blood-brain barrier. *Neurobiol Dis* 2010; **37**: 13–25.

7 Begley D, Brightman M. Structural and functional aspects of the blood-brain barrier. *Prog Drug Res* 2003; **61**: 39–78.

8 Hawkins BT, Davis TP. The Blood-Brain Barrier / Neurovascular Unit in Health and Disease. *Pharmacol Rev* 2005; **57**: 173–185.

9 Pardridge WM. Blood-brain barrier drug targeting: the future of brain drug development. *Mol Interv* 2003; **3**: 90–105.

10 Martín-Padura I, Lostaglio S, Schneemann M, Williams L, Romano M, Fruscella P *et al.* Junctional adhesion molecule, a novel member of the immunoglobulin superfamily that distributes at intercellular junctions and modulates monocyte transmigration. *J Cell Biol* 1998; **142**: 117–127.

11 Furuse M, Hirase T, Itoh M, Nagafuchi A, Yonemura S, Tsukita S *et al.* Occludin: A novel integral membrane protein localizing at tight junctions. *J Cell Biol* 1993; **123**: 1777–1788.

12 Furuse M, Fujita K, Hiiragi T, Fujimoto K, Tsukita S. Claudin-1 and -2: Novel integral membrane proteins localizing at tight junctions with no sequence similarity to occludin. *J Cell Biol* 1998; **141**: 1539–1550.

13 Morita K, Furuse M, Fujimoto K, Tsukita S. Claudin multigene family encoding four-transmembrane domain protein components of tight junction strands. *Proc Natl Acad Sci U S A* 1999; **96**: 511–516.

14 Wolburg H. The Endothelial Frontier. In: *Blood-Brain Barriers: From Ontogeny to Artificial Interfaces*. Wiley--VCH Verlag GmbH & Co. KGaA, 2006, pp 76–107.

15 Anderson JM. Cell signalling: MAGUK magic. *Curr Biol* 1996; **6**: 382–384.

16 Correale J, Villa A. Cellular elements of the blood-brain barrier. *Neurochem Res* 2009; **34**: 2067–2077.

17 Bazzoni G, Dejana E. Endothelial Cell-to-Cell Junctions: Molecular Organization and Role in Vascular Homeostasis. *Physiol Rev* 2004; **84**: 869–901.

18 Ohtsuki S, Terasaki T. Contribution of carrier-mediated transport systems to the blood-brain barrier as a supporting and protecting interface for the brain; importance for CNS drug discovery and development. *Pharm Res* 2007; **24**: 1745–1758.

19 Hermann DM, Bassetti CL. Implications of ATP-binding cassette transporters for brain pharmacotherapies. *Trends Pharmacol Sci* 2007; **28**: 128–134.

20 Ashraf T, Ronaldson PT, Bendayan R. Drug Transport in the Brain. In: *Drug Transporters: Molecular Characterization and Role in Drug Disposition*. John Wiley & Sonc, Inc., 2007, pp 273–301.

21 Löscher W, Potschka H. Blood-brain barrier active efflux transporters: ATP-binding cassette gene family. *NeuroRx* 2005; **2**: 86–98.

22 Abbott NJ. The Bipolar Astrocyte: Polarized Features of Astrocytic Glia Underlying Physiology, with Particular Reference to the Blood-Brain Barrier. In: *Blood-Brain Barriers: From Ontogeny to Artificial Interfaces*. Wiley--VCH Verlag GmbH & Co. KGaA, 2006, pp 189–208.

23 Lee G, Bendayan R. Functional expression and localization of P-glycoprotein in the central nervous system: Relevance to the pathogenesis and treatment of neurological disorders. *Pharm Res* 2004; **21**: 1313–1330.

24 Wilhelm I, Krizbai IA. In vitro models of the blood–brain-barrier for the study of drug delivery to the brain. *Mol Pharm* 2014; **11**: 1949–1963.

25 Bicker J, Alves G, Fortuna A, Falcão A. Blood-brain barrier models and their relevance for a successful development of CNS drug delivery systems: A review. *Eur J Pharm Biopharm* 2014; **87**: 409–432.

26 Sofroniew M V., Vinters H V. Astrocytes: Biology and pathology. *Acta Neuropathol* 2010; **119**: 7–35.

27 Dore-Duffy P. Pericytes: pluripotent cells of the blood brain barrier. *Curr Pharm Des* 2008; **14**: 1581–1593.

28 Dehouck M-P, Méresse S, Delorme P, Fruchart J-C, Cecchelli R. An Easier, Reproducible, and Mass-Production Method to Study the Blood-Brain Barrier In Vitro. *J Neurochem* 1990; **54**: 1798–1801.

29 Al Ahmad A, Gassmann M, Ogunshola OO. Maintaining blood-brain barrier integrity: Pericytes perform better than astrocytes during prolonged oxygen deprivation. *J Cell Physiol* 2009; **218**: 612–622.

30 Thomsen LB, Burkhart A, Moos T. A triple culture model of the blood-brain barrier using porcine brain endothelial cells, astrocytes and pericytes. *PLoS One* 2015; **10**: 1–16.

31 Wang Y, Wang N, Cai B, Wang GY, Li J, Piao XX. In vitro model of the blood-brain barrier established by co-culture of primary cerebral microvascular endothelial and astrocyte cells. *Neural Regen Res* 2015; **10**: 2011–2017.

32 Menezes MJ, McClenahan FK, Leiton C V., Aranmolate A, Shan X, Colognato H. The Extracellular Matrix Protein Laminin 2 Regulates the Maturation and Function of the Blood-Brain Barrier. *J Neurosci* 2014; **34**: 15260–15280.

33 Wang J, Milner R. Fibronectin promotes brain capillary endothelial cell survival and proliferation through alpha5beta1 and alphavbeta3 integrins via MAP kinase signalling. *J Neurochem* 2006; **96**: 148.

34 Tilling T, Korte D, Hoheisel D, Galla HJ. Basement membrane proteins influence brain capillary endothelial barrier function in vitro. *J Neurochem* 1998; **71**: 1151–1157.

35 Rascher G, Fischmann A, Kröger S, Duffner F, Grote EH, Wolburg H. Extracellular matrix and the blood-brain barrier in glioblastoma multiforme: Spatial segregation of tenascin and agrin. *Acta Neuropathol* 2002; **104**: 85–91.

36 Rosenberg GA. Neurological diseases in relation to the blood–brain barrier. *J Cereb Blood Flow Metab* 2012; **32**: 1139–1151.

37 Yang Y, Rosenberg GA. Blood-brain barrier breakdown in acute and chronic cerebrovascular disease. *Stroke* 2011; **42**: 3323–3328.

38 Kim JH, Byun HM, Chung EC, Chung HY, Bae ON. Loss of integrity: Impairment of the blood-brain barrier in heavy metal-associated ischemic stroke. *Toxicol Res* 2013; **29**: 157–164.

39 Kamphuis W, Troletti C, Reijerkerk A, Romero I, Vries H. The Blood-Brain Barrier in Multiple Sclerosis: microRNAs as Key Regulators. *CNS Neurol Disord - Drug Targets* 2015; **14**: 157–167.

40 Correale J, Villa A. The blood-brain-barrier in multiple sclerosis: functional roles and therapeutic targeting. *Autoimmunity* 2007; **40**: 148–160.

41 Oby E, Janigro D. The blood-brain barrier and epilepsy. *Epilepsia* 2006; **47**: 1761–1774.

42 Zlokovic B V. The blood-brain barrier in health and chronic neurodegenerative disorders. *Neuron* 2008; **57**: 178–201.

43 Daneman R. The blood-brain barrier in health and disease. *Ann Neurol* 2012; **72**: 648–672.

44 Schwaninger M, Sallmann S, Petersen N, Schneider A, Prinz S, Libermann TA *et al.* Bradykinin induces interleukin-6 expression in astrocytes through activation of nuclear factor-??B. *J Neurochem* 1999; **73**: 1461–1466.

45 Bradl M, Lassmann H. Progressive multiple sclerosis. *Semin Immunopathol* 2009; **31**: 455–465.

46 Plumb J, McQuaid S, Mirakhur M, Kirk J. Abnormal endothelial tight junctions in active lesions and normal-appearing white matter in multiple sclerosis. *Brain Pathol* 2002; **12**: 154–169.

47 Pascual JM, Wang D, Lecumberri B, Yang H, Mao X, Yang R *et al.* GLUT1 deficiency and other glucose transporter diseases. *Eur J Endocrinol* 2004; **150**: 627–633.

48 Marchi N, Hallene KL, Kight KM, Cucullo L, Moddel G, Bingaman W *et al.* Significance of MDR1 and multiple drug resistance in refractory human epileptic brain. *BMC Med* 2004; **2**: 37.

49 Gaillard PJ, De Boer AG, Breimer DD. Pharmacological investigations on lipopolysaccharide-induced permeability changes in the blood-brain barrier in vitro. *Microvasc Res* 2003; **65**: 24–31.

50 Zlokovic B V, Deane R, Sagare AP, Bell RD, Winkler EA. Low-density lipoprotein receptor-related protein-1: a serial clearance homeostatic mechanism controlling Alzheimer's

amyloid β-peptide elimination from the brain. *J Neurochem* 2010; **115**: 1077–1089.

51 Pluta R. Is the ischemic blood–brain barrier insufficiency responsible for full-blown Alzheimer's disease? *Neurol Res* 2006; **28**: 665–671.

52 WHO. Neurological Disorders: Public Health Challenges. *Arch Neurol* 2008; **65**: 154.

53 Velasco-Aguirre C, Morales F, Gallardo-Toledo E, Guerrero S, Giralt E, Araya E *et al.* Peptides and proteins used to enhance gold nanoparticle delivery to the brain: preclinical approaches. *Int J Nanomedicine* 2015; **10**: 4919–36.

54 Arranz-Gibert P, Guixer B, Malakoutikhah M, Muttenthaler M, Guzmán F, Teixidó M *et al.* Lipid Bilayer Crossing-The Gate of Symmetry. Water-Soluble Phenylproline-Based Blood-Brain Barrier Shuttles. *J Am Chem Soc* 2015; **137**: 7357–7364.

55 Oller-Salvia B, Sánchez-Navarro M, Giralt E, Teixidó M. Blood–brain barrier shuttle peptides: an emerging paradigm for brain delivery. *Chem Soc Rev* 2016; **45**. doi:10.1039/C6CS00076B.

56 Sánchez-Purrà M, Ramos V, Petrenko VA, Torchilin VP, Borrós S. Double-targeted polymersomes and liposomes for multiple barrier crossing. *Int J Pharm* 2016; **511**: 946–956.

57 Urich E, Lazic SE, Molnos J, Wells I, Freskgård PO. Transcriptional profiling of human brain endothelial cells reveals key properties crucial for predictive in vitro blood-brain barrier models. *PLoS One* 2012; **7**. doi:10.1371/journal.pone.0038149.

58 Urich E, Patsch C, Aigner S, Graf M, Iacone R, Freskgård P-O. Multicellular self-assembled spheroidal model of the blood brain barrier. *Sci Rep* 2013; **3**: 1500.

59 Naik P, Cucullo L. In Vitro Blood-Brain Barrier Models: Current and Perspective Technologies. *J Pharm* 2012; **101**: 1337–1354.

60 Garberg P, Ball M, Borg N, Cecchelli R, Fenart L, Hurst RD *et al.* In vitro models for the blood-brain barrier. *Toxicol Vitr* 2005; **19**: 299–334.

61 Toth A, Veszelka S, Nakagawa S, Niwa M, A. Deli M. Patented In Vitro Blood-Brain Barrier Models in CNS Drug Discovery. *Recent Pat CNS Drug Discov* 2011; **6**: 107–118.

62 Palmiotti CA, Prasad S, Naik P, Abul KMD, Sajja RK, Achyuta AH *et al.* In vitro cerebrovascular modeling in the 21st century: current and prospective technologies. *Pharm Res* 2014; **31**: 3229–50.

63 Alavijeh MS, Chishty M, Qaiser MZ, Palmer AM. Drug metabolism and pharmacokinetics, the blood-brain barrier, and central nervous system drug discovery. *NeuroRx* 2005; **2**: 554–571.

64 Weksler BB, Subileau EA, Perrière N, Charneau P, Holloway K, Leveque M *et al.* Blood-brain barrier-specific properties of a human adult brain endothelial cell line. *FASEB J* 2005; **19**: 1872–4.

65 Weksler B, Romero I a, Couraud P-O. The hCMEC/D3 cell line as a model of the human blood brain barrier. *Fluids Barriers CNS* 2013; **10**: 16.

66 Lippmann ES, Azarin SM, Kay JE, Nessler R a, Wilson HK, Al-Ahmad A *et al.* Derivation of Blood-Brain Barrier Endothelial Cells from Human Pluripotent Stem Cells. *Nat Biotechnol*

2012; **30**: 783–791.

67 Lippmann ES, Al-Ahmad A, Palecek SP, Shusta E V. Modeling the blood-brain barrier using stem cell sources. *Fluids Barriers CNS* 2013; **10**: 2.

68 Netto DJ, Chen PC, Sobin SS, Lees JY. Demonstration of Uniform Capillary Basal Lamina Thickness by Computer Technology. 1991; **19**: 209–217.

69 Davies PF. Flow-Mediated Endothelial Mechanotransduction. *Physiol Genomics* 1995; **75**: 519–560.

70 Azuma N, Duzgun SA, Ikeda M, Kito H, Akasaka N, Sasajima T *et al.* Endothelial cell response to different mechanical forces. *J Vasc Surg* 2000; **32**: 789–794.

71 Cucullo L, Hossain M, Puvenna V, Marchi N, Janigro D. The role of shear stress in Blood-Brain Barrier endothelial physiology. *BMC Neurosci* 2011; **12**: 40.

72 Cucullo L, Marchi N, Hossain M, Janigro D. A dynamic in vitro BBB model for the study of immune cell trafficking into the central nervous system. *J Cereb Blood Flow Metab* 2011; **31**: 767–777.

73 Griep LM, Wolbers F, de Wagenaar B, ter Braak PM, Weksler BB, Romero IA *et al.* BBB on chip: microfluidic platform to mechanically and biochemically modulate blood-brain barrier function. *Biomed Microdevices* 2013; **15**: 145–50.

74 Prabhakarpandian B, Shen M-C, Nichols JB, Mills IR, Sidoryk-Wegrzynowicz M, Aschner M *et al.* Sym-BBB: A Microfluidic Blood-Brain Barrier Model. *Lab Chip* 2013; **13**: 1093–1101.

75 Booth R, Kim H. Characterization of a microfluidic in vitro model of the blood-brain barrier (μBBB). *Lab Chip* 2012; **12**: 1784–92.

76 Achyuta AKH, Conway AJ, Crouse RB, Bannister EC, Lee RN, Katnik CP *et al.* A modular approach to create a neurovascular unit-on-a-chip. *Lab Chip* 2013; **13**: 542–553.

77 Wiese G, Barthel SR, Dimitroff CJ. Analysis of Physiologic E-Selectin-Mediated Leukocyte Rolling on Microvascular Endothelium. *J Vis Exp* 2009; **24**: e1009.

78 Hsiao TW, Tresco PA, Hlady V. Astrocytes alignment and reactivity on collagen hydrogels patterned with ECM proteins. *Biomaterials* 2015; **39**: 124–130.

79 East E, Golding JP, Phillips JB. A versatile 3D culture model facilitates monitoring of astrocytes undergoing reactive gliosis. *J Tissue Eng Regen Med* 2009; **3**: 634–646.

80 Placone AL, McGuiggan PM, Bergles DE, Guerrero-Cazares H, Quiñones-Hinojosa A, Searson PC. Human astrocytes develop physiological morphology and remain quiescent in a novel 3D matrix. *Biomaterials* 2015; **42**: 134–143.

81 Frampton JP, Hynd MR, Shuler ML, Shain W. Fabrication and optimization of alginate hydrogel constructs for use in 3D neural cell culture. *Biomed Mater* 2011; **6**: 015002.

82 Puschmann TB, Zandén C, De Pablo Y, Kirchhoff F, Pekna M, Liu J *et al.* Bioactive 3D cell culture system minimizes cellular stress and maintains the in vivo-like morphological complexity of astroglial cells. *Glia* 2013; **61**: 432–440.

83 Al Ahmad A, Taboada CB, Gassmann M, Ogunshola OO. Astrocytes and pericytes

differentially modulate blood-brain barrier characteristics during development and hypoxic insult. *J Cereb Blood Flow Metab* 2011; **31**: 693–705.

84 Hawkins BT, Grego S, Sellgren KL. Three-dimensional culture conditions differentially affect astrocyte modulation of brain endothelial barrier function in response to transforming growth factor β1. *Brain Res* 2015; **1608**: 167–176.

85 Zheng Y, Chen J, Craven M, Choi NW, Totorica S, Diaz-Santana A *et al.* In vitro microvessels for the study of angiogenesis and thrombosis. *Proc Natl Acad Sci U S A* 2012; **109**: 9342–7.

86 Tourovskaia A, Fauver M, Kramer G, Simonson S, Neumann T. Tissue-engineered microenvironment systems for modeling human vasculature. *Exp Biol Med* 2014; **239**: 1264–1271.

87 Faber JE, Stouffer GA. Introduction to basic hemodynamic principles. In: *Cardiovascular Hemodynamics*. Blackwell Publishing, 2008, pp 3–16.

88 Davies PF, Remuzzi A, Gordon EJ, Dewey CF, Gimbrone MA. Turbulent fluid shear stress induces vascular endothelial cell turnover in vitro. *Proc Natl Acad Sci U S A* 1986; **83**: 2114–7.

89 Papaioannou TG, Stefanadis C. Vascular wall shear stress: basic principles and methods. *Hellenic J Cardiol* 2005; **46**: 9–15.

90 Chien S. Mechanotransduction and endothelial cell homeostasis: the wisdom of the cell. *Am J Physiol Heart Circ Physiol* 2007; **292**: H1209–H1224.

91 Sumpio B. *Hemodynamic forces and vascular cell biology.* R.G. Landes, 1993.

92 Janoštiak R, Pataki AC, Brábek J, Rösel D. Mechanosensors in integrin signaling: The emerging role of p130Cas. *Eur J Cell Biol* 2014; **93**: 445–454.

93 Shay-Salit A, Shushy M, Wolfovitz E, Yahav H, Breviario F, Dejana E *et al.* VEGF receptor 2 and the adherens junction as a mechanical transducer in vascular endothelial cells. *Proc Natl Acad Sci U S A* 2002; **99**: 9462–9467.

94 Chachisvilis M, Zhang YL, Frangos JA. G protein-coupled receptors sense fluid shear stress in endothelial cells. *Proc Natl Acad Sci* 2006; **103**: 15463–15468.

95 Gautam M, Gojova A, Barakat AI. Flow-Activated Ion Channels in Vascular Endothelium. *Cell Biochem Biophys* 2006; **46**: 277–284.

96 Hierck BP, Van Der Heiden K, Alkemade FE, Van De Pas S, Van Thienen J V., Groenendijk BCW *et al.* Primary cilia sensitize endothelial cells for fluid shear stress. *Dev Dyn* 2008; **237**: 725–735.

97 Curry FE, Adamson RH. Endothelial glycocalyx: Permeability barrier and mechanosensor. *Ann Biomed Eng* 2012; **40**: 828–839.

98 Resnick N, Gimbrone MA. Hemodynamic endothelial forces regulators of endothelial gene expression. *FASEB J* 1995; **9**: 874–882.

99 Li YS, Shyy JY, Li S, Lee J, Su B, Karin M *et al.* The Ras-JNK pathway is involved in shear-induced gene expression. *Mol Cell Biol* 1996; **16**: 5947–5954.

100 Milovanova T, Chatterjee S, Manevich Y, Kotelnikova I, Debolt K, Madesh M *et al.* Lung endothelial cell proliferation with decreased shear stress is mediated by reactive oxygen species. *Am J Physiol Cell Physiol* 2006; **290**: C66–76.

101 Rennier K, Ji JY. Shear stress attenuates apoptosis due to TNFα, oxidative stress, and serum depletion via death-associated protein kinase (DAPK) expression. *BMC Res Notes* 2015; **8**: 85.

102 Teichmann J, Morgenstern A, Seebach J, Schnittler HJ, Werner C, Pompe T. The control of endothelial cell adhesion and migration by shear stress and matrix-substrate anchorage. *Biomaterials* 2012; **33**: 1959–1969.

103 Seebach J, Dieterich P, Luo F, Schillers H, Vestweber D, Oberleithner H *et al.* Endothelial barrier function under laminar fluid shear stress. *Lab Invest* 2000; **80**: 1819–31.

104 Aird WC. Phenotypic Heterogeneity of the Endothelium: I. Structure, Function, and Mechanisms. *Circ Res* 2007; **100**: 158–173.

105 Chatterjee S, Fisher AB. Mechanotransduction in the endothelium: role of membrane proteins and reactive oxygen species in sensing, transduction, and transmission of the signal with altered blood flow. *Antioxid Redox Signal* 2014; **20**: 899–913.

106 Richter Y, Groothuis A, Seifert P, Edelman ER. Dynamic flow alterations dictate leukocyte adhesion and response to endovascular interventions. *J Clin Invest* 2004; **113**: 1607–1614.

107 Davies PF. Hemodynamic shear stress and the endothelium in cardiovascular pathophysiology. *Nat Clin Pract Cardiovasc Med* 2009; **6**: 16–26.

108 Martorell J, Santomá P, Kolandaivelu K, Kolachalama VB, Melgar-Lesmes P, Molins JJ *et al.* Extent of flow recirculation governs expression of atherosclerotic and thrombotic biomarkers in arterial bifurcations. *Cardiovasc Res* 2014; **103**: 37–46.

109 Cucullo L, Hossain M, Tierney W, Janigro D. A new dynamic in vitro modular capillaries-venules modular system: cerebrovascular physiology in a box. *BMC Neurosci* 2013; **14**: 18.

110 Wong AD, Ye M, Levy AF, Rothstein JD, Bergles DE, Searson PC. The blood-brain barrier: an engineering perspective. *Front Neuroeng* 2013; **6**: 7.

111 Walsh TG, Murphy RP, Fitzpatrick P, Rochfort KD, Guinan AF, Murphy A *et al.* Stabilization of brain microvascular endothelial barrier function by shear stress involves VE-cadherin signaling leading to modulation of pTyr-occludin levels. *J Cell Physiol* 2011; **226**: 3053–63.

112 Rochfort KD, Cummins PM. Thrombomodulin regulation in human brain microvascular endothelial cells in vitro: Role of cytokines and shear stress. *Microvasc Res* 2014; **97**: 1–5.

113 Rochfort KD, Collins LE, McLoughlin A, Cummins PM. Shear-dependent attenuation of cellular ROS levels can suppress proinflammatory cytokine injury to human brain microvascular endothelial barrier properties. *J Cereb Blood Flow Metab* 2015; **35**: 1648–1656.

114 Krizanac-Bengez L, Mayberg MR, Cunningham E, Hossain M, Ponnampalam S, Parkinson

FE *et al.* Loss of shear stress induces leukocyte-mediated cytokine release and blood-brain barrier failure in dynamic in vitro blood-brain barrier model. *J Cell Physiol* 2006; **206**: 68–77.

115 Krizanac-Bengez L, Hossain M, Fazio V, Mayberg M, Janigro D. Loss of flow induces leukocyte-mediated MMP/TIMP imbalance in dynamic in vitro blood-brain barrier model: role of pro-inflammatory cytokines. *Am J Physiol Cell Physiol* 2006; **291**: C740–9.

116 Battegay EJ, Lip GY, Bakris GL. Definition and Classification of Hypertension. In: *Hypertension: Principles and Practice*. Taylor & Francis Group, 2005, pp 15–22.

117 Lip GY, Beevers D. Prevalence and causes. In: *ABC of Hypertension*. Blackwell Publishing, 2007, pp 1–7.

118 O'Rourke MF. Arterial Stiffness, Systolic Blood Pressure, and Logical Treatment of Arterial Hypertension. *Hypertension* 1990; **15**: 339–347.

119 Nichols WW, O'Rourke MF, Vlachopoulos C. Properties of the arterial wall: practice. In: *McDonald's Blood Flow in Arteries - Theoretical, Experimental and Clinical Principles*. Hodder Arnold, 2011, pp 77–110.

120 O'Rourke MF, Hashimoto J. Mechanical factors in arterial aging: A clinical perspective. *J Am Coll Cardiol* 2007; **50**: 1–13.

121 Schiffrin EL, Tedgui A, Lehoux S. Mechanical Stress and the Arterial Wall. In: *Blood Pressure and Arterial Wall Mechanics in Cardiovascular Diseases*. Springer, 2014, pp 97–106.

122 Hirata K, Yaginuma T, O'Rourke MF, Kawakami M. Age-related changes in carotid artery flow and pressure pulses: Possible implications for cerebral microvascular disease. *Stroke* 2006; **37**: 2552–2556.

123 O'Rourke MF, Safar ME, Dzau V. The Cardiovascular Continuum extended: aging effects on the aorta and microvasculature. *Vasc Med* 2010; **15**: 461–8.

124 O'Rourke MF, Safar ME. Relationship between aortic stiffening and microvascular disease in brain and kidney: cause and logic of therapy. *Hypertension* 2005; **46**: 200–4.

125 Mozaffarian D, Benjamin EJ, Go AS, Arnett DK, Blaha MJ, Cushman M *et al. Heart Disease and Stroke Statistics—2016 Update: A Report From the American Heart Association*. 2015 doi:10.1161/CIR.0000000000000350.

126 Ois A, Cuadrado-Godia E, Rodríguez-Campello A, Giralt-Steinhauer E, Jiménez-Conde J, Lopez-Cuiña M *et al.* Relevance of stroke subtype in vascular risk prediction. *Neurology* 2013; **81**: 575–580.

127 Desmond DW, Moroney JT, Sano M, Stern Y. Incidence of dementia after ischemic stroke: Results of a longitudinal study. *Stroke* 2002; **33**: 2254–2260.

128 Laurent S, Katsahian S, Fassot C, Tropeano AI, Gautier I, Laloux B *et al.* Aortic stiffness is an independent predictor of fatal stroke in essential hypertension. *Stroke* 2003; **34**: 1203–1206.

129 Henskens LHG, Kroon A a, van Oostenbrugge RJ, Gronenschild EHBM, Fuss-Lejeune MMJJ, Hofman P a M *et al.* Increased aortic pulse wave velocity is associated with silent

cerebral small-vessel disease in hypertensive patients. *Hypertension* 2008; **52**: 1120–6.

130 Poels MMF, Ikram MA, Van Der Lugt A, Hofman A, Krestin GP, Breteler MMB *et al.* Incidence of cerebral microbleeds in the general population: The Rotterdam Scan Study. *Stroke* 2011; **42**: 656–661.

131 Waldstein SR, Rice SC, Thayer JF, Najjar SS, Scuteri A, Zonderman AB. Pulse Pressure and Cognitive Decline Pulse Pressure and Pulse Wave Velocity Are Related to Cognitive Decline in the Baltimore Longitudinal Study of Aging. *Hypertension* 2008; **51**: 99–104.

132 Mitchell GF, van Buchem MA, Sigurdsson S, Gotal JD, Jonsdottir MK, Kjartansson Ó *et al.* Arterial stiffness, pressure and flow pulsatility and brain structure and function: the Age, Gene/Environment Susceptibility - Reykjavik study. *Brain* 2011; **134**: 3398–407.

133 Saji N, Kimura K, Kawarai T, Shimizu H, Kita Y. Arterial stiffness and progressive neurological deficit in patients with acute deep subcortical infarction. *Stroke* 2012; **43**: 3088–90.

134 Singer J, Trollor JN, Crawford J, O'Rourke MF, Baune BT, Brodaty H *et al.* The Association between Pulse Wave Velocity and Cognitive Function: The Sydney Memory and Ageing Study. *PLoS One* 2013; **8**: 4–9.

135 Stone J, Johnstone DM, Mitrofanis J, Rourke MO. The Mechanical Cause of Age-Related Dementia (Alzheimer's Disease): The Brain is Destroyed by the Pulse. *J Alzheimer's Dis* 2015; **44**: 355–373.

136 Meng X-F, Yu J-T, Wang H-F, Tan M-S, Wang C, Tan C-C *et al.* Midlife Vascular Risk Factors and the Risk of Alzheimer's Disease: A Systematic Review and Meta-Analysis. *J Alzheimers Dis* 2014; **42**: 1295–1310.

137 Di Marco LY, Venneri A, Farkas E, Evans PC, Marzo A, Frangi AF. Vascular dysfunction in the pathogenesis of Alzheimer's disease — A review of endothelium-mediated mechanisms and ensuing vicious circles. *Neurobiol Dis* 2015; **82**: 593–606.

138 Iadecola C. The Pathobiology of Vascular Dementia. *Neuron* 2013; **80**: 844–866.

139 Iadecola C. Neurovascular regulation in the normal brain and in Alzheimer's disease. *Nat Rev Neurosci* 2004; **5**: 347–360.

140 Cooper LL, Woodard T, Sigurdsson S, van Buchem MA, Torjesen AA, Inker LA *et al.* Cerebrovascular Damage Mediates Relations Between Aortic Stiffness and Memory. *Hypertension* 2016; **67**: 176–182.

141 Schreiber S, Bueche CZ, Garz C, Braun H. Blood brain barrier breakdown as the starting point of cerebral small vessel disease? - New insights from a rat model. *Exp Transl Stroke Med* 2013; **5**: 4.

142 Toth P, Tucsek Z, Sosnowska D, Gautam T, Mitschelen M, Tarantini S *et al.* Age-related autoregulatory dysfunction and cerebromicrovascular injury in mice with angiotensin II-induced hypertension. *J Cereb Blood Flow Metab* 2013; **33**: 1732–1742.

143 Knowland D, Arac A, Sekiguchi KJ, Hsu M, Lutz SE, Perrino J *et al.* Stepwise Recruitment of Transcellular and Paracellular Pathways Underlies Blood-Brain Barrier Breakdown in Stroke. *Neuron* 2014; **82**: 603–617.

144 Chua DC, Bakris GL. Management and Treatment Guidelines. In: *Hypertension: Principles and Practice*. Taylor & Francis Group, 2005, pp 357–382.

145 Lip GY, Beevers D. Pharmacological treatment of hypertension. In: *ABC of Hypertension*. Blackwell Publishing, 2007, pp 47–55.

146 Houston MC. Treatment of hypertension. In: *Handbook of Hypertension*. John Wiley & Sons, 2009, pp 60–86.

147 Judd E, Calhoun DA. Apparent and true resistant hypertension: definition, prevalence and outcomes. *J Hum Hypertens* 2014; **28**: 463–8.

148 Pimenta E, Calhoun DA. Resistant Hypertension: Incidence, Prevalence, and Prognosis. *Circulation* 2012; **125**: 1594–1596.

149 Schlaich MP, Lambert E, Kaye DM, Krozowski Z, Campbell DJ, Lambert G *et al.* Sympathetic Augmentation in Hypertension: Role of Nerve Firing, Norepinephrine Reuptake, and Angiotensin Neuromodulation. *Hypertension* 2004; **43**: 169–175.

150 Schlaich MP, Sobotka P a, Krum H, Lambert E, Esler MD. Renal sympathetic-nerve ablation for uncontrolled hypertension. *N Engl J Med* 2009; **361**: 932–934.

151 Esler M. The sympathetic system and hypertension. *Am J Hypertens* 2000; **13**: 99S–105S.

152 DiBona GF, Esler M. Translational medicine: the antihypertensive effect of renal denervation. *AJP Regul Integr Comp Physiol* 2010; **298**: R245–R253.

153 Gulati V, White WB. Novel Approaches for the Treatment of the Patient with Resistant Hypertension: Renal Nerve Ablation. *Curr Cardiovasc Risk Rep* 2013; **7**: 401–408.

154 Bertog SC, Slevert H. Catheter-Based Technology Alternatives for Renal Denervation: An Overview. In: *Renal Denervation: A New Approach to Treatment of Resistant Hypertension*. Springer-Verlag, 2015, pp 59–61.

155 Krum H, Sobotka P, Mahfoud F, Böhm M, Esler M, Schlaich M. Device-based antihypertensive therapy: Therapeutic modulation of the autonomic nervous system. *Circulation* 2011; **123**: 209–215.

156 Krum H, Schlaich M, Whitbourn R, Sobotka PA, Sadowski J, Bartus K *et al.* Catheter-based renal sympathetic denervation for resistant hypertension: a multicentre safety and proof-of-principle cohort study. *Lancet* 2009; **373**: 1275–1281.

157 Esler MD, Krum H, Sobotka PA, Schlaich MP, Schmieder RE, Böhm M *et al.* Renal sympathetic denervation in patients with treatment-resistant hypertension (The Symplicity HTN-2 Trial): A randomised controlled trial. *Lancet* 2010; **376**: 1903–1909.

158 Esler MD, Krum H, Schlaich M, Schmieder RE, Böhm M, Sobotka PA. Renal sympathetic denervation for treatment of drug-resistant hypertension: One-year results from the symplicity htn-2 randomized, controlled trial. *Circulation* 2012; **126**: 2976–2982.

159 Krum H, Schlaich MP, Sobotka PA, Böhm M, Mahfoud F, Rocha-Singh K *et al.* Percutaneous renal denervation in patients with treatment-resistant hypertension: Final 3-year report of the Symplicity HTN-1 study. *Lancet* 2014; **383**: 622–629.

160 Bhatt DL, Kandzari DE, O'Neill WW, D'Agostino R, Flack JM, Katzen BT *et al.* A controlled trial of renal denervation for resistant hypertension. *N Engl J Med* 2014; **370**: 1393–401.

161 Tzafriri AR, Mahfoud F, Keating JH, Markham PM, Spognardi A, Wong G *et al.* Innervation patterns may limit response to endovascular renal denervation. *J Am Coll Cardiol* 2014; **64**: 1079–1087.

162 Tellez A, Rousselle S, Palmieri T, Rate IV WR, Wicks J, Degrange A *et al.* Renal artery nerve distribution and density in the porcine model: biologic implications for the development of radiofrequency ablation therapies. *Transl Res* 2013; **162**: 381–389.

163 Tzafriri AR, Keating JH, Markham PM, Spognardi A-M, L. Stanley JR, Wong G *et al.* Arterial microanatomy determines the success of energy-based renal denervation in controlling hypertension. *Sci Transl Med* 2015; **7**: 285ra65–285ra65.

164 Nakagawa T, Hasegawa Y, Uekawa K, Ma M, Katayama T, Sueta D *et al.* Renal Denervation Prevents Stroke and Brain Injury via Attenuation of Oxidative Stress in Hypertensive Rats. *J Am Heart Assoc* 2013; **2**: e000375–e000375.

165 Methe H, Balcells M, Alegret MDC, Santacana M, Molins B, Hamik A *et al.* Vascular bed origin dictates flow pattern regulation of endothelial adhesion molecule expression. *Am J Physiol Heart Circ Physiol* 2007; **292**: H2167–75.

166 Balcells M, Martorell J, Olivé C, Santacana M, Chitalia V, Cardoso AA *et al.* Smooth muscle cells orchestrate the endothelial cell response to flow and injury. *Circulation* 2010; **121**: 2192–9.

167 Lyck R, Ruderisch N, Moll AG, Steiner O, Cohen CD, Engelhardt B *et al.* Culture-induced changes in blood–brain barrier transcriptome: implications for amino-acid transporters in vivo. *J Cereb Blood Flow Metab* 2009; **29**: 1491–1502.

168 Yuan W, Lv Y, Zeng M, Fu BM. Non-invasive measurement of solute permeability in cerebral microvessels of the rat. *Microvasc Res* 2009; **77**: 166–173.

169 Li G, Simon MJ, Cancel LM, Shi ZD, Ji X, Tarbell JM *et al.* Permeability of endothelial and astrocyte cocultures: In vitro Blood-brain barrier models for drug delivery studies. *Ann Biomed Eng* 2010; **38**: 2499–2511.

170 Jiang S, Xia R, Jiang Y, Wang L, Gao F. Vascular endothelial growth factors enhance the permeability of the mouse blood-brain barrier. *PLoS One* 2014; **9**: 1–7.

171 Cipolla MJ. The Cerebral Circulation. In: *Colloquium Series on Integrated Systems Physiology: From Molecule to Function to Disease*. 2009, pp 1–59.

172 Garcia-Polite F. Automatic generation of a capillary network structure for the obtaining of a computational model of the Blood-Brain Barrier. *Master Thesis - IQS* 2012.

173 Benetos A, Laurent S, Hoeks AP, Boutouyrie PH, Safar ME. Arterial alterations with aging and high blood pressure. A noninvasive study of carotid and femoral arteries. *Arterioscler Thromb Vasc Biol* 1993; **13**: 90–97.

174 Forster S, Thumser AE, Hood SR, Plant N. Characterization of Rhodamine-123 as a Tracer Dye for Use In In vitro Drug Transport Assays. *PLoS One* 2012; **7**: e33253.

175 Hawkins BT, Rigor RR, Miller DS. Rapid loss of blood–brain barrier P-glycoprotein activity through transporter internalization demonstrated using a novel in situ proteolysis protection assay. *J Cereb Blood Flow Metab* 2010; **30**: 1593–1597.

176 Wang H-L, Lai TW. Optimization of Evans blue quantitation in limited rat tissue samples. *Sci Rep* 2014; **4**: 6588.

177 Jaffer H, Adjei IM, Labhasetwar V. Optical imaging to map blood-brain barrier leakage. *Sci Rep* 2013; **3**: 3117.

178 Hamik A, Lin Z, Kumar A, Balcells M, Sinha S, Katz J *et al.* Kruppel-like factor 4 regulates endothelial inflammation. *J Biol Chem* 2007; **282**: 13769–13779.

179 Chiu JJ, Usami S, Chien S. Vascular endothelial responses to altered shear stress: Pathologic implications for atherosclerosis. *Ann Med* 2009; **41**: 19–28.

180 Taheri S, Gasparovic C, Huisa BN, Adair JC, Edmonds E, Prestopnik J *et al.* Blood-Brain Barrier Permeability Abnormalities in Vascular Cognitive Impairment. *Stroke* 2011; **42**: 2158–2163.

181 Gottardi CJ, Arpin M, Fanning a S, Louvard D. The junction-associated protein, zonula occludens-1, localizes to the nucleus before the maturation and during the remodeling of cell-cell contacts. *Proc Natl Acad Sci U S A* 1996; **93**: 10779–10784.

182 Tarbell JM, Simon SI, Curry FE. Mechanosensing at the vascular interface. *Annu Rev Biomed Eng* 2014; **16**: 505–32.

183 Jung B, Obinata H, Galvani S, Mendelson K, Ding BS, Skoura A *et al.* Flow-Regulated Endothelial S1P Receptor-1 Signaling Sustains Vascular Development. *Dev Cell* 2012; **23**: 600–610.

184 Jalali S, Li YS, Sotoudeh M, Yuan S, Li S, Chien S *et al.* Shear stress activates p60src-Ras-MAPK signaling pathways in vascular endothelial cells. *Arterioscler Thromb Vasc Biol* 1998; **18**: 227–34.

185 Liu D-Z, Ander BP, Xu H, Shen Y, Kaur P, Deng W *et al.* Blood-brain barrier breakdown and repair by Src after thrombin-induced injury. *Ann Neurol* 2010; **67**: 526–533.

186 Bai Y, Xu G, Xu M, Li Q, Qin X. Inhibition of Src phosphorylation reduces damage to the blood-brain barrier following transient focal cerebral ischemia in rats. *Int J Mol Med* 2014; **34**: 1–10.

187 Li D, Mrsny RJ. Oncogenic Raf-1 disrupts epithelial tight junctions via downregulation of occludin. *J Cell Biol* 2000; **148**: 791–800.

188 González-Mariscal L, Tapia R, Chamorro D. Crosstalk of tight junction components with signaling pathways. *Biochim Biophys Acta* 2008; **1778**: 729–56.

189 DePaola N, Phelps JE, Florez L, Keese CR, Minnear FL, Giaever I *et al.* Electrical Impedance of Cultured Endothelium Under Fluid Flow. *Ann Biomed Eng* 2001; **29**: 648–656.

190 Seebach J, Donnert G, Kronstein R, Werth S, Wojciak-Stothard B, Falzarano D *et al.* Regulation of endothelial barrier function during flow-induced conversion to an arterial phenotype. *Cardiovasc Res* 2007; **75**: 596–607.

191 Tornavaca O, Chia M, Dufton N, Almagro LO, Conway DE, Randi AM *et al.* ZO-1 controls endothelial adherens junctions, cell-cell tension, angiogenesis, and barrier formation. *J Cell Biol* 2015; **208**: 821–838.

192 Eigenmann DE, Xue G, Kim KS, Moses A V, Hamburger M, Oufir M. Comparative study of

four immortalized human brain capillary endothelial cell lines , hCMEC / D3 , hBMEC , TY10 , and BB19 , and optimization of culture conditions , for an in vitro blood – brain barrier model for drug permeability studies Comparative stu. 2013.

193 Liu L, Shi GP. CD31: Beyond a marker for endothelial cells. *Cardiovasc Res* 2012; **94**: 3–5.

194 Alcendor DJ, Block FE, Cliffel DE, Daniels JS, Ellacott KLJ, Goodwin CR *et al.* Neurovascular unit on a chip: implications for translational applications. *Stem Cell Res Ther* 2013; **4 Suppl 1**: S18.

195 Teniente-Serra A, Grau-López L, Mansilla MJ, Fernández-Sanmartín M, Ester Condins A, Ramo-Tello C *et al.* Multiparametric flow cytometric analysis of whole blood reveals changes in minor lymphocyte subpopulations of multiple sclerosis patients. *Autoimmunity* 2016; **6934**: 1–10.

196 Ramo-Tello C, Tintore M, Rovira A, Ramio-Torrenta L, Brieva L, Saiz A *et al.* Baseline clinical status as a predictor of methylprednisolone response in multiple sclerosis relapses. *Mult Scler J* 2016; **22**: 117–121.

197 Balcells M, Wallins JS, Edelman ER. Amyloid beta toxicity dependent upon endothelial cell state. *Neurosci Lett* 2008; **441**: 319–22.

198 DaRocha-Souto B, Scotton TC, Coma M, Serrano-Pozo A, Hashimoto T, Serenó L *et al.* Brain oligomeric β-amyloid but not total amyloid plaque burden correlates with neuronal loss and astrocyte inflammatory response in amyloid precursor protein/tau transgenic mice. *J Neuropathol Exp Neurol* 2011; **70**: 360–376.

199 Perez-Nievas BG, Stein TD, Tai HC, Dols-Icardo O, Scotton TC, Barroeta-Espar I *et al.* Dissecting phenotypic traits linked to human resilience to Alzheimer's pathology. *Brain* 2013; **136**: 2510–2526.

200 Heistad DD, Marcus ML. Effect of sympathetic stimulation on permeability of the blood-brain barrier to albumin during acute hypertension in cats. *Circ Res* 1979; **45**: 331–338.

201 Mayhan WG, Werber AH, Heistad DD. Protection of cerebral vessels by sympathetic nerves and vascular hypertrophy. *Circulation* 1987; **75**: I107–12.

202 Byrom MJ, Bannon PG, White GH, Ng MKC. Animal models for the assessment of novel vascular conduits. *J Vasc Surg* 2010; **52**: 176–195.

203 Esler M. Renal denervation for hypertension: Observations and predictions of a founder. *Eur Heart J* 2014; **35**: 1178–1185.

204 Worthley SG, Tsioufis CP, Worthley MI, Sinhal A, Chew DP, Meredith IT *et al.* Safety and efficacy of a multi-electrode renal sympathetic denervation system in resistant hypertension: The EnligHTN I trial. *Eur Heart J* 2013; **34**: 2132–2140.

205 Sakakura K, Ladich E, Cheng Q, Otsuka F, Yahagi K, Fowler DR *et al.* Anatomic Assessment of Sympathetic Peri-Arterial Renal Nerves in Man. *J Am Coll Cardiol* 2014; **64**: 635–643.

206 Atherton DS, Deep NL, Mendelsohn FO. Micro-anatomy of the renal sympathetic nervous system: A human postmortem histologic study. *Clin Anat* 2012; **25**: 628–633.

207 Sakakura K, Ladich E, Edelman ER, Markham P, Stanley JRL, Keating J *et al.* Methodological Standardization for the Pre-Clinical Evaluation of Renal Sympathetic

Denervation. *JACC Cardiovasc Interv* 2014; **7**: 1184–1193.

208 van Amsterdam WAC, Blankestijn PJ, Goldschmeding R, Bleys RLAW. The morphological substrate for Renal Denervation: Nerve distribution patterns and parasympathetic nerves. A post-mortem histological study. *Ann Anat* 2016; **204**: 71–79.

209 Tzafriri AR, Bailey L, Keating J, Garcia-Polite F, Markham P, Prutchi D *et al.* TCT-84 Enhanced Circumferential Ablation using a Multi-electrode Bipolar/Unipolar Over-the - Wire Renal Denervation RF Catheter System with Closed Loop Sensing. *J Am Coll Cardiol* 2015; **66**.http://dx.doi.org/10.1016/j.jacc.2015.08.128.

210 Aytac SK, Yigit H, Sancak T, Ozcan H. Correlation between the diameter of the main renal artery and the presence of an accessory renal artery: sonographic and angiographic evaluation. *J Ultrasound Med* 2003; **22**: 433–9; quiz 440–2.

8. Annexes

8.1. Nerve morphometry in renal artery – ImageJ script

```
macro nerveMapping{
	setBatchMode(true);
	setOption("ExpandableArrays",true);
	dirF="E:\\Nerve ablation plots\\Images\\";
	dirR="E:\\Nerve ablation plots\\ROIs nerve\\";
	filelistF=getFileList(dirF);
	filelistR=getFileList(dirR);
	nF=filelistF.length;
	nR=filelistR.length;
	if(nF==nR){
		for(i=0;i<nR;i++){
			showProgress(i/nR);
			fileF=filelistF[i];
			fileR=filelistR[i];
			fileFsub=substring(fileF,0,indexOf(fileF,".jpg"));
			fileRsub=substring(fileR,0,indexOf(fileR,".zip"));
			if(fileFsub==fileRsub){
				mapping(dirF,fileF,dirR,fileR);
			}else{
				waitForUser("Error");
			}
		}
		setBatchMode(false);
		waitForUser("Execution completed");
	}else{
		waitForUser("Error");
	}
}

function mapping(dirF,fileF,dirR,fileR){
	setBatchMode(true);
	open(dirF+fileF);
	run("ROI Manager...");
	roiManager("Open",dirR+fileR);
	W=getWidth();
	H=getHeight();
	nl=0;
	Xl=newArray(1);
	Yl=newArray(1);
	Rl=newArray(1);
	sc=2/575*1000;
	sc2=sc*sc;

	//Orientation
	roiManager("Select",1);
	run("Set Measurements...", "  redirect=None decimal=3");
	run("Measure");
	ang=getResult("Angle",0);
	selectWindow("Results");
	run("Close");

	//Nerve+ganglia count
	nROI=roiManager("Count");
	selectionNG=newArray(1);
	nNG=0;
```

```
nN=0;
nG=0;
for(i=2;i<nROI;i++){
	roiManager("Select",i);
	if(selectionType()==5){
		nN=i-2;
		nG=nROI-i-1;
	}else{
		selectionNG[nNG]=i;
		nNG+=1;
	}
}
if(nN==0){
	nN=nNG;
}

//Output arrays
typeNG=newArray(nNG);
areaNG=newArray(nNG);
XcNG=newArray(nNG);
YcNG=newArray(nNG);
lengthNG=newArray(nNG);
angleNG=newArray(nNG);

//Entiy type
for(i=0;i<nNG;i++){
	if(i<nN){
		typeNG[i]="N";
	}else{
		typeNG[i]="G";
	}
}

//Lumen outline + centroid and outline coordinate determination
run("Set Measurements...", "centroid redirect=None decimal=3");
roiManager("Select",0);
roiManager("Measure");
Xc=getResult("X",0);
Yc=getResult("Y",0);
selectWindow("Results");
run("Close");
roiManager("Deselect");
newImage("Lumen outline", "8-bit white", W, H, 1);
roiManager("Select",0);
setForegroundColor(0,0,0);
run("Draw");
for(i=0;i<H;i++){
	for(j=0;j<W;j++){
		if(getPixel(j,i)==0){
			Xl[nl]=j;
			Yl[nl]=i;
			Rl[nl]=-atan2(Yl[nl]-Yc,Xl[nl]-Xc)*180/PI;
			nl++;
		}
	}
}
selectWindow("Lumen outline");
```

```
	run("Close");
		Rlranks=Array.rankPositions(Rl);
	Rl=Array.sort(Rl);
	XlT=Array.copy(Xl);
	YlT=Array.copy(Yl);
	for(i=0;i<nl;i++){
		Xl[i]=XlT[Rlranks[i]];
		Yl[i]=YlT[Rlranks[i]];
	}

	//Measurement of area and centroid per nerve
	run("Set Measurements...", "area centroid redirect=None decimal=3");
	roiManager("Select",selectionNG);
	roiManager("Measure");
	for(i=0;i<nNG;i++){
		areaNG[i]=getResult("Area",i)*(sc*sc/1e6); //Scaled to mm^2
		XcNG[i]=getResult("X",i); //Unscaled
		YcNG[i]=getResult("Y",i); //Unscaled
	}
	selectWindow("Results");
	run("Close");

	//Lumen outline + centroid and outline coordinate determination
	for(i=0;i<nNG;i++){
		angleNG[i]=-atan2(YcNG[i]-Yc,XcNG[i]-Xc)*180/PI;
		for(j=0;j<nl-1;j++){
			if((Rl[j]-angleNG[i])<0 && (Rl[j+1]-angleNG[i])>=0){
				lengthNG[i]=sqrt(pow(Xl[j]-XcNG[i],2)+pow(Yl[j]-YcNG[i],2));
				break
			}else if(j==nl-2){
				lengthNG[i]=sqrt(pow(Xl[nl-1]-XcNG[i],2)+pow(Yl[nl-1]-YcNG[i],2));
				break
			}
		}
		angleNG[i]-=ang;
		if(angleNG[i]>180){
			angleNG[i]-=360;
		}
		XcNG[i]=(XcNG[i]-Xc)*sc/1000;
		YcNG[i]=-(YcNG[i]-Yc)*sc/1000;
		lengthNG[i]*=sc/1000;
		setResult("Type",i,typeNG[i]);
		setResult("Area",i,areaNG[i]);
		setResult("X",i,XcNG[i]);
		setResult("Y",i,YcNG[i]);
		setResult("Angle",i,angleNG[i]);
		setResult("Length",i,lengthNG[i]);
		saveAs("Results",
"E:Results\\Nerves\\"+substring(fileF,0,indexOf(fileF,".jpg"))+"_Results.txt");
		close(fileF);
	}
	roiManager("Deselect");
	roiManager("Delete");
}
```

8.2. Lymph node morphometry in renal artery – ImageJ script

```
macro lymphNodeMapping{
	setBatchMode(true);
	setOption("ExpandableArrays",true);
	dirF="E:\\Images\\";
	dirR="E:\\ROIs lymph node\\";
	filelistF=getFileList(dirF);
	filelistR=getFileList(dirR);
	nF=filelistF.length;
	nR=filelistR.length;
	if(nF==nR){
		for(i=0;i<nR;i++){
			showProgress(i/nR);
			fileF=filelistF[i];
			fileR=filelistR[i];
			fileFsub=substring(fileF,0,indexOf(fileF,".jpg"));
			fileRsub=substring(fileR,0,indexOf(fileR,".zip"));
			if(fileFsub==fileRsub){
				LNmapping(dirF,fileF,dirR,fileR);
			}else{
				waitForUser("Error");
			}
		}
		setBatchMode(false);
		waitForUser("Execution completed");
	}else{
		waitForUser("Error");
	}
}

function LNmapping(dirF,fileF,dirR,fileR){
	setBatchMode(true);
	open(dirF+fileF);
	run("ROI Manager...");
	roiManager("Open",dirR+fileR);
	W=getWidth();
	H=getHeight();
	nl=0;
	Xl=newArray(1);
	Yl=newArray(1);
	Rl=newArray(1);
	deg=5;
	ndeg=360/deg;
	//If different scale in each image
	dist=getNumber(fileR+" / Scale in mm:", 2);
	px=getNumber(fileR+" / Scale in px:", 575);
	sc=dist/px;
	//If unique scale for all images
	//sc=2/575;
	sc2=sc*sc;

	//Orientation
	roiManager("Select",1);
	run("Set Measurements...", "  redirect=None decimal=3");
	run("Measure");
	ang=getResult("Angle",0);
```

```
selectWindow("Results");
run("Close");

//Lumen outline + centroid and outline coordinate determination
run("Set Measurements...", "centroid redirect=None decimal=3");
roiManager("Select",0);
roiManager("Measure");
Xc=getResult("X",0);
Yc=getResult("Y",0);
selectWindow("Results");
run("Close");
roiManager("Deselect");
newImage("Lumen outline", "8-bit white", W, H, 1);
roiManager("Select",0);
setForegroundColor(0,0,0);
run("Draw");
for(i=0;i<H;i++){
	for(j=0;j<W;j++){
		if(getPixel(j,i)==0){
			Xl[nl]=j;
			Yl[nl]=i;
			Rl[nl]=-atan2(Yl[nl]-Yc,Xl[nl]-Xc)*180/PI;
			nl++;
		}
	}
}
selectWindow("Lumen outline");
run("Close");
Rlranks=Array.rankPositions(Rl);
Rl=Array.sort(Rl);
XlT=Array.copy(Xl);
YlT=Array.copy(Yl);
for(i=0;i<nl;i++){
	Xl[i]=XlT[Rlranks[i]];
	Yl[i]=YlT[Rlranks[i]];
}

//LN outline coordinate list generation
nROI=roiManager("Count");
nLN=nROI-2;
Rln2=newArray(ndeg);
for(i=0;i<Rln2.length;i++){
	Rln2[i]=-180+i*deg;
}
for(k=0;k<nLN;k++){
	newImage("LN outline", "8-bit white", W, H, 1);
	run("Set Measurements...", "centroid redirect=None decimal=3");
	roiManager("Select",k+2);
	roiManager("Measure");
	Xlnc=getResult("X",0);
	Ylnc=getResult("Y",0);
	selectWindow("Results");
	run("Close");
	setForegroundColor(0,0,0);
	run("Draw");
	nln=0;
	Xln=newArray(1);
```

```
Yln=newArray(1);
Rln=newArray(1);
for(i=0;i<H;i++){
	for(j=0;j<W;j++){
		if(getPixel(j,i)==0){
			Xln[nln]=j;
			Yln[nln]=i;
			Rln[nln]=-atan2(Yln[nln]-Ylnc,Xln[nln]-Xlnc)*180/PI;
			nln++;
		}
	}
}
selectWindow("LN outline");
run("Close");
//Angular ranking
Rlnranks=Array.rankPositions(Rln);
Rln=Array.sort(Rln);
XlnT=Array.copy(Xln);
YlnT=Array.copy(Yln);
for(i=0;i<nln;i++){
	Xln[i]=XlnT[Rlnranks[i]];
	Yln[i]=YlnT[Rlnranks[i]];
}

//Point selection each 5deg
Xln1=newArray(ndeg);
Yln1=newArray(ndeg);
Rln1=newArray(ndeg);
deg2=0;
for(i=0;i<nln-1;i++){
	if(deg2==0){
		if(abs(Rln[i]+180)<=abs(Rln[nln-1]-180)){
			Xln1[deg2]=Xln[i];
			Yln1[deg2]=Yln[i];
		}else{
			Xln1[deg2]=Xln[i+1];
			Yln1[deg2]=Yln[i+1];
		}
		deg2+=1;
	}else if(deg2==ndeg){
		break;
	}else{
		if((Rln[i]-Rln2[deg2])<0 && (Rln[i+1]-Rln2[deg2])>=0){
			if(abs(Rln[i]-Rln2[deg2])<=abs(Rln[i+1]-Rln2[deg2])){
				Xln1[deg2]=Xln[i];
				Yln1[deg2]=Yln[i];
			}else{
				Xln1[deg2]=Xln[i+1];
				Yln1[deg2]=Yln[i+1];
			}
			deg2+=1;
		}
	}
}
Rlnl=newArray(ndeg);
Lln=newArray(ndeg);
XlnB=newArray(ndeg);
```

```
		YlnB=newArray(ndeg);
		for(i=0;i<ndeg;i++){
			Rlnl[i]=-atan2(Yln1[i]-Yc,Xln1[i]-Xc)*180/PI;
			for(j=0;j<Xl.length-1;j++){
				if((Rl[j]-Rlnl[i])<0 && (Rl[j+1]-Rlnl[i])>=0){
					Lln[i]=sqrt(pow(Xl[j]-Xln1[i],2)+pow(Yl[j]-Yln1[i],2));
					Rlnl[i]-=ang;
					break;
				}else if(j==Xl.length-2){
					Lln[i]=sqrt(pow(Xl[j+1]-Xln1[i],2)+pow(Yl[j+1]-Yln1[i],2));
					Rlnl[i]-=ang;
					break;
				}
			}
			setResult("Angle"+d2s(k+1,0),i,Rlnl[i]);
			setResult("Distance"+d2s(k+1,0),i,Lln[i]*sc);
		}
		saveAs("Results","E:\\Results\\Lymph
Node\\"+substring(fileF,0,indexOf(fileF,".jpg"))+"_LN"+d2s(k+1,0)+".txt");
		if(k==nLN-1){
			close(fileF);
		}
	}
	roiManager("Deselect");
	roiManager("Delete");
}
```

8.3. Nerve ablation morphometry in renal artery – ImageJ script

```
macro AblationMapping{
	//Parameter definition
	setOption("ExpandableArrays",true);
	W=getWidth();
	H=getHeight();
	Xab=newArray(1);
	Yab=newArray(1);
	Xab2=newArray(1);
	Yab2=newArray(1);
	Rab=newArray(1);
	Lab=newArray(1);
	Xl=newArray(1);
	Yl=newArray(1);
	Rl=newArray(1);
	nl=0;
	nab=0;
	sc=575/2;
	//Lumen outline generation and centroid location
	run("ROI Manager...");
	roiManager("Select",0);
	run("Set Measurements...", "centroid redirect=None decimal=3");
	run("Measure");
	Xc=getResult("X",0);
	Yc=getResult("Y",0);
	selectWindow("Results");
	run("Close");

	//Lumen outline coordinate list generation
	newImage("Lumen outline", "8-bit white", W, H, 1);
	roiManager("Select",0);
	run("Draw");
	for(i=0;i<H;i++){
		for(j=0;j<W;j++){
			if(getPixel(j,i)==0){
				Xl[nl]=j;
				Yl[nl]=i;
				nl++;
			}
		}
	}
	selectWindow("Lumen outline");
	run("Close");

	//Orientation
	roiManager("Select",1);
	run("Set Measurements...", "  redirect=None decimal=3");
	run("Measure");
	ang=getResult("Angle",0);
	selectWindow("Results");
	run("Close");

	//Ablation area outline coordinate list generation
	roiManager("Select",2);
	roiManager("Measure");
	for(i=0;i<nResults;i++){
```

```
		Xab[i]=getResult("X",i);
		Yab[i]=getResult("Y",i);
		if(i==nResults-1){
			Xab[i+1]=Xab[0];
			Yab[i+1]=Yab[0];
		}
	}
	selectWindow("Results");
	run("Close");

	//Coordinate list sorting based on angle from centroid
	for(i=0;i<Xab.length;i++){
		Rab[i]=atan2(Yab[i]-Yc,Xab[i]-Xc)*180/PI;
	}
	for(i=0;i<nl;i++){
		Rl[i]=atan2(Yl[i]-Yc,Xl[i]-Xc)*180/PI;
	}
	Rlranks=Array.rankPositions(Rl);
	Rl=Array.sort(Rl);
	XlT=Array.copy(Xl);
	YlT=Array.copy(Yl);
	for(i=0;i<nl;i++){
		Xl[i]=XlT[Rlranks[i]];
		Yl[i]=YlT[Rlranks[i]];
	}
	for(i=0;i<Xab.length;i++){
		Rab[i]=atan2(Yab[i]-Yc,Xab[i]-Xc)*180/PI;
		for(j=0;j<Xl.length-1;j++){
			if((Rl[j]-Rab[i])<0 && (Rl[j+1]-Rab[i])>=0){
				Lab[i]=sqrt(pow(Xl[j]-Xab[i],2)+pow(Yl[j]-Yab[i],2));
				Xab2[i]=(Lab[i]+sc*2.5)*cos(Rab[i]*PI/180);
				Yab2[i]=-(Lab[i]+sc*2.5)*sin(Rab[i]*PI/180);
				break;
			}
		}
	}
	for(i=0;i<Xab.length;i++){
		Xab[i]=(Xab[i]-Xc);
		Yab[i]=-(Yab[i]-Yc);
		setResult("X",i,Xab[i]/sc);
		setResult("Y",i,Yab[i]/sc);
		setResult("Angle",i,Rab[i]-ang);
		setResult("Length",i,Lab[i]/sc);
		setResult("X2",i,Xab2[i]/sc);
		setResult("Y2",i,Yab2[i]/sc);
	}
}
```

8.4. Nerve ablation circumferential coverage evaluation – ImageJ script

```
macro RadialAblationCoverage{
	//Parameter definition
	H=getHeight();
	W=getWidth();
	Xl=newArray(1);
	Yl=newArray(1);
	Rl=newArray(1);
	nl=0;
	rad=1;
	deg=10;
	ndeg=360/deg;
	X0=newArray(ndeg);
	Y0=newArray(ndeg);
	L0=newArray(ndeg);
	Rl2=newArray(ndeg);
	F0=newArray(ndeg);
	F1=newArray(ndeg);
	F2=newArray(ndeg);
	F3=newArray(ndeg);
	F4=newArray(ndeg);
	F5=newArray(ndeg);

	ringDepth=2.5;
	waitForUser("Manual steps","1) Set mm/px scale.\n2) If necessary, crop image.\n3) Select lumen outline with Polygon Selection tool.\n4) Fit Spline\n5) Press OK");
	run("ROI Manager...");
	roiManager("Add");
	run("Set Scale...", "distance=287 known=1 unit=mm");
	setOption("ExpandableArrays",true);

	//Ablation area generation
	waitForUser("Manual steps","1) Fit polygon + spline to ablation zone.\n2) Add to the ROI Manager.\n3) Repeat steps 1 and 2 for each zone.\n4) Select all ablation zone ROI's, combine with OR operation.\n5) Add the final ROI and delete individual selections.\n6) Press OK");
	roiManager("Add");

	//Lumen outline coordinate list generation
	newImage("Lumen outline", "8-bit white", W, H, 1);
	roiManager("Select",0);
	run("Draw");

	//Centroid location
	roiManager("Select",0);
	run("Set Measurements...", "centroid redirect=None decimal=3");
	run("Measure");
	Xc=getResult("X",0);
	Yc=getResult("Y",0);
	selectWindow("Results");
	run("Close");

	//Lumen outline coordinate list generation
	for(i=0;i<H;i++){
		for(j=0;j<W;j++){
			if(getPixel(j,i)==0){
				Xl[nl]=j;
```

```
                        Yl[nl]=i;
                        Rl[nl]=atan2(Yl[nl]-Yc,Xl[nl]-Xc)*180/PI;
                        nl++;
                }
        }
}
selectWindow("Lumen outline");
run("Close");

//Coordinate list sorting based on angle from centroid
Rlranks=Array.rankPositions(Rl);
Rl=Array.sort(Rl);
XlT=Array.copy(Xl);
YlT=Array.copy(Yl);
for(i=0;i<nl;i++){
        Xl[i]=XlT[Rlranks[i]];
        Yl[i]=YlT[Rlranks[i]];
}

//Finding lumen coordinates located at multiples of deg
for(i=0;i<Rl2.length;i++){
        Rl2[i]=-180+i*deg;
}
deg2=0;
for(i=0;i<nl-1;i++){
        if(deg2==0){
                if(abs(Rl[i]+180)<=abs(Rl[nl-1]-180)){
                        X0[deg2]=Xl[i];
                        Y0[deg2]=Yl[i];
                }else{
                        X0[deg2]=Xl[i+1];
                        Y0[deg2]=Yl[i+1];
                }
                deg2+=1;
        }else if(deg2==ndeg){
                break;
        }else{
                if((Rl[i]-Rl2[deg2])<0 && (Rl[i+1]-Rl2[deg2])>=0){
                        if(abs(Rl[i]-Rl2[deg2])<=abs(Rl[i+1]-Rl2[deg2])){
                                X0[deg2]=Xl[i];
                                Y0[deg2]=Yl[i];
                        }else{
                                X0[deg2]=Xl[i+1];
                                Y0[deg2]=Yl[i+1];
                        }

                        deg2+=1;
                }
        }
}
toScaled(Xc,Yc);

//Determining the length from the centroid to the lumen in X0Y0 points
for(i=0;i<ndeg;i++){
        toScaled(X0[i],Y0[i]);
        L0[i]=sqrt(pow(X0[i]-Xc,2)+pow(Y0[i]-Yc,2));
}
```

```
	//Radial/Angular point generation + Boolean location of ablation zone
	roiManager("Select",1);
	for(i=0;i<6;i++){
		for(j=0;j<ndeg;j++){
			if(i==0){
				X=X0[j];
				Y=Y0[j];
			}else{
				X=X0[j]+i*rad*cos(Rl2[j]*PI/180);
				Y=Y0[j]+i*rad*sin(Rl2[j]*PI/180);
			}
			toUnscaled(X,Y);
			roiManager("Select",1);
			setResult(d2s(i,0)+"mm",j,selectionContains(X,Y));
			makePoint(X,Y);
			roiManager("Add");
		}
	}
}
```

Publications and conference abstracts

Publications

- Garcia-Polite F, Martorell J, Del Rey-Puech P, Melgar-Lesmes P, O'Brien CC, Roquer J, Ois A, Principe A, Edelman ER, Balcells M. Pulsatility and high shear stress deteriorate barrier phenotype in brain microvascular endothelium. *Journal of Cerebral Blood Flow & Metabolism* 2016 (accepted).

Conference abstracts

- **Innovations in Cardiovascular Interventions (ICI)**. December 2015. Tel-Aviv, Israel. Tzafriri AR, Bailey L, Keating JH, Garcia-Polite F, Markham P, Prutchi D, Edelman ER. *Effective Circumferential Ablation using a Multi-electrode Bipolar/Unipolar Over-the-Wire Renal Denervation RF Catheter System with Closed Loop Sensing*.
- **Transcatheter Cardiovascular Therapeutics (TCT).** October 2015. San Francisco, CA, USA. Tzafriri AR; Bailey L; Keating JH; Garcia-Polite F; Markham PM; Prutchi D; Edelman ER. *Enhanced Circumferential Ablation using a Multi-electrode Bipolar/Unipolar Over-the-Wire Renal Denervation RF Catheter System with Closed Loop Sensing.*
- **11th International Conference on Cerebral Vascular Biology**. July 2015. Paris, France. F. Garcia-Polite, P. del Rey-Puech, J. Martorell, C.C. O'Brien, M. O'Rourke, E.R. Edelman, M. Balcells. *Increasing wall shear stress correlates with tight junction expression and P-glycoprotein efflux activity in microvascular endothelial cells at the neurovascular unit*. (Poster)
- **11th International Conference on Cerebral Vascular Biology**. July 2015. Paris, France. P. del Rey-Puech, F. Garcia-Polite, M. Lopez, J. Roquer, A. Ois, A. Principe, P. Melgar-Lesmes, E.R. Edelman, M. Balcells. *Impact of cellular components and their interaction in Blood-Brain Barrier phenotype*. (Poster)
- **11th International Symposium on Endovascular Therapeutics**. June 2015. Barcelona, Spain. F. Garcia-Polite, P. del Rey-Puech, J. Martorell, C.C. O'brien, E.R. Edelman, M. Balcells. *Tight junction expression and efflux activity correlate with shear stress in microvascular endothelial cells at the Blood-Brain Barrier*. (Poster)
- **11th International Symposium on Endovascular Therapeutics**. June 2015. Barcelona, Spain. P. del Rey-Puech, F. Garcia-Polite, J. Martorell, J. Roquer, A. Ois, M. Balcells. *Blood-Brain Barrier phenotype is impacted by cellular components and their interaction*. (Poster)

- **International Stroke Conference 2015**. February 2015. Nashville (TN), United States. S. Salehi-Omran, F. Garcia-Polite, E.R. Edelman, M. Balcells. *Shear Stress and Coculture with Astrocytes Determine Brain Microvascular Endothelial Cell Phenotype*. (Poster)
- **17th International Symposium on Signal Transductions at the Blood-Brain Barrier and Blood-Retina Barriers**, September 2014. Dublin, Ireland. F. García-Polite, J. Martorell, A.A. García-Granada, E.R. Edelman, M. Balcells. *Disrupted wall shear stress alters autocrine signaling of brain microvascular endothelial cells at the blood-brain barrier*. (Poster)
- **15th international symposium: Signal Transductions at the Blood-Brain Barrier**, September 2012. Potsdam, Germany. F. García-Polite, A.A. García-Granada, J.J. Molins Vara, M. Balcells. *CAD generation software of brain capillary networks for FEM simulation*. (Poster)